Title
Seismic Tomography of California and Nevada

Author
Doody, Claire Diane

Publication Date
2023

Peer reviewed|Thesis/dissertation

Adjoint waveform tomography of California and Nevada

By

Claire Doody

A dissertation submitted in partial satisfaction of the

requirements for the degree of

Doctor of Philosophy

in

Earth & Planetary Science

in the

Graduate Division

of the

University of California, Berkeley

Committee in charge:

Professor Barbara Romanowicz, Chair
Professor Richard Allen
Professor Michael Manga
Professor Stuart Russell
Doctor Arthur Rodgers

Spring 2023

Adjoint waveform tomography of California and Nevada

Abstract

Seismic Tomography of California and Nevada

by

Claire Doody

Doctor of Philosophy in Earth & Planetary Science

University of California, Berkeley

Professor Barbara Romanowicz, Chair

Accurate seismic velocity models are a necessary parameter for seismic hazard analysis in high hazard regions. Therefore, we present the California-Nevada Adjoint Simulations (CANVAS) model, an adjoint waveform tomography model of California and Nevada that is optimized to fit waveforms. We began by testing different starting models for CANVAS to determine what effect starting model choice plays on final inversion results. Though studies have compared synthetic seismograms to compare starting models (e.g., Zhou et al., 2021), this is the first study to compare results after inversion. We chose CSEM_NA (Krischer et al., 2018), SPiRaL (Simmons et al., 2021), and WUS256 (Rodgers et al., 2022) as starting models and iterated each model to a minimum period of 20 seconds. We then compared the results of the final models using five comparison metrics. All five of the comparison metrics showed that the final models all resolved tectonic structure and fit observed data similarly, regardless of the structure or fit of the starting models. Therefore, we conclude that the choice of starting model has minimal effect on the final model results.

Errors in source mechanisms can produce bad synthetic seismograms, which limit the data available to use in adjoint waveform tomography inversions. Many researchers use source mechanisms from the Global Centroid Moment Tensor (GCMT) catalogue. However, the GCMT catalogue has known issues with resolving shallow crustal earthquakes. Since shallow crustal earthquakes dominate CANVAS's dataset, we inverted for source mechanisms using MTTime, a time-domain moment tensor inversion code. We calculated 3D Green's functions using an intermediate version of CANVAS that was iterated to a minimum period of 20 seconds. We showed that the inverted source mechanisms greatly improved waveform fit compared to the GCMT solutions, particularly at distant stations. We also demonstrated that 3D Green's functions have better and more consistent waveform fits compared to solutions inverted using 1D Green's functions.

Before introducing shorter period data in CANVAS, we replaced the original GCMT solutions with the inverted solutions. Synthetics calculated using the inverted source mechanisms better matched the amplitude of the observed data, and greatly increased the amount of windowed data that could be included in the inversion of CANVAS. Therefore, we advocate for the importance of regularly updating source mechanisms in adjoint waveform tomography workflows. We conclude by proposing CANVAS, an adjoint waveform tomography model of California and

Nevada iterated to a minimum period of 12 seconds. Though CANVAS has coarse resolution compared to other crustal tomography models, it can resolve the geographic extents and velocities of well-known tectonic features throughout California and Nevada. The model particularly excels at fitting the dispersed surface waves, showing significant improvement compared to its starting model, WUS256 (Rodgers et al., 2022). Finally, CANVAS also accurately resolves the depth to basement of large basins in California without *a priori* basin information. This highlights the inherent information contained in seismic waveforms, which full waveform inversion tomography is exceptional at harnessing. We hope that CANVAS can be used as a starting model for smaller regional tomography studies that could eventually become input velocity models for stress inversions or rupture propagation models.

Contents

List of Figures

List of Tables

Preface

Sitting at the junction of the North American, Pacific, and Gorda plates, California is a tectonically complex region with high seismic hazard across the entirety of the state. The study of California seismicity began when UC Berkeley professor Andrew Lawson wrote the Lawson Report in the aftermath of the 18 April 1906 Great San Francisco Earthquake (Lawson, 1908). The use of seismic waves to study the interior of the Earth has a similar long history. In 1936, Danish seismologist Inge Lehmann proposed the existence of the inner core based on reflected seismic waves from distant earthquakes (Lehmann, 1936). Since then, scientists have continued to use seismic data to better understand the Earth's composition. Seismic tomography came to prominence in the 1970s with formative work by Keiiti Aki (Aki and Lee, 1976; Aki et al., 1977). Aki's work used the arrival times of p-waves at dense seismic arrays to invert for the velocity structure of the Earth in California, in a method now commonly referred to as travel-time tomography (Aki and Lee, 1976).

Travel-time tomography is still widely used to study Earth's interior. However, as high-performance computing has become readily available, more complex techniques to determine Earth's velocity structure have emerged. Full waveform inversion is a type of seismic tomography that iteratively optimizes the fit between observed and synthetic data. Synthetic data are calculated by solving the wave equation through a given velocity model; unlike travel-time tomography, full waveform inversion can account for 3D wavefield effects (Liu and Gu, 2012; Rickers et al., 2012; Tarantola, 1984). California is a fantastic natural laboratory for seismic tomography because of azimuthally well-distributed earthquake sources and receivers. Though adjoint waveform tomography models have been produced for southern California (e.g., Tape et al., 2009; Wang et al., 2022), none has been proposed for the whole state until this study. Therefore, we proposed CANVAS, an adjoint waveform tomography model of California and Nevada.

The construction of CANVAS is broken into three main steps which correspond to the three chapters presented herein:

Chapter 1- Comparing Adjoint Waveform Tomography Models of California Using Different Starting Models: Adjoint waveform tomography requires a starting model to produce the synthetic waveforms necessary to iterate the model. Because of the high computational cost of computing adjoint waveform tomography inversions, comparison of the effect of starting models had previously been restricted to forward modelling (e.g., Zhou et al., 2022). Using computational resources available through Lawrence Livermore National Laboratory's Livermore Computing center, we calculated three adjoint tomography models of California using three different starting models. The starting models (CSEM_NA, Krischer et al., 2018; SPiRaL, Simmons et al., 202; WUS256, Rodgers et al., 2022) all have varying degrees of resolution and accuracy in the domain of interest. We used a conservative, multi-scale inversion approach to invert the three models to a minimum period of 20 seconds. To compare the results of the three inverted models, we proposed five different comparison metrics—two in the model-space and three in the data-space. All five metrics showed that the three inverted models resolved the same tectonic structure and had reasonably similar waveform fits. Therefore, we concluded that the final models had little dependence on the starting models. This conclusion requires certain qualification. Firstly, we made careful methodological choices, including running many iterations and using a multi-scale approach that slowly adds in shorter period information, among other choices outlined in Chapter 1. Secondly, this conclusion has only been tested at long wavelengths, so further research is required to determine if iterating to shorter periods would cause this conclusion to not hold. Finally, California has azimuthally well-distributed sources and receivers, which allow for many crossing ray paths. Further research is needed to determine if these caveats are necessary to converge to the same model. This chapter is adapted from a previously published article: *Doody, C., Rodgers, A., Afanasiev, M., Boehm, C., Krischer, L., Chiang, A., & Simmons, N. Comparing adjoint waveform tomography models of California using different starting models.* Journal of Geophysical Research: Solid Earth. https://doi.org/10.1029/2023JB026463. Model data from this study can be found at *Doody, C. (2023a). Dataset for 'Comparing adjoint waveform tomography models of California using different starting models.' [Dataset].* Zenodo. https://doi.org/10.5281/zenodo.7830683

Chapter 2- Moment Tensor Catalogue for California and Nevada Using 3D Green's Functions: Earthquake source mechanisms are a necessary parameter in calculating synthetic seismograms in the adjoint waveform tomography workflow. Most researchers use the Global Centroid Moment Tensor (GCMT) catalogue (Dziewonski et al., 1981; Ekström et al., 2012) since it produces consistently accurate source mechanisms on a global scale. However, the methodology used to calculate the GCMT solutions have inherent issues, particularly for small, crustal events like most events in California and Nevada. To produce more accurate source mechanisms, we used an intermediate version of CANVAS (the CANV_WUS model in Chapter 1) to calculate 3D Green's functions. The main benefit of using 3D Green's functions instead of 1D Green's functions is that the 3D model can capture lateral heterogeneity, and so more accurately model waveforms. We showed that the inverted solutions using 3D Green's functions fit the data better than the GCMT solution and have similar mechanisms to higher-quality local catalogue solutions. We also compared the result of 1D and 3D Green's functions to highlight how 3D Green's functions produce more consistent fits to the data than 1D Green's functions. 3D Green's functions also have better fits to distant stations, producing similar moment tensor results when only using stations that are greater than 400km from the epicenter. The performance of 3D Green's functions in computing source mechanisms has broad implications for improved source constraints on offshore events, and more broadly to provide improved moment tensors in areas of the world where data coverage is sparse.

Chapter 3- CANVAS: An Adjoint Waveform Tomography Model of California and Nevada: This thesis culminates with the presentation of the California-Nevada Adjoint Simulations (CANVAS) model. CANVAS is an adjoint waveform tomography model of the crust and uppermost mantle iterated to a minimum period of 12 seconds. Velocity models provide important constraints on other seismological observations such as stress inversions and rupture propagation modelling, both of which inform seismic hazard analysis. Therefore, to provide accurate seismic hazards, accurate velocity models are necessary. Though other models of the state exist (Lin et al., 2010; Stanciu and Humpreys, 2021), CANVAS is the first adjoint waveform tomography model of the state. CANVAS is iterated in two distinct stages: the first stage with source mechanisms from the GCMT, and the second stage with the source mechanisms calculated in Chapter 2. We showed that updating the source mechanisms significantly improves waveform fits and azimuthal coverage of windowed data used to calculate the gradients. As for the model itself, we improved waveform fits over our starting model, WUS256 (Rodgers et al., 2022), particularly in the dispersed surface waves. CANVAS resolved tectonic features seen in other models and was able to accurate define the depth to basement of major basins, including the Central Valley and the Ventura Basin. We hope that CANVAS can serve as a starting model for iterating to shorter periods over the state, or for crustal tomography models on smaller scales.

This thesis adds to the body of seismic tomography work in California, while also attempting to understand fundamental questions in the adjoint waveform tomography methodology. Each chapter builds off the work of the previous chapter to culminate in the presentation of the CANVAS model. Though CANVAS is coarse compared to other crustal studies of California (e.g., Lin et al., 2010; Share et al., 2019), we believe that CANVAS's ability to fit waveforms make it a good candidate as a starting model for smaller-scale regional studies. These regional studies could provide high-resolution, accurate velocity models that can provide significant constraints on seismic hazard analysis throughout California.

Acknowledgements

I would like to begin by thanking my advisors, Artie Rodgers and Richard Allen, for their tireless help in seeing this thesis to fruition. This dissertation has taken many forms over the past 5 years, and I am eternally grateful for the support that they have given me to explore many areas of research. I would like to thank Richard for convincing me that Berkeley was the best place to do a PhD and for introducing me to the field of seismic tomography; his mentorship throughout the years has been invaluable to my success in graduate school. I would also like to thank Artie for taking me in as an intern in 2020 and providing support and guidance over the past three years that brought this thesis to life.

I would also like to acknowledge my chair, Barbara Romanowicz, and her group, who have been instrumental as my research transitioned to full waveform inversion in 2020. I thank Barbara, Li-Wei Chen, Dan Frost-Tan, Chao Lyu, Utpal Kumar, and Federico Munch for being a sounding board for new ideas and for always asking the difficult questions. I would also like to thank my other two committee members, Michael Manga and Stuart Russell, for their feedback on this thesis and other projects throughout the years.

I would be remiss not to thank the Allen group, who have been instrumental as both collaborators and friends over my PhD. William Hawley, Robert Martin-Short, and Qingkai Kong were amazing mentors at the beginning of my PhD. Sarina Patel has been my rock for the past five years, and I couldn't have asked for a better labmates and friends in her, Yuancong Gou, and Savvas Marcou. Thank you also to Angie Chung, Jenn Strauss, Eliza Karlowska, and Sam Goldstein for their support over the years. I'd also like to thank the Berkeley Seismology Lab, particularly Zack Alexy, Doug Dreger, Peggy Hellweg, Horst Rademacher, and Taka'aki Taira. My officemates Mrinal Dursun, Yuexin Li, Dani Lindsay, Kathryn Materna, and Runze Miao have been continual sources of inspiration and laugther.

My journey in seismology would have never been possible without the IRIS internship program. My internship advisors Adam Ringler and Rob Anthony have been my biggest cheerleaders since 2017 and none of this would have been possible without them. I would also like to thank my other IRIS interns, especially Travis Alongi, Jimmy Atterholt, and Claire Richardson. I would also thank my collaborators Mike Afanasiev, Christian Boehm, Andrea Chiang, Lion Krischer, Chris Morency, and Nathan Simmons, who have all contributed significantly to the work presented herein.

Finally, none of this would have been possible without my family and friends. My parents, Jim and Wendy, and my brothers, Paul, Tim, and Thomas, have been my greatest support system since Day 1. A big thank you also to my friends: Alex, Andrew, Andy, Ashleigh, Chelsea, Erin, Helena, Jo, Jordana, Julia, Kate, Leah, Maddie, Mara, Michelle, Nathaniel, Ryan, Rodrigo, Sarah, Sevan, Shana, Stephanie, Will, and many, many more who aren't named here.

Chapter 1

Comparing adjoint waveform tomography models of California using different starting models

1.1 Abstract

Adjoint waveform tomography (AWT) sits at the cutting edge of seismic tomography on local, regional, and global scales. However, the choice in starting model may have a significant impact on the final inversion results. In this paper, we present 3 AWT models of California that are based on different starting models. We chose three models that were inverted at different scales: SPiRaL, a global travel-time tomography model (Simmons et al., 2021), CSEM_NA, a regional adjoint tomography model of North America and the North Atlantic (Krischer et al., 2018), and WUS256, a regional adjoint tomography model of the western US (Rodgers et al., 2022). We then inverted three AWT models using the same source and receiver set. We ran each model over 3 period bands: 30-100 seconds, 25-100 seconds, and 20-80 seconds. Once the iterations were finalized, we used five methods of testing model similarity in both the model and data space. We conclude that the choice of starting model has a minimal impact on long wavelength models if an appropriate multi-scale inversion approach is used.

1.2 Introduction

Seismic tomography has been a vital tool for understanding Earth's interior structure since studies were first published in the late 1970s (e.g., Aki and Lee, 1976; Aki et al., 1977). Though the theory of full waveform inversion existed, ray-based travel time tomography methods were the primary method of velocity modelling for much of the field's history. Ray-based travel time tomography uses the difference between theoretical and observed arrival times of specified seismic waves to calculate velocity perturbations in the Earth (Dziewonski et al., 1977). Ray-based tomography can be computationally inexpensive but suffers in tectonically complex regions as the physics behind it is unable to resolve effects such as wavefront healing, focusing/defocusing, and other 3D wavefield effects (Liu and Gu, 2012; Rickers et al., 2012; Tarantola, 1984). Unlike ray-based methods, adjoint waveform tomography (AWT) accounts for 3D wavefield effects by solving the elastic wave equation through a given 3D volume, while also considering finite-frequency effects. AWT iteratively optimizes the synthetic data to best match the observed data for available source-receiver pairs. By using the recorded waveform instead of travel times, AWT includes more information (Romanowicz, 2003). AWT has a greater sensitivity to Earth structure than ray-based travel time tomography, enabling greater resolution of tectonic complexity.

Uncertainty analysis and quantitative comparisons of FWI models continues to be a topic of active research (Flath et al., 2011; Gebraad et al., 2020; Martin et al., 2012; Rawlinson et al., 2014; Ulrich et al., 2022; Zhu et al., 2016). In linearized ray-based travel time tomography, uncertainty can be assessed through built-in uncertainty in travel time picks and the computation of model resolution matrices. In practice, model performance in full waveform inversion models is evaluated in three ways: qualitative waveform fits, performance of model on validation events (i.e. events not included in the inversion; Tape et al., 2010), bootstrapping (e.g., French and Romanowicz, 2014), and qualitative resolution analysis through methods such as checkerboard resolution tests, which are known to have significant drawbacks (e.g. Leveque et al., 1993; Rawlinson and Spakman, 2016), and Hessian vector product calculations (Fichtner and van Leeuwen, 2015; Gao et al., 2018). Uncertainty remains difficult to quantify in FWI models mainly due to the computational cost of computing deterministic and probabilistic uncertainties (e.g., Gebraad et al., 2020; Liu and Peter, 2019; Tarantola, 1987; Virieux and Operto, 2009).

As for model comparison, quantitative comparisons are made difficult by the different parameterization of models by different researchers. The misfit function chosen, events and stations included in the inversions, attenuation model used, and regularization employed all affect model results (Tromp, 2020; Zhou et al., 2022). Though global models show similarity at long wavelengths (Lekic et al., 2012; Ritsema et al., 2011), models diverge as shorter wavelength information is incorporated. In past studies, models are often presented as updates of previous models, using the last version of the model as the starting model for the current model (e.g., Bozdag et al., 2016; French et al., 2013; French and Romanowicz, 2014; Lei et al., 2020). Recent studies have also begun to use 1-D velocity models such as the Preliminary Reference Earth Model (PREM; Dziewonski and Anderson, 1981) to avoid artefacts from the starting model (e.g., Boehm et al., 2022; Metivier et al., 2016).

In this paper, we use a multi-scale, iterative approach to compute three AWT models of California that each start from a different starting model. All three models reveal known tectonic features of the region. We find that the models obtained from this approach are broadly equivalent in terms of their shear wavespeeds and waveform fits. We conclude that using the methodology presented herein, we find that there is minimal effect of the starting model on the final model results.

1.3 Methods

1.3.1 Data

We collected waveform data from 103 regional earthquakes recorded within our domain (Figure 1.1). The events used occurred between January 1, 2000 and October 31, 2020 with moderate moment magnitudes (M_w) between 4.5-6.5. The lower magnitude threshold is dictated by signal-to-noise ratios at long periods, while the upper threshold is chosen such that we can use the point-source approximation. Some larger magnitude earthquakes (M_w 6-6.5) had complex waveforms indicative of finite fault ruptures that we could not model, so those events were excluded during quality control. Focal mechanisms for the events were taken from the Global Centroid Moment Tensor (GCMT) catalog (Dziewonski and Woodhouse, 1983; Ekstrom et al., 2012). The events were recorded at over 1300 unique stations from more than 40 permanent and temporary networks (Figure 1.1; for a list of networks, please refer to the appendix). Waveforms were collected from FDSN web services and stored in the Adaptable Seismic Data Format (ASDF; Krischer et al., 2016).

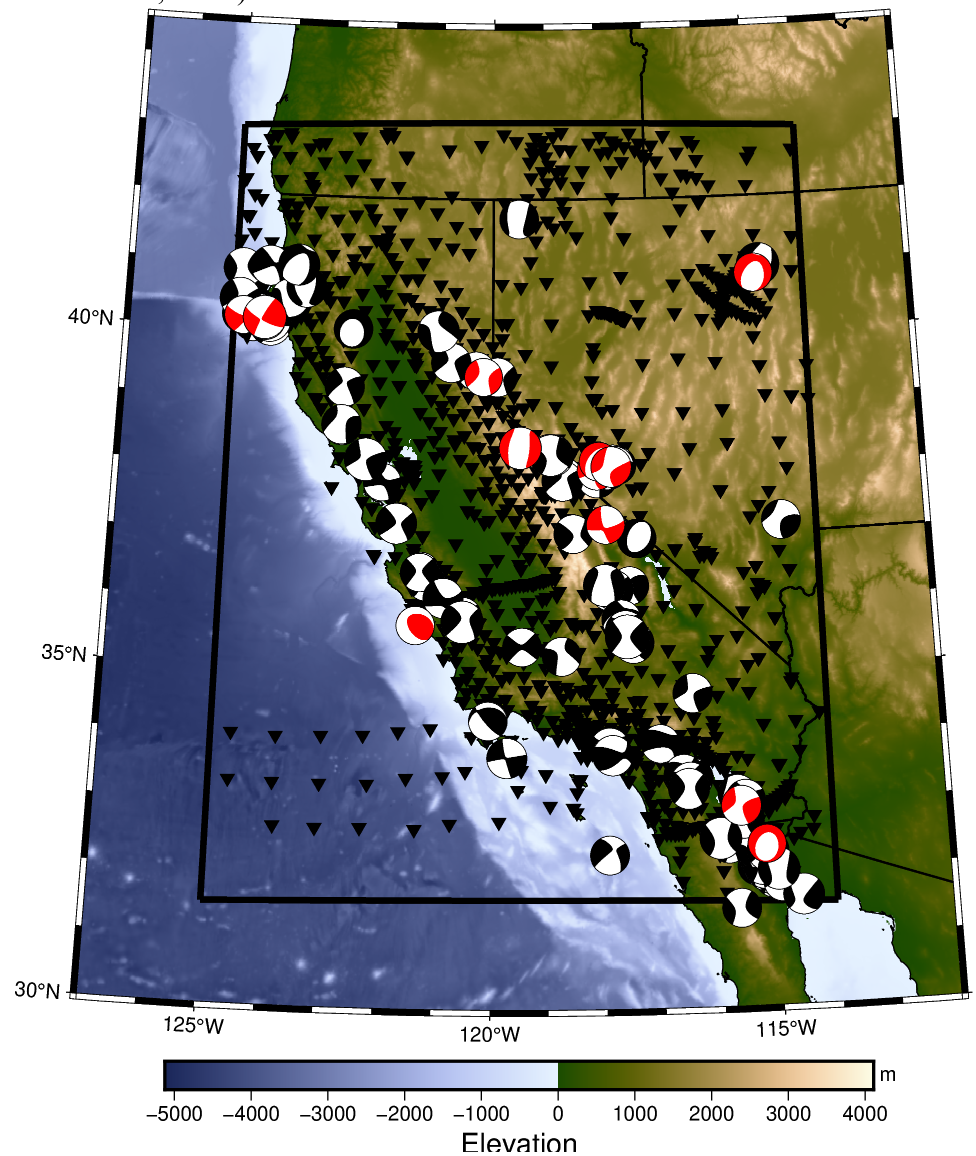

Figure 1.1. Map of the inversion domain. The black box indicates the geographic extent of the inversion domain. The black moment tensors indicate the location of the 103 earthquakes used in the inversion; the red moment tensors indicate the location of the 15 validation events. Moment tensors were taken from the GCMT catalog (Ekstrom et al., 2012). The inverted black triangles indicate the location of all stations with data used in the inversion and/or validation.

1.3.2 Inversion Methodology

AWT is computation- and data-intensive and requires efficient workflow software to automatically manage the costly computations and volume of data required to run adjoint waveform tomography (AWT) iterations. Several software packages have become available in the past few years to enable AWT (Krischer et al., 2015; Modrak et al., 2018; Chow et al., 2020; Thrastarson et al., 2021). In this study, we used Salvus, an end-to-end full waveform inversion software from Mondaic Ltd. (mondaic.com). Salvus manages data processing, forward simulations, window picking, misfit calculations, and inversions, including communication between the user's local machine and the high-performance computing (HPC) cluster used. Salvus also builds in visualization and quality control directly into Jupyter Notebooks (Kluyver et al., 2016) that allow the user to check results at any stage of an inversion. For a more detailed description of Salvus and its use, we point the reader to Rodgers et al. (2022) and Wehner et al. (2022).

We begin our inversions with three different starting models that cover our study area: SPiRaL (Simmons et al., 2021), CSEM_NA (Krischer et al., 2018), and WUS256 (Rodgers et al., 2022). These three models were chosen because each includes radial anisotropy, which is essential to fit regional surface waves. The different scales and datasets used to infer these starting models, described below, provide variability that allow us to test the effect of starting models on final inversion results. SPiRaL is a global model obtained from joint inversion of P and S wave arrival times and vertical transverse isotropy. CSEM_NA is an adjoint waveform tomography model of the North Atlantic, including both the North American and European continents. WUS256 is an adjoint waveform tomography model for the western US. It is important to note here that WUS256 uses SPiRaL as its starting model, so we expect that it will show comparatively improved fits prior to any inversions. CSEM_NA is independent of the other two models.

To make our comparison as fair as possible, we use the same regularization scheme described above for all three models. Figure 1.2 provides a flowchart of the steps followed in the inversion methodology and is annotated with key details of the data and methodological choices. We performed multi-scale inversions over three period bands: 30-100 seconds, 25-100 seconds, and 20-80 seconds (Figure 1.2). We began iterations at 30 seconds minimum period because of our small domain size (~1000 kmx1000 km) and focus on resolving crustal structure. We decreased the minimum period band at small increments of 5 seconds to be conservative in our descent down the misfit surface and to avoid getting trapped in local minima (Bunks et al., 1995; Fichtner, 2010). At 20 seconds, we chose to decrease our maximum period band to 80 seconds to improve the signal-to-noise ratio for smaller magnitude events (Mw4.5-5). We solved for four wavespeeds: V_{PV}, V_{PH}, V_{SV}, and V_{SH}, the vertically and horizontally polarized compressional and shear wavespeeds, respectively.

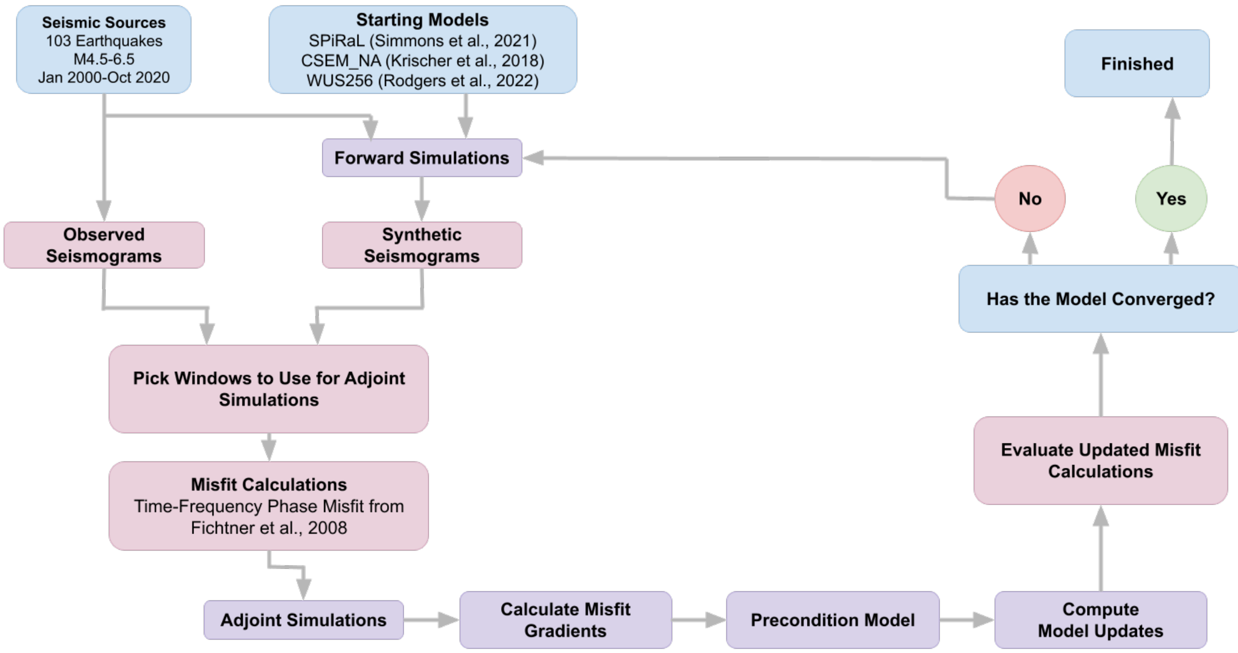

Figure 1.2. Flowchart of inversion steps. All steps aside from data and model downloading are done in Salvus (mondaic.com).

Forward simulations were calculated using the spectral element method on unstructured meshes (Afanasiev et al., 2019; Komatitsch and Tromp, 2002a, b). Window picking is done automatically on the large data set using a modified version of the method proposed by Krischer et al., 2015. The choice of window location and duration is controlled mainly by three parameters: cross-correlation of the observed and synthetic data, the phase shifts between the observed and synthetic data, and the envelope similarity between the observed and synthetic data. If a portion of the waveforms are above a given threshold for all parameters, then a window is chosen. We chose restrictive thresholds such as high correlation values, a minimum window length of 1.5 times the minimum period, and small allowed time shift values to refrain from fitting noise and cycle skipping. We point the reader to Section 1.5.2.1 for a more detailed description of window picking parameters used in this study. We choose conservative thresholds to refrain from fitting noise or cycle slipping. There is one key difference to the model setup that arises during window picking. Because windows are picked based on the similarity between the observed and simulated data, each model has a unique window set. We chose to pick windows separately for each model so as not to bias the results by using the window set from one model (giving advantage to the model with the window set chosen) or to include noise, cycle skipping, or other artefacts in standardized body/surface wave windows. Comparing the windowing statistics of the final model results shows that, in the end, all three models pick windows in similar station-event pairs that are also of similar length. Windowing statistics are discussed in depth in Section 1.5.2.1.

We used the time-frequency phase misfit function (Fichtner et al., 2008) to quantify the misfit of the observed and synthetic data and to compute adjoint sources. The time-frequency phase misfit function converts waveforms into the time-frequency (wavelet) domain (Kristekova et al. 2006; 2009) to compute weighted phase and envelope differences. The time-frequency phase misfit function works well for regions where the wavefield is spatially undersampled and the background model is not well known (Fichtner et al., 2009b). After the misfit is calculated, we compute event sensitivity kernels with the interaction of the forward and adjoint wavefields. The gradients computed are the sum of the sensitivity kernels calculated for each event (Fichtner, 2010; Fichtner et al., 2006; Tape et al., 2007; Tarantola, 1988; Tromp et al., 2005). Model updates are preconditioned with anisotropic smoothing based on the local wavelength of the shortest period; the gradient is smoothed at 0.2 wavelengths in the vertical direction, and 0.5 wavelengths in the lateral directions. To avoid source and receiver effects in the event-dependent gradients, we applied a source cutout of 75 km around the hypocenter and 35 km around each receiver in the 30-100 second and 25-100 second period bands; at 20-80 seconds, we remove the receiver cutouts so that we can begin to resolve upper crustal structure near the receivers.

Finite frequency sensitivity kernels for waveform misfit computed with adjoint methods have outsized amplitudes to near-source and near-receiver structure, which are generally near the Earth’s surface. This could lead to updates in the shallow structure that could trade-off with structure along the path away from the source and receiver. To gradually update crustal structure through the inversion iterations, we instituted a “region of interest” in our first two inversion stages (30-100 seconds and 25-100 seconds) to suppress sensitivities at shallow depths. The region of interest allows us to focus on fitting deeper structure in earlier iterations by minimizing updates above a specified depth (Rodgers et al., 2022). At 30 seconds minimum period, we used a region of interest of 50km; the region of interest is reduced to 15km at 25-100 seconds before being removed at 20-80 seconds.

To compute model updates, we use the Limited-memory Broyden-Fletcher-Goldfarb-Shanno (L-BFGS) approach (e.g., Nocedal and Wright, 2006). We specifically use the trust-region L-BFGS method proposed in Boehm et al. (2018), which uses a quasi-Newton approximation of the inverse Hessian to calculate model updates. This method allows us to compute both step size and direction for each update by minimizing the quadratic approximation of the given objective function. Trust-region L-BFGS approaches have been shown to be more efficient than line search methods in cases where the gradient of the misfit cannot be easily evaluated (Gao et al., 2021; Liu et al., 2022; Modrak and Tromp, 2016).

The key aspects of the method presented above that influence the results of this study are the gradient treatments, the large number of iterations performed, the use of the trust-region L-BFGS optimization approach that checks for good alignment between predicted misfit based on the curvature approximation and the actual misfit, and the multi-scale inversions that allow us to fit long wavelength structure before moving to shorter periods. These factors combined allow us to feel confident in the robustness (i.e., independence of the starting model) of our methodology. When combined, these methodological choices may lead to smaller steps in model space when compared to contemporary regional-scale FWI work.

We believe that cutting off inversions early before the model has converged on its own are the main factors that could lead to different results in the final models. In our inversions, we see that broad changes to the structure happen in the first few iterations; after the elbow point of the misfit curve, the remaining iterations define smaller-scale structures and constrain amplitudes of model features. These later iterations are also key to fitting shorter period, late arriving dispersed surface waves in our models. Stopping before the elbow point of the misfit reduction curve would lead to differing model attributes and waveform fits, therefore likely causing the models to diverge. Given the conclusions of this paper, we believe the inversion approach taken in this study has, in part, allowed us to successfully navigate the necessarily complex misfit surface, and was key in removing the influence of any given starting model.

1.4 Results

Before we begin comparing the three models, we first present the results of the three inverted models. Figures 1.7-1.9 show the isotropic shear wavespeeds at 5, 15, and 55 km depth, respectively. We focus on interpreting the models in the crust and uppermost mantle (<60km) as the period band considered (20-100 seconds) has minimal sensitivity below about 50km (Pasyanos, 2005). Since the crux of this study is comparing model results, we defer tectonic interpretation of the models to a later study. The plots shown below (Figures 1.7-1.9) focus on the lithosphere, but we will refer also to deeper structure. All figures are also masked to only show model features in California. Figure 1.3 shows the ray coverage for all three models. The rays represent great circle paths where at least one window is picked for a given station-event pair. Since most of our ray coverage is in California, we limit our interpretations only to that region.

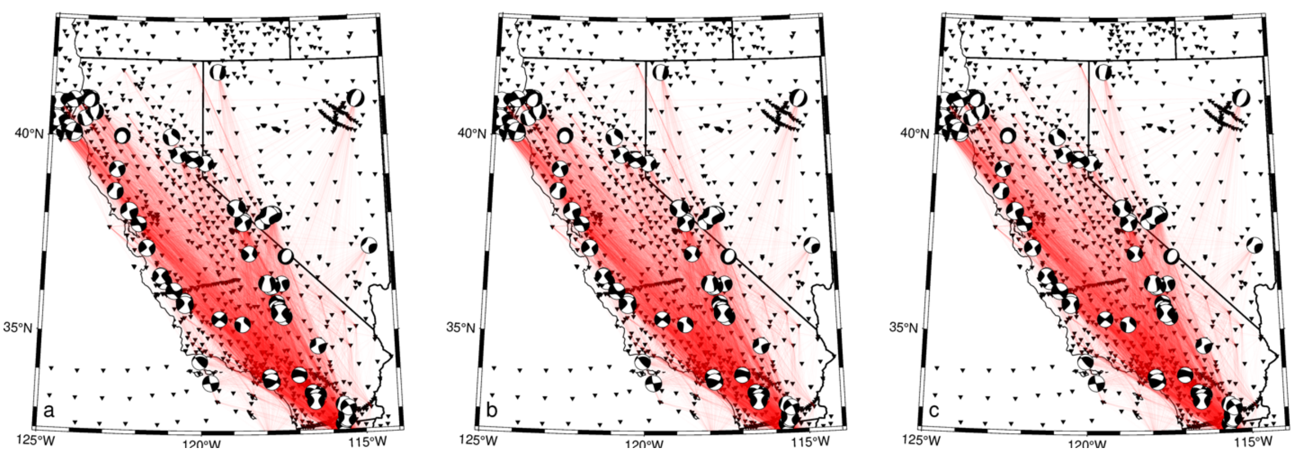

Figure 1.3. Path coverage map for the three final models: (a) CANV_SP, (b) CANV_WUS, and (c) CANV_CS.

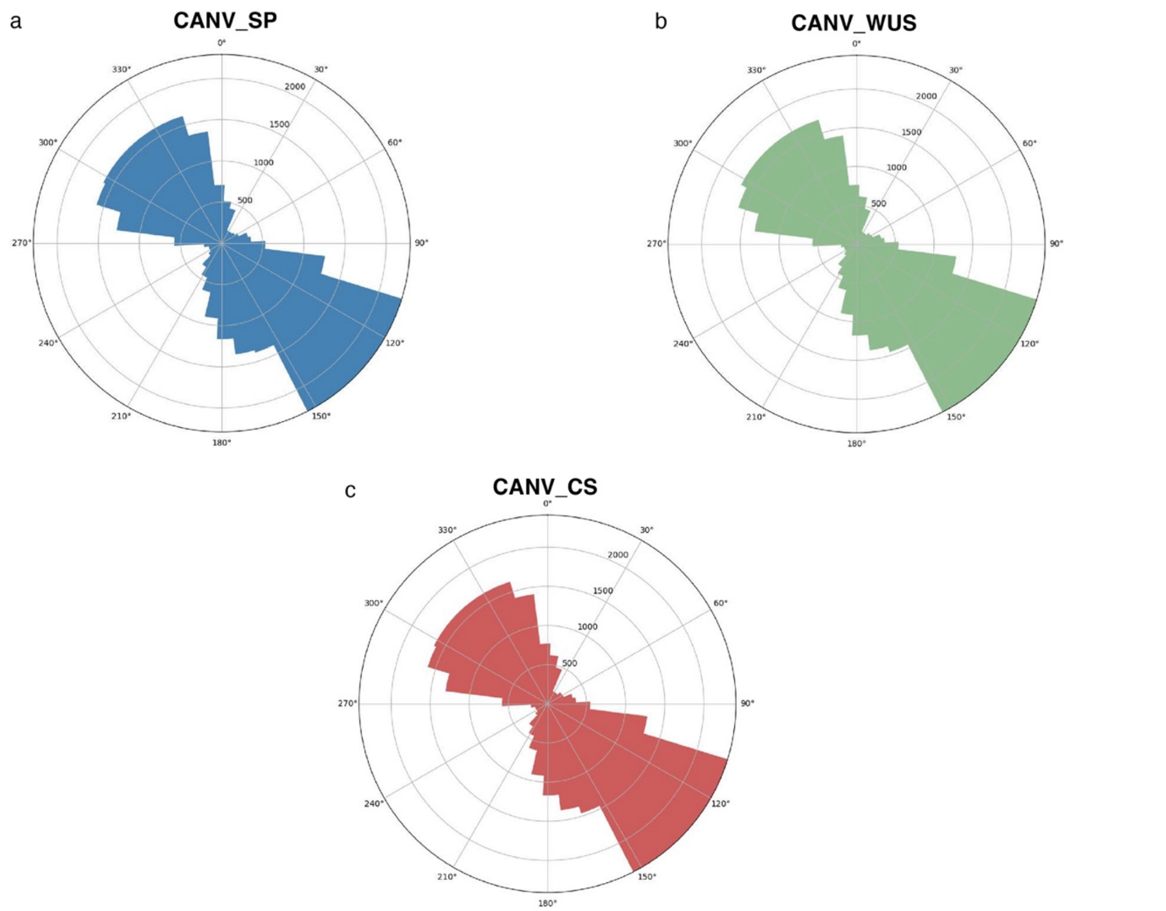

Figure 1.4. Rose diagram showing azimuthal raypath coverage in the three final models. Azimuths are binned in 10° bins; the length of the bars corresponds to the number of raypaths in that azimuth bin.

Figure 1.5 shows the absolute misfit values for the three final models. Figure 1.6 shows the relative misfit reduction of all three final models. The relative misfit (ΔX) at a given iteration *i* is defined as:

$$\Delta X_i = 1 - \frac{X_0 - X_i}{X_0} \qquad (1)$$

Where X_0 is the initial total misfit and X_i is the total misfit at iteration i. Since each model has a different number of iterations, the misfit plot is broken down by period band. At 30-100 seconds, all three models see at least a 30% reduction in misfit, with CANV_WUS reducing misfit by nearly 50%. Because WUS256 is the best-fitting starting model, more windows are picked for smaller events at 30-100 seconds than are picked for CSEM_NA and SPiRaL, resulting in a larger initial misfit for CANV_WUS. By 25-100 seconds and 20-80 seconds, the misfit reduction is smaller for CANV_SP and CANV_WUS. CANV_CS has the largest misfit reduction in these period bands because CSEM_NA is poorly resolved in this region compared to SPiRaL and WUS256.

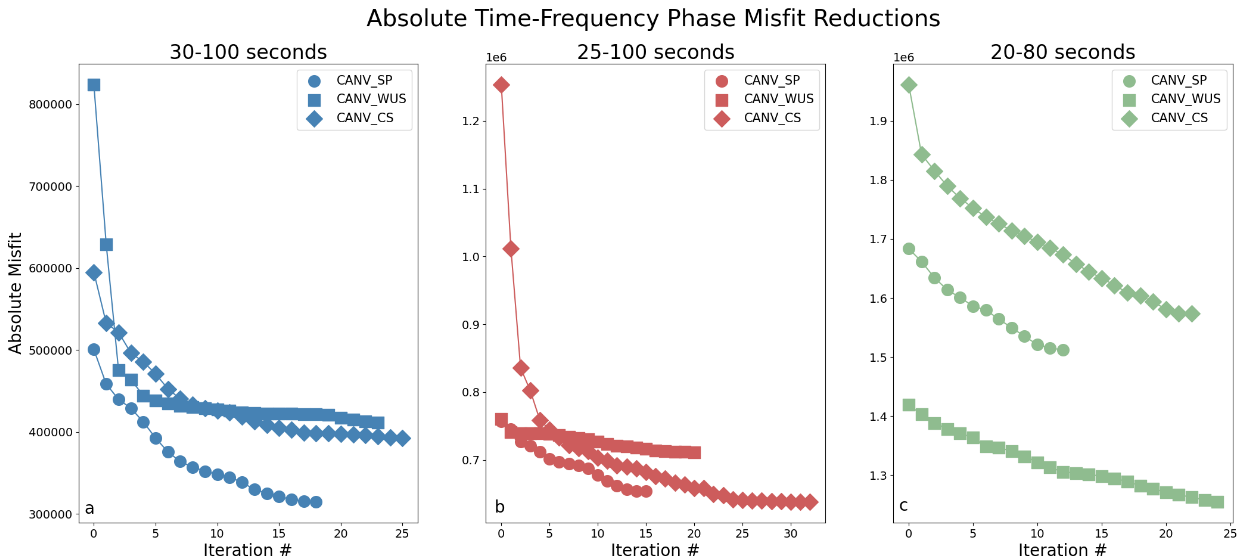

Figure 1.5. Absolute time-frequency phase misfit reduction for the three final models. CANV_SP iterates over a total of 48 iterations, CANV_WUS over 70 iterations, and CANV_CS over 84 iterations in all three period bands. Though CANV_CS has the smallest number of windows, it has the largest misfits due to the original model only being iterated to a minimum period of 30 seconds.

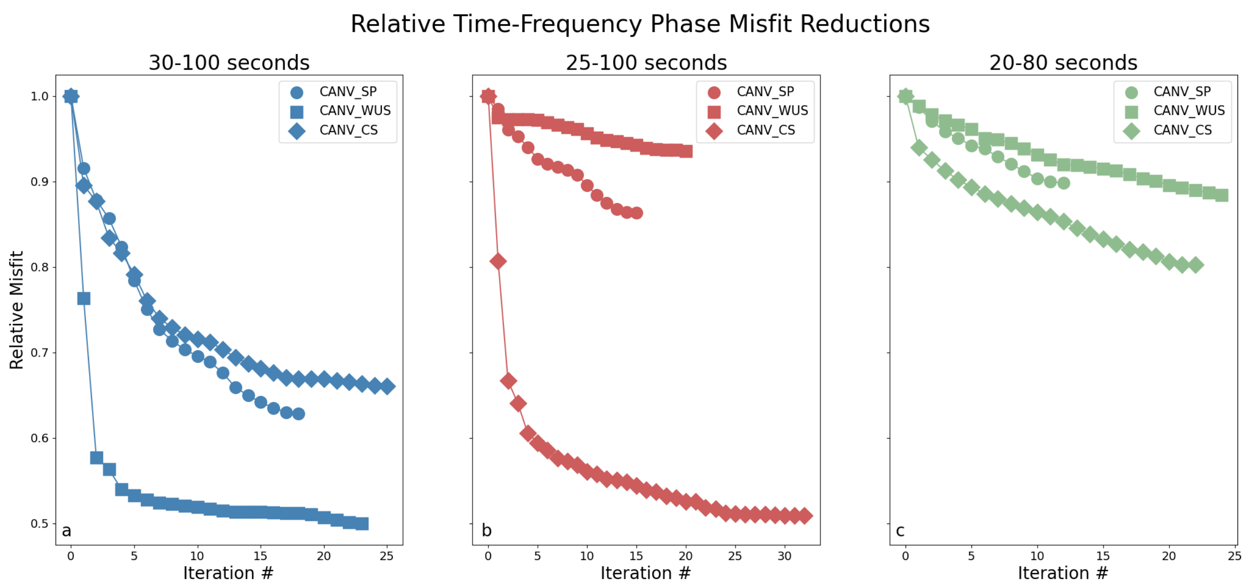

Figure 1.6. Relative time-frequency phase misfit reduction for the three final models. CANV_SP (circles) iterates over a total of 48 iterations, CANV_WUS (squares) over 70 iterations, and CANV_CS (diamonds) over 84 iterations in all three period bands. Though CANV_CS has the smallest number of windows, it has the largest misfits due to the original model only being iterated to a minimum period of 30 seconds.

Figure 1.7 shows the relative Voigt-averaged V_S anomalies in the three starting models (Figure 1.7a-c), the three final models (Figure 1.7d-f), and the natural logarithm ratio of the absolute V_S velocities between the final models and the starting models (Figure 1.7g-i) at 5 km depth. The logarithmic ratio plots show the location and magnitude of updates made compared to the values of the starting model. The updates required to achieve the final model are considerably different depending on the smoothness of the starting model. This indicates that the iterative waveform inversion methodology makes updates to the model based on the structure required by the data.

The three starting models show a large variation in structure. SPiRaL (Figure 1.7a) shows high velocities over most of California, with the lowest velocities off the coast of Cape Mendocino, and the highest velocities under the central Sierra Nevada mountains. WUS256 (Figure 1.7b) shows the highest amplitude and finest scale structure of the three models. The root of the Sierra Nevada mountain range is visible, as well as lower velocities related to the Central Valley. The lowest velocities are under Cape Mendocino, around where the proposed slab window in the Gorda Slab is located (Furlong and Schwartz, 2004) and The Geysers, a geothermal field in central Northern California. Low velocities are also seen under the Long Valley caldera region (e.g., Flinders et al., 2018). Finally, CSEM_NA (Figure 1.7c) has the smoothest structure, with higher velocities in Southern California, and low velocities in northern and northeastern California.

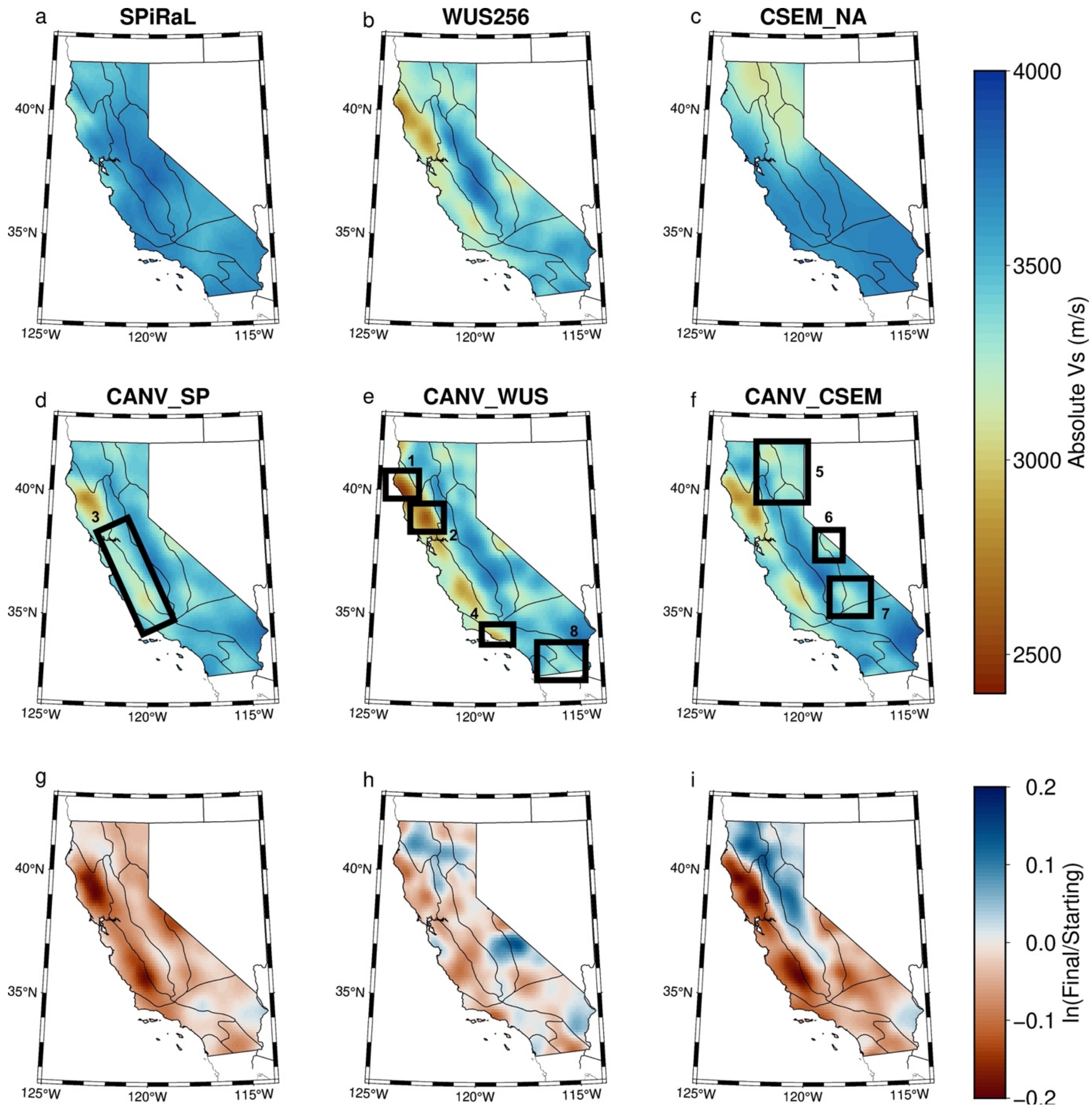

Figure 1.7. Absolute Voight-averaged Vs for the starting models (a-c) and the final models (d-f) at 5km depth. All are plotted on the same scale. Panels g-i show the ratio of absolute Vs values of the final models versus their respective starting models. Red regions show areas where the final model is slower than the starting model; blue regions show areas where the final model is faster than the starting model. The thin black lines in all panels denote the major physiographic regions of California (Fenneman and Johnson, 1946). The bold black boxes in panels d-f highlight major features of the model that are discussed in the text.

Despite the differences in the starting models, the final models resolve similar features in the upper crust (Figures 1.7 and 1.8). All three final models have low velocities along the western coast in the upper crust, corresponding (from North to South) to the Gorda slab window (Box 1, Figure 1.7e; Furlong and Schwartz, 2004), the Geysers geothermal field (Box 2, Figure 1.7e; Majer and McEvilly, 1979; Zucca et al., 1994; Lin and Wu, 2018), and the Central Valley sedimentary basin (Box 3, Figure 1.7d; Lin et al., 2010; Li et al, 2022). CANV_WUS, which starts with WUS256, has the lowest velocities and clearest definition between the Gorda slab window and the Geysers geothermal field. Velocities also appear lower in the Ventura Basin in

CANV_WUS (Box 4, Figure 1.7e), though the basin is smeared because we are only resolving long-wavelength structure. Low velocities in eastern California correspond to volcanic centers. In the northeastern part of the state, lower velocities are seen under Mount Shasta and Lassen volcanic centers (Boxes 5, Figure 1.7f), with differing amplitudes depending on the model. In the central part of eastern California, low velocities under Long Valley Caldera (Box 6, Figure 1.7f) are ringed by the fast velocities of the root of the Sierra Nevada mountains. Low velocities south of the Sierra Nevada mountains likely correspond to the Coso volcanic field (Box 7, Figure 1.7f). Near the border with Mexico, the low velocities in all three models correspond to the Salton Sea region (Box 8, Figure 1.7e); these low velocities are bounded by the San Andreas Fault system, an observation that has also been seen by other workers (e.g., Ajala et al., 2019; Wang et al., 2022).

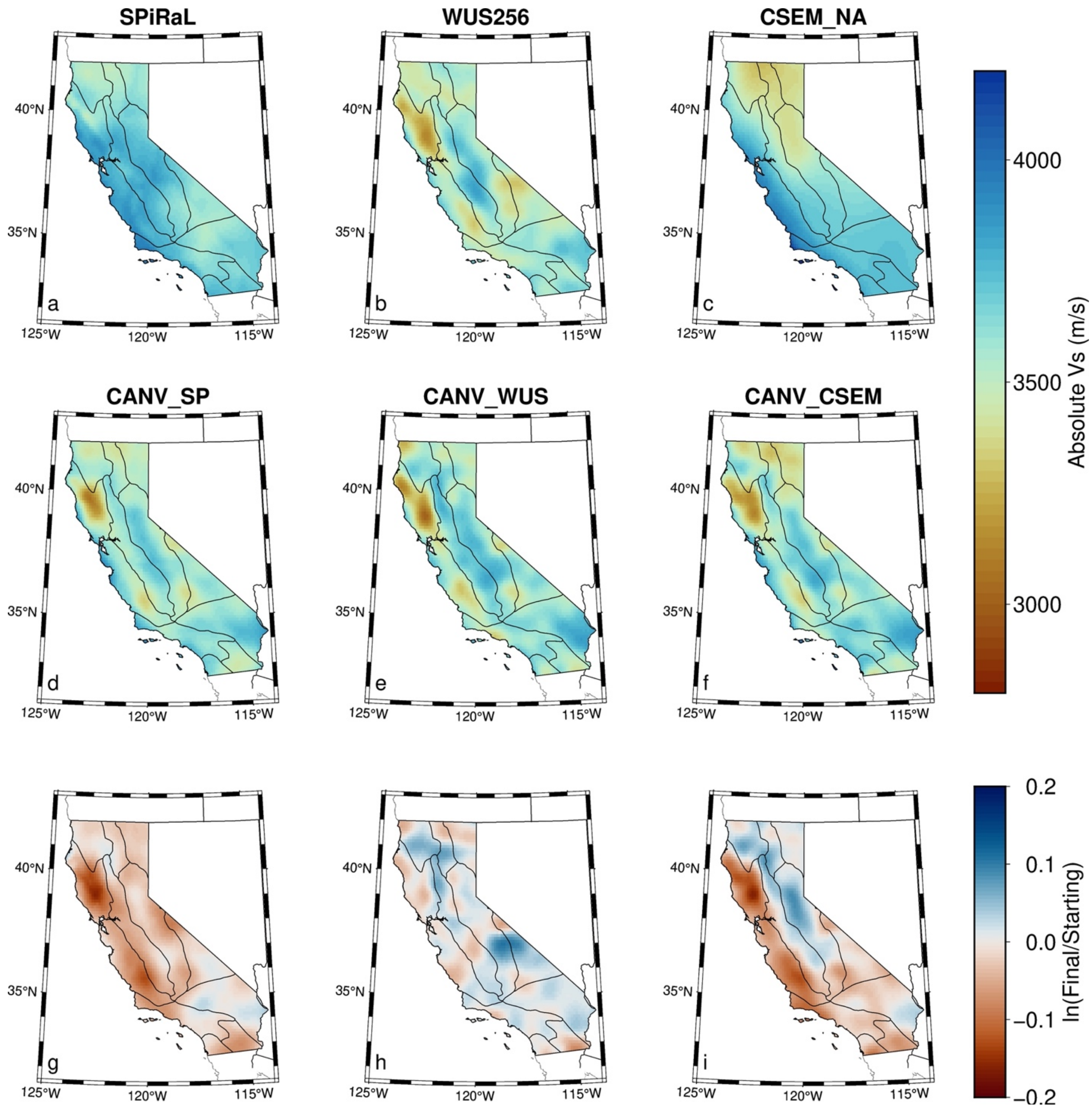

Figure 1.8. Absolute Voight-averaged Vs for the starting models (a-c) and the final models (d-f) at 15km depth. All are plotted on the same scale. Panels g-i show the ratio of absolute Vs values of the final models versus their respective starting models. Red regions show areas where the final model is slower than the starting model; blue regions show areas where the final model is faster than the starting model. The thin black lines in all panels denote the major physiographic regions of California (Fenneman and Johnson, 1946).

The starting models at 55 km depth are also quite different (Figure 1.9a-c). However, the final models also agree with other studies at uppermost mantle depths (Figure 1.9). Beginning in the North, the subducting Gorda slab is visible in the north-central part of the state in all three final models (Figure 1.9d-f). At depths below 60 km, the curvature of the Gorda slab towards the southwest at its southernmost extent is clearly visible in all three final models. The extent and curvature of the slab in the CANV models follows the contours of Slab 2.0 (Hayes et al., 2018); the rotation of the slab is thought to be connected to the slab tear in the Juan de Fuca slab under central Oregon (Hawley and Allen, 2019). For the starting models, WUS256 shows the Gorda slab at the same depths as the final models, while the slab is visible in SPiRaL only at deeper depths (<75km) and CSEM_NA shows anomalous low velocities throughout extent of the Gorda slab (Figure 1.9a-c). Therefore, regardless of the slab's existence in the starting models, the final models are all able to resolve the slab, though with varying amplitudes. All three final models are also resolve the Isabella Anomaly in central California (Box 1, Figure 1.9e). This high-amplitude fast velocity feature is thought to be the detached lithospheric root of the southern Sierra Nevada mountains (Zandt et al., 2004; Jiang et al. 2018; Dougherty et al., 2020). The lithospheric drip is offset to the west from the location of the Sierra Nevada, which is also observed in other studies (e.g., Stanciu and Humphreys, 2021; Rodgers et al., 2022). The high velocity anomaly associated with the Transverse Ranges are also visible (e.g., Kohler, 1999), though not as prominently as the Isabella Anomaly (Box 2, Figure 1.9f). The continuity of the Transverse Range anomaly is interrupted in some of the models by a low velocity anomaly under the Salton Trough (Box 3, Figure 1.9d), which is related to the thin lithosphere and high heat flow in this region (Lekic et al., 2012; Han et al., 2016). These low velocities are likely smeared at these depths, since our period bands of interest give us limited resolution at the upper mantle depths.

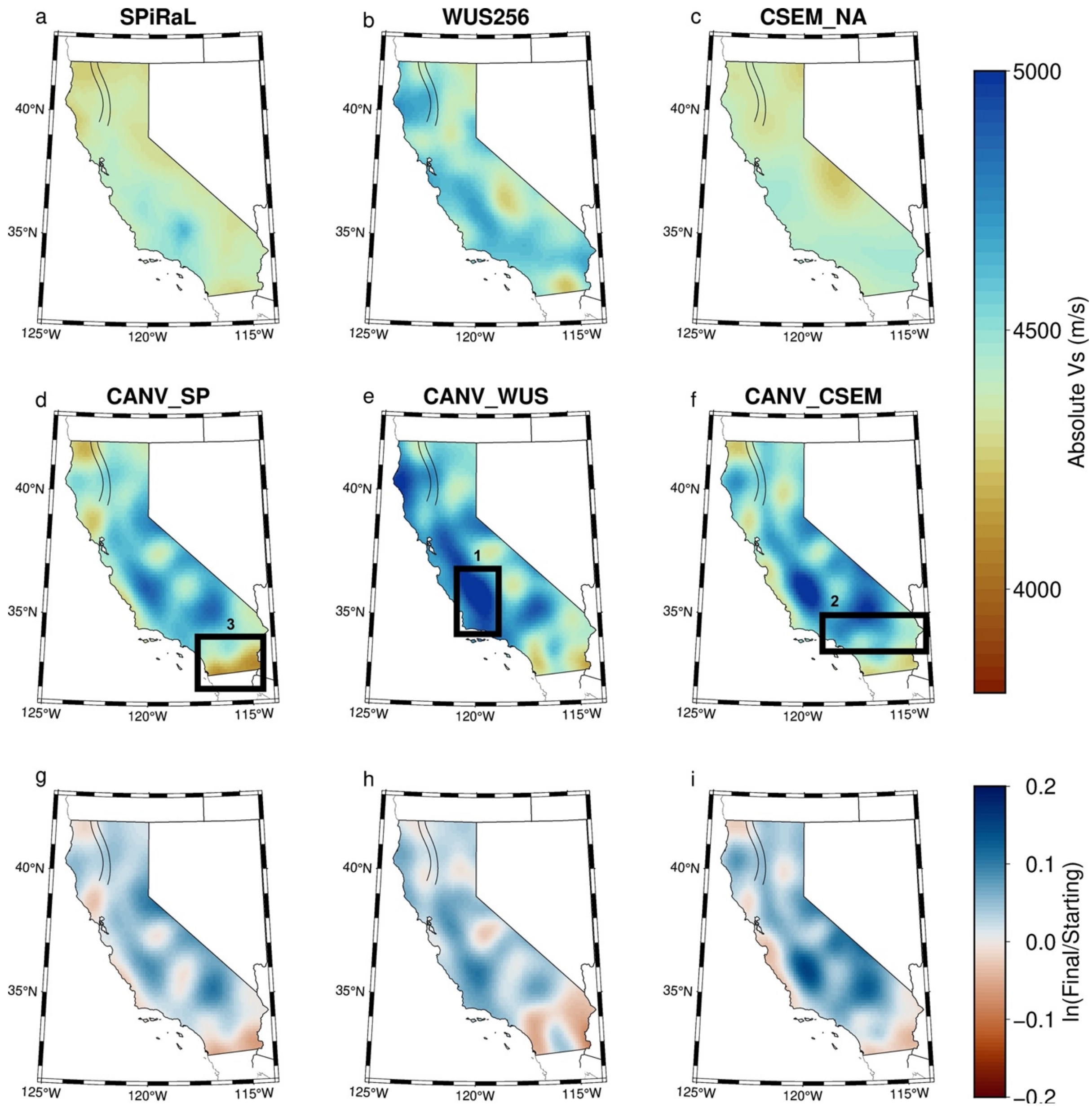

Figure 1.9. Absolute Voight-averaged Vs for the starting models (a-c) and the final models (d-f) at 55 km depth. All are plotted on the same scale. Panels g-i show the ratio of absolute Vs values of the final models versus their respective starting models. Red regions show areas where the final model is slower than the starting model; blue regions show areas where the final model is faster than the starting model. The thin black lines represent the 40km and 60km contour of the Gorda slab from Slab 2.0 (Hayes et al., 2018). The bold black boxes in panels d-f highlight major features of the model that are discussed in the text.

1.5 Model Comparisons

In this section, we compare the resulting three models described in the previous section. Models were compared in both the model space and data space. Comparing the models in model space allows us to view the spatial patterns of the shear wavespeeds and tectonic structures that the models resolve. Comparing the models in data space allows us to determine how well each of the models fits the observed data given the model space differences. Both comparison spaces are vital to understanding whether the models are converging on a similar final result given the different characteristics of each starting model. The comparison methods presented below are not meant to be an exhaustive list of ways to compare seismic tomography models. Some methods, such as K-Means clustering (e.g., Lekic and Romanowicz, 2011) and event-based misfits (e.g. Rodgers et al., 2022) have been used to compare the performance of tomography models before; the structural similarity index (SSIM) (Wang et al., 2004), though broadly applied in the signal processing community, but has not been applied to seismic tomography to our knowledge.

We have focused on methods that are computationally inexpensive, generalizable, and cover a broad range of ways to compare model results. When discussing the comparison results below, we choose not to interpret these results in the context of determining which model has the best performance. What model is the "best" will vary depending on the intended application of the model and chosen metrics. The discussion below is meant to highlight *quantifiable* ways to compare tomography model results through the lens of model convergence. Any discussion of the models outside of their comparison to each other is outside of the scope of this paper.

1.5.1 Model Space Comparisons

1.5.1.1 K-Means Clustering

We begin comparing our models by using k-means clustering (Lloyd, 1982). K-means clustering is frequently used in seismic tomography to both identify tectonic structures in the models (e.g., Chai et al., 2015; Cottaar and Lekic, 2016; Eymond and Jordan, 2019; Lekic et al., 2012; Xiong et al., 2021) and to compare morphologic features between tomography models (Lekic et al., 2012). The shape and characteristic velocities of the clusters provide a qualitative method to determine the models' ability to resolve large-scale tectonic features.

K-means clustering is an unsupervised machine learning algorithm that separates n data points into a user-defined number of clusters k. Data points are segregated into clusters by their squared Euclidean distance (i.e. intra-cluster distance) from a given centroid, or mean, cluster value. This process is then repeated multiple times starting at different mean points. The final cluster results are chosen from the iteration that has the smallest sum of squared Euclidean distance between the centroid and the data points within the clusters. To avoid sub-optimal clustering, we used the k-means++ approach (Arthur and Vassilvitskii, 2007) to choose the initial cluster centroid locations. Unlike traditional k-means, which chooses n number of random centroid locations, k-means++ chooses one random centroid location, and then places the remainder n-1 centroids at the maximum squared distance from the first centroid. This method of choosing initial centroid locations reduces the error at the onset, leading to faster convergence times.

We use the k-means++ algorithm as implemented in Scikit Learn (Pedregosa, et al., 2011) to calculate the clusters in our models. We input profiles of absolute isotropic V_S in the crust (down to 30km) calculated at every 0.1˚ x 0.1˚ in latitude and longitude. We run the clustering algorithm on the dataset for 2, 3 and 4 clusters. The resulting clusters are shown in Figure 1.10.

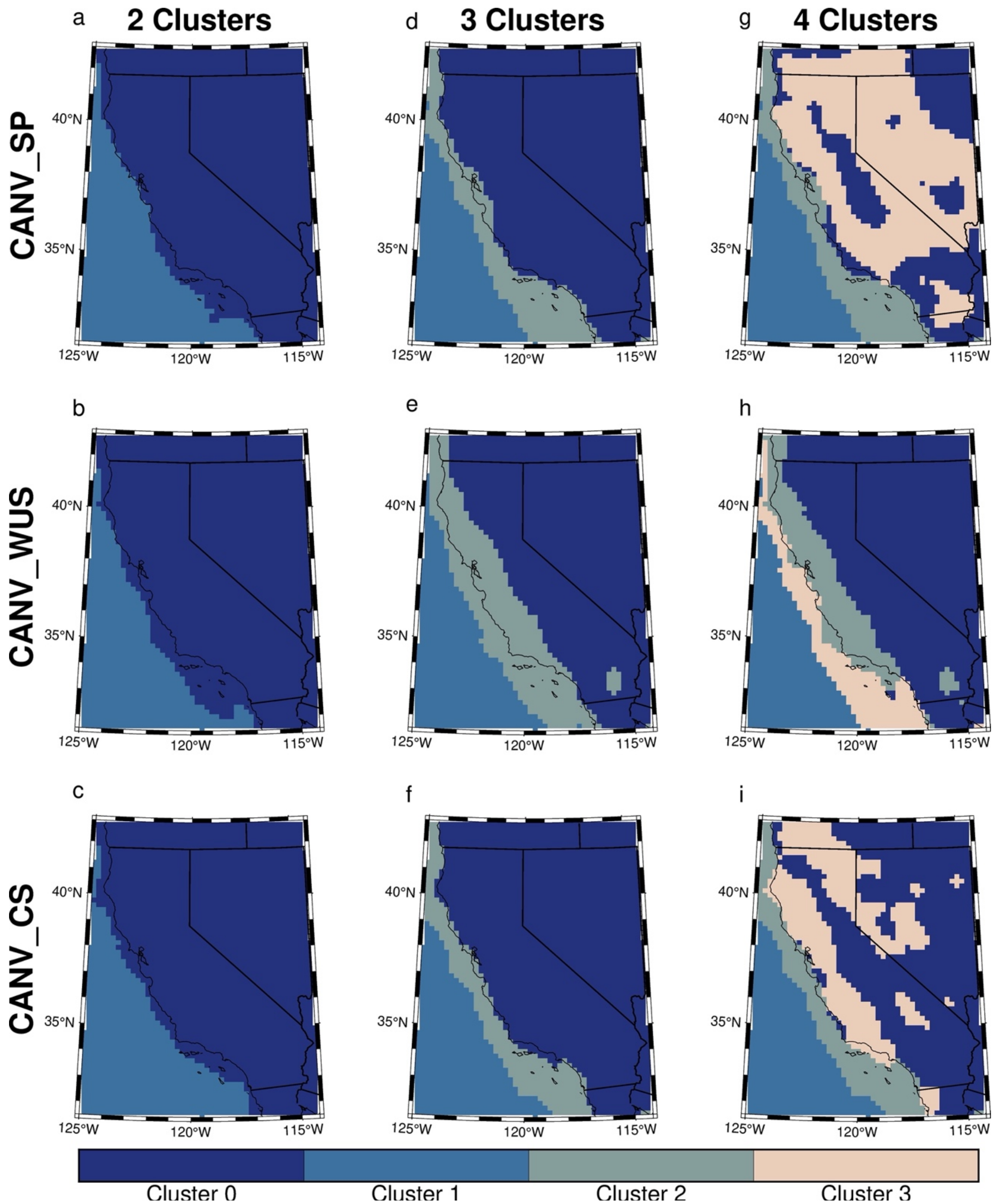

Figure 1.10. K-means clustering of all three final models using 2 (a-c),3 (d-f), and 4 (g-i) clusters.

At *k*=2 clusters (Figure 1.10a-c), all three models have one cluster in the oceanic crust, and the second cluster in the continental crust. Since the Moho depth varies drastically between the oceanic and continental lithosphere, this clustering behavior is expected (Lekic et al., 2012). At *k*=3 clusters (Figure 1.7d-f), the characteristics of the clusters begin to differ between the three models. CANV_SP (Figure 1.10d) and CANV_CSEM (Figure 1.10f) differentiate the continental shelf from the rest of the ocean as their third cluster (see Figure 1.1 for bathymetric map). CANV_WUS also differentiates the continental shelf in its third cluster but includes in that cluster the Coastal Ranges/Central Valley and a small area under the Salton Sea. This is due to the stronger amplitude low velocities in the crust under the coast and Salton Sea in the CANV_WUS model (and WUS256; see Figure 1.7c/d). WUS256 also has lower velocities in the crust under the continental shelf compared to CSEM_NA and SPiRaL.

Finally, at *k*=4 clusters, the clusters align again. All three models retain the ocean, continent, and continental shelf clusters. The fourth cluster for each model clusters around lower velocities under the continent. The extent of these low velocity regions varies between each model. CANV_SP has the low-velocity cluster with the largest extent, covering the Great Valley (Figure 1.7d, Box3), the extensional Basin and Range province in Nevada and easternmost California, and the Salton Sea area (Figure 1.7e, Box 8); the high velocity of the root of the Sierra Nevada is visible (Figure 1.7g) , surrounded by the low velocity cluster described above. These low velocity features have been described in other tomography models of the region (e.g., Chai et al., 2015; Lin et al., 2010; Rodgers et al., 2022). CANV_CSEM similarly clusters the Great Valley and some of the Basin and Range province; this cluster, however, seems to track the artificial low velocities from the starting model in this region. Finally, CANV_WUS only clusters along the Coastal Ranges and Great Valley, not in the Basin and Range province like the other two models. Though the structure of the CANV_WUS model in the Basin and Range province resembles the CANV_SP model, the amplitude of low velocities along the coast is much stronger in the CANV_WUS model, meaning that the clustering algorithm will prefer to cluster these very low velocities together instead of including the smaller low velocity perturbations in the Basin and Range province.

Overall, k-means clustering provides *qualitative* evidence that the three models resolve similar tectonic features. Though variations exist in both the geographic extent and characteristic velocity of the clusters between the three models, these can all be attributed either to variations in the amplitude of velocity features between the three models or to artefacts that are carried over from the starting models in regions where ray path coverage is poor. Regardless of the variations between the models, we can conclude that the models are able to resolve large-scale tectonic structure.

1.5.1.2 Structural Similarity Index (SSIM)

Though k-means clustering can provide a *qualitative* analysis of model similarity, we were interested in a metric to *quantify* the differences between the models. Since it is difficult to compute formal uncertainties for FWI models (see Introduction for discussion on these difficulties), we turned to the structural similarity index (SSIM; Wang et al., 2004) to quantify model similarities and differences. SSIM is an “objective image quality measure” (Wang et al., 2004) that is used to quantify the degradation of a target image in comparison to a reference image. Though other image quality measures exist, SSIM stands out because it considers the human visual perception system’s ability to analyze structural information of an image.

The SSIM value between two images (*x* and *y*) is calculated using the following equation:

$$SSIM(x,y) = \frac{(2\mu_x\mu_y+C_1)(2\sigma_{xy}+C_2)}{(\mu_x^2+\mu_y^2+C_1)(\sigma_x^2+\sigma_y^2+C_2)} \tag{2}$$

where μ_x and μ_y are the average pixel values, or luminance, in a 7x7 pixel window in the reference and target images respectively, and σ_x and σ_y are the standard deviation of the pixel values, or contrast, in the same window for the reference and target images respectively. σ_{xy} is defined as:

$$\sigma_{xy} = \frac{1}{N-1}\sum_{i=1}^{N}(x_i - \mu_x)(y_i - \mu_y) \tag{3}$$

where x_i and y_i are the pixel values. C_1 and C_2 from Equation (1) are constant values; these values are assumed to be very small, so they can be ignored (Wang et al., 2004). The SSIM index is calculated for each 7x7 pixel window, creating a 2D array of SSIM values for the given image; a singular SSIM value is calculated by averaging the values over space. Applying SSIM values locally and averaging the values instead of running the calculation globally is advantageous for multiple reasons, but most importantly it provides a spatial map to compare the (dis)similarity between the two images. SSIM values range from 0 to 1, with 1 meaning that the images are identical and 0 meaning that the images are completely different (e.g., comparing an apple to a building). Figure 1.11 provides an example of images with different SSIM values to contextualize the results of comparing the starting and final models below.

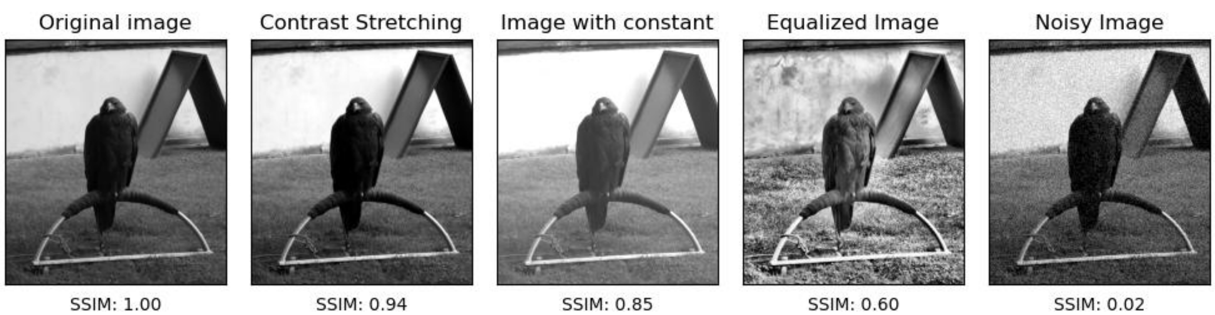

Figure 1.11. An example of structural similarity index values for a picture of an eagle taken from scikit-learn's image library (Pedregosa et al., 2011). The first panel is used as the ground truth against which all other images are compared. Aside from the first panel, the images have been altered in a variety of ways to change the luminance of pixels and the contrast between neighboring pixels, which affect the global SSIM value.

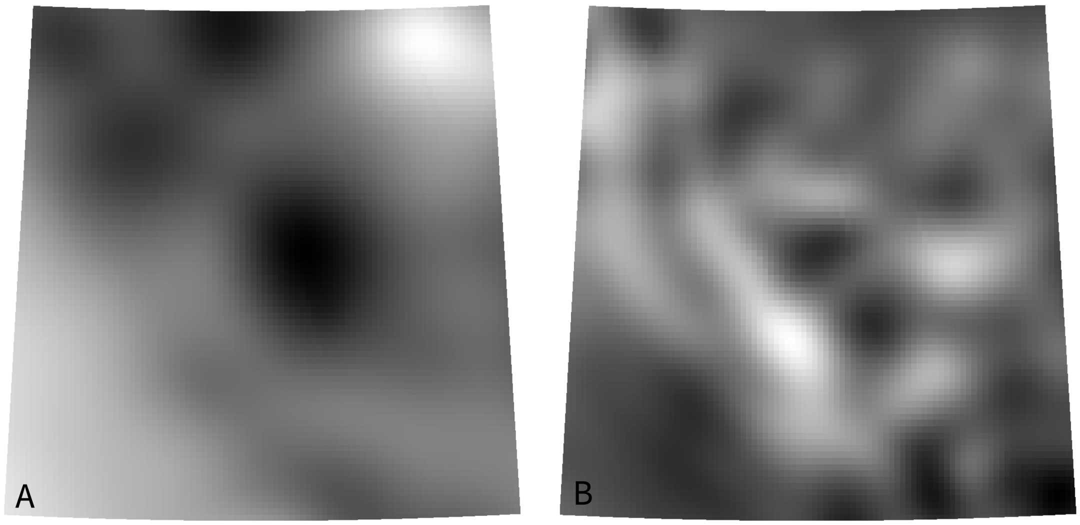

Figure 1.12. Example of input image for structural similarity index calculation. The image shown is of the CSEM_NA model (Panel a; Krischer et al., 2018) and the CANV_WUS model (Panel b) at 55km depth over the entire model domain; the two images have an SSIM value of 0.85. The values shown are of absolute isotropic Vs; all starting and final models are plotted on the same scale. The images are plotted in grayscale to enhance contrast.

To determine the SSIM values of the respective tomography models, we extract the absolute V_S values for each starting and final model from 5km to 75km in 5km intervals. The V_S values were plotted using PyGMT (Uieda and Wessel, 2019) in grayscale over our domain (see Figure 1.12). Once the images were created, the SSIM value was calculated for each model pair at each depth; the results with depth are shown in Figure 1.13 and grouped by starting models, starting and final models and final models in panels a, b, and c, respectively.

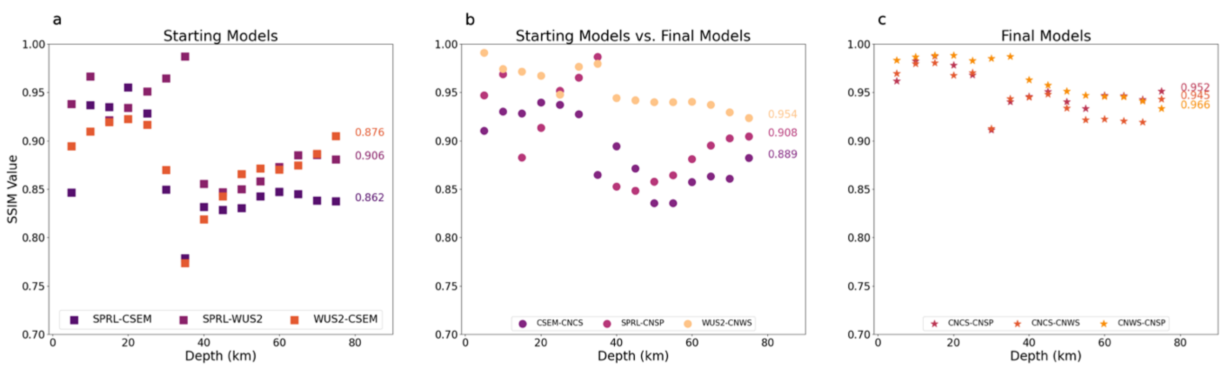

Figure 1.13. SSIM values vs. depth for all model-model permutations. The values at the far right of each panel are the average SSIM value over all depths for the given models. a) SSIM values for the starting models compared to each other, b) SSIM values for the starting models compared to the final models, and c) SSIM values for the final models compared to each other.

For the starting models compared to each other (Figure 1.13a), SPiRaL and WUS256 have the highest average SSIM value over all depths with an average value of 0.91. The values are highest in the crust, where smaller updates are made because of the minimum period band of WUS256 (20 seconds). The SSIM value of WUS256 compared to SPiRaL are very high between 25-35km, which coincides with the Moho depths in the model; the Moho topography imposed is the same for WUS256 and SPiRaL, which results in a high structural similarity value. The SSIM values of SPiRaL and WUS256 compared to CSEM are lower but have similar average values (0.88 for WUS256 vs. CSEM_NA and 0.86 for SPiRaL vs. CSEM_NA). WUS256 shows more similarity to CSEM_NA at uppermost mantle depths (>50 km), whereas SPiRaL shows more similarity to CSEM in the crust. SSIM values for both WUS256 vs. CSEM_NA and SPiRaL vs. CSEM_NA are low at Moho depths. CSEM_NA does not have the Moho topography imposed in the model, which creates this discrepancy.

For the starting models compared to the final models (Figure 1.13b), there is a larger variability between the SSIM values. WUS256 shows the highest average SSIM values compared to all three final models (0.9-0.95), especially in the crust. Since WUS256 is already well resolved, the model space updates made to create CANV_WUS are smaller than the other final models (see Figure 1.5 for misfit plot), which results in higher SSIM values. The SSIM values for CSEM_NA compared to CANV_CS are the lowest, indicating that large changes were made to the CSEM_NA model to arrive at CANV_CS (consistent with Figure 1.7i and 1.8i). CSEM_NA is only iterated down to a minimum period of 30 seconds, and so is unlikely to resolve the smaller-scale structures that the three models produced in this study can resolve. The SSIM values of CSEM_NA compared to the final models are also far lower at Moho depths because of the lack of Moho topography in CSEM_NA. The SSIM values for SPiRaL compared to CANV_SP fall between those of CSEM_NA and WUS256 compared to the final models. The SSIM values of SPiRaL compared to CANV_SP drop significantly after 35km, then increase again towards 75km. Though SPiRaL and CANV_SP show similar tectonic structure in the upper mantle, the range of velocities in the two models vary (Figure 1.9a/d/g). Therefore, the low SSIM values are attributable to the amplitude difference between SPiRaL and CANV_SP. The SSIM values increase with depth since we have limited resolution below 60km, which means that deeper depths will resemble the starting model more. This trend can be seen at upper mantle depths when comparing CSEM_NA and CANV_CS as well. The SSIM values for WUS256 compared to CANV_WUS are relatively flat below the Moho, which can be attributed to WUS256's high resolution in the uppermost mantle.

The SSIM values of the final models compared to each other show far less variability with depth than either the starting models compared to themselves, or the starting models compared to the final models. All final model comparisons have SSIM values above 0.9, with the lowest values around Moho depths. These values are likely due to residual artefacts from CSEM_NA's lack of Moho topography. The SSIM values for the final models are higher in the crust than they are in the uppermost mantle. Because we start our iterations at 30 seconds minimum period and our maximum period extends only to 100 seconds, the surface wave sensitivity is concentrated in the upper 60 km of our models. Therefore, the lower SSIM values and larger variability below the Moho are inherited from the starting models.

Overall, the analysis of the models using SSIM allows us to *quantify* the differences between the models in model space based on their visual characteristics. The SSIM analysis shows that all three final models are more visually similar to each other than they are to the models they start from. The SSIM values are particularly high in the crust of the final models, where we have the highest resolution, with values of above 0.95 for all three final model permutations in the upper

25km of the models. Therefore, we can quantitatively confirm that the final models strongly resemble each other in model space.

1.5.2 Data Space Comparisons

With k-means clustering and the structural similarity index, we have shown that the models are *qualitatively* and *quantitatively* similar in model space. However, model space comparisons do not give any information on waveform fits or data-space convergence of the models. Therefore, we propose three methods of data-space comparison to examine the goodness of fit of the starting models and final models compared to the observed data. All three of these methods have been used in other studies to determine improvements in fit in tomography models, and we believe that these three measures–windowing statistics, event-based misfits, and variance reductions of waveform differences–provide well-rounded insight into the convergence of the three models in the data-space, irrespective of the differences seen in the model space.

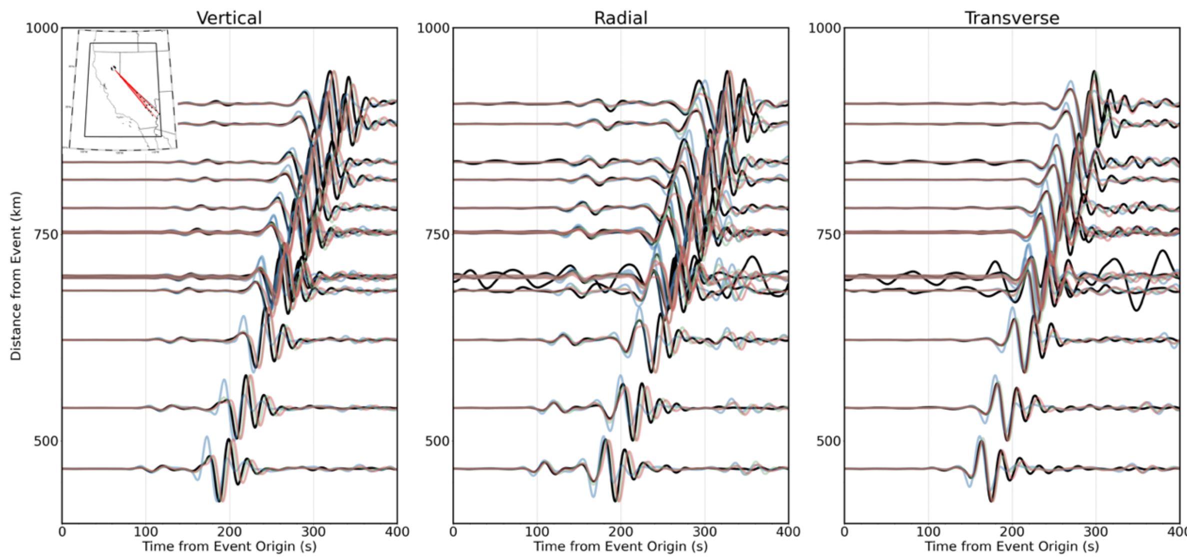

Figure 1.14. Waveforms for the starting models for the 24 May 2013 Mw 5.72 earthquake in Canyondam, California (inset map). The stations plotted are in the back azimuth range of 130˚-140˚ at distances greater than 400km from the epicenter (see inset map). Black seismograms represent the observed data, blue seismograms are synthetics from SPiRaL (Simmons et al., 2021), green seismograms are synthetics from WUS256 (Rodgers et al., 2022), and red seismograms are synthetics from CSEM_NA (Krischer et al., 2018).

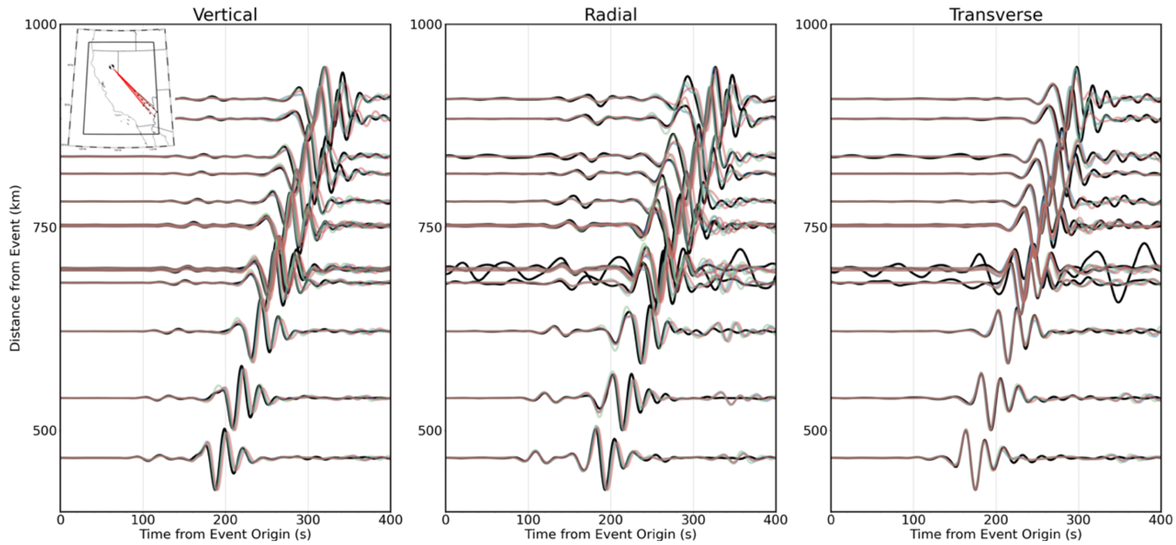

Figure 1.15. Waveforms for the final models for the 24 May 2013 Mw 5.72 earthquake in Canyondam, California (inset map). Black seismograms represent the observed data, blue seismograms are synthetics from CANV_SP, green seismograms are synthetics from CANV_WUS, and red seismograms are synthetics from CANV_CS.

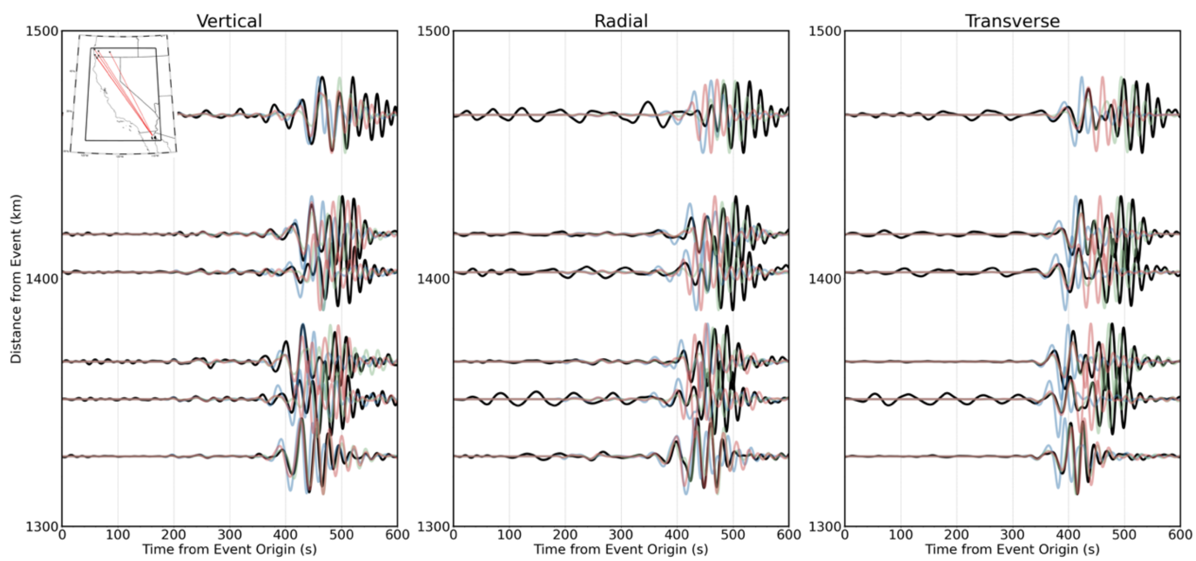

Figure 1.16. Waveforms for the starting models for the 18 February 2011 Mw 5.15 earthquake in Baja California (inset map). The stations plotted are at distances greater than 1325km from the epicenter (see inset map). Black seismograms represent the observed data, blue seismograms are synthetics from SPiRaL (Simmons et al., 2021), green seismograms are synthetics from WUS256 (Rodgers et al., 2022), and red seismograms are synthetics from CSEM_NA (Krischer et al., 2018).

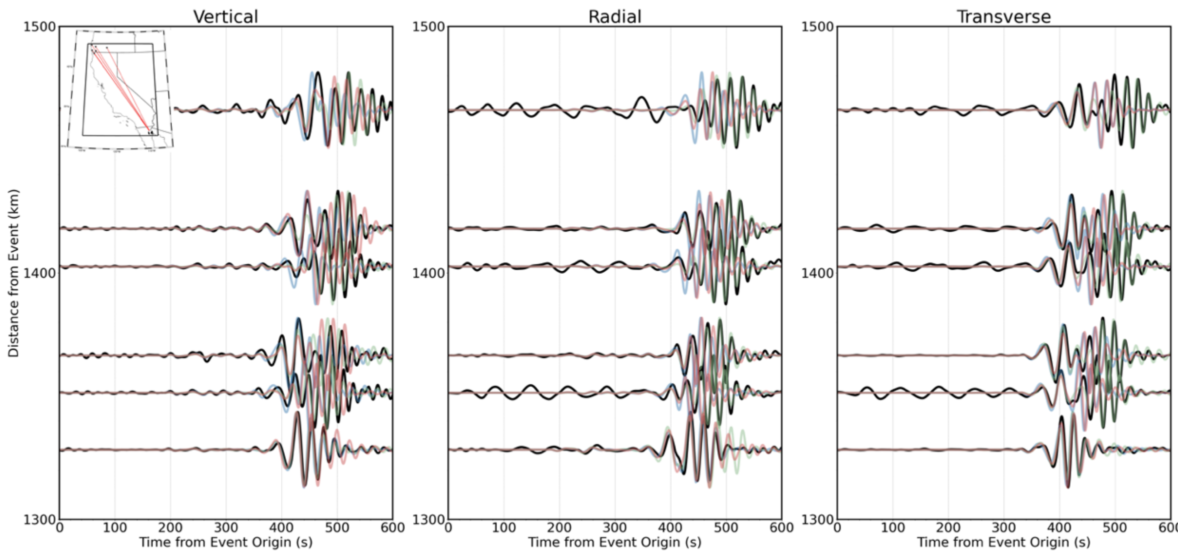

Figure 1.17. Waveforms for the starting models for the 18 February 2011 Mw 5.15 earthquake in Baja California (inset map). The stations plotted are at distances greater than 1325km from the epicenter (see inset map). Black seismograms represent the observed data, blue seismograms are synthetics from CANV_SP, green seismograms are synthetics from CANV_WUS, and red seismograms are synthetics from CANV_CS.

1.5.2.1 Windowing Statistics

As discussed in the Methods section, each inversion picks an independent window set based on the synthetics of the given model (see Figures 1.14-1.17 for examples of synthetic waveforms). We chose not to standardize the windows for each inversion for two main reasons: to avoid incorporating cycle skipping and noise if using windows based on body/surface wave travel times and to avoid biasing the results towards one model by picking the window set of one model and standardizing it across the rest of the models. By not standardizing the windows across all models, we will inevitably include different data in the inversions as each starting model and interim model will correlate to the observed data differently. If the models reach convergence, however, we expect that we will have a similar set of windows, as the simulated waveforms will have the same response, therefore correlating to the observed data in the same way.

To test the similarity of the final waveforms in the data space, we re-ran our window picking algorithm on the final models as well as the starting models using a mesh resolving 20s minimum period. Before analyzing the results, we will briefly comment on the window picking methodology. The window picking algorithm used by Salvus is adapted from the Large-scale Seismic Inversion Framework (LASIF; Krischer et al., 2015).

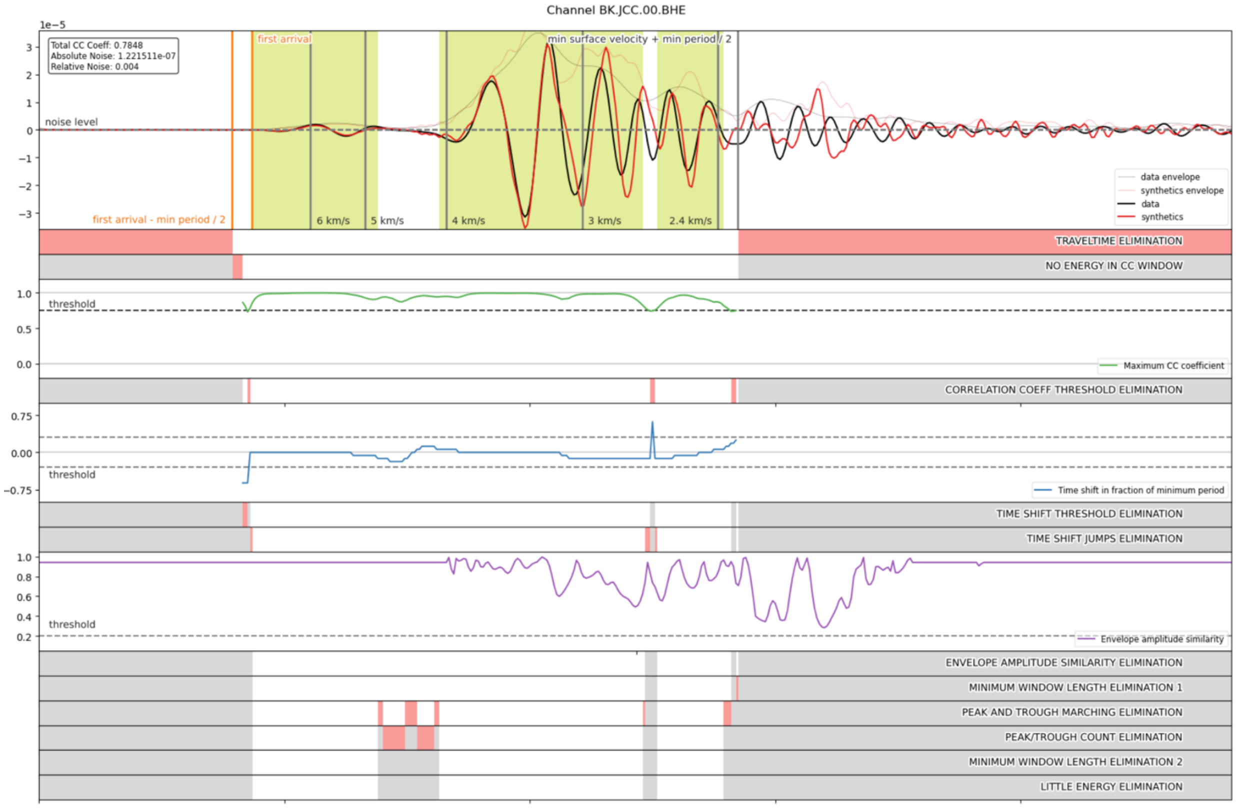

Figure 1.18. Visual example of window picking criteria. The waveform shown is for the east component of BK.JCC for a Mw 5.50 event in Central California on 4 June 2020. The synthetic data shown is for CANV_WUS; the observed and synthetic data are bandpass filtered between 20 and 80 seconds. The 11 criteria used to pick the final window set are listed on the righthand side of each row. Areas of a row that are red indicate that the given portion of the waveform does not fit that criterion, and so is therefore excluded from the final windows. The final windows chosen are highlighted in green.

Window selection is broken into three stages: using travel times to find the bounds where we can pick windows, determining global rejection criteria that would prevent windows from being picked for a given waveform, and a set of acceptance/rejection parameters that determine what parts of the waveform are suitable to be windowed (see Figure 1.18 for visual representation). For the first step of calculating the time window for which we can pick windows, the first arrival time is calculated using ak135 (Kennett et al., 1995) and a minimum surface wave speed is set by the user (2.4km/s in this study). A buffer of half the minimum period is added to both ends to determine the time period over which windows can be picked. Any part of the waveform before the first arrival – buffer or after the minimum surface wave arrival + buffer is excluded. Once the area over which we can window is calculated, the algorithm then moves on to determining whether the data quality is good enough to pick windows for that waveform. Data quality is determined using a normalized cross-correlation value of the observed and synthetic data (see Equation 1, Krischer et al., 2015) and the relative noise level of the data, which is calculated by taking the ratio of the maximum amplitude of the waveform prior to the first arrival and the maximum amplitude of the waveform in the travel time-bounded window. The minimum normalized cross-correlation value and maximum noise level are determined by the user. If the waveform has a high enough cross-correlation value and low enough noise level, we can then move on to picking the windows for that waveform.

The built-in window picking function in Salvus uses nine parameters to constrain windows. Three parameters control the initial window candidates: the cross-correlation values across the waveform calculated using a sliding window cross-correlation approach (see Equations 2 and 3, Krischer et al., 2015), the time shift between the observed and synthetic data in the sliding window, and the envelope amplitude similarity in the sliding window. The thresholds are set by the user. Candidate windows are then refined by minimum window length, time difference between matching peaks, minimum number of peaks and troughs in the window, and the energy ratio of the maximum amplitude within the window and the absolute noise prior to the first arrival. If the proposed window fits all the above criteria to the user-defined thresholds, then a window is picked.

Inversion Events

Total Number of Cells

	SPiRaL	***CANV_SP***	*WUS256*	***CANV_WUS***	*CSEM_NA*	***CANV_CS***
Z	24862	**30391**	29335	**32359**	23906	**31455**
N	17605	**21305**	20869	**21082**	16221	**21490**
E	17411	**20872**	20785	**21371**	16108	**21031**
Total	59878	**72568**	64724	**74812**	56235	**73976**

Time-Bandwidth Product (days-Hz)

	SPiRaL	***CANV_SP***	*WUS256*	***CANV_WUS***	*CSEM_NA*	***CANV_CS***
Z	0.534	**0.835**	0.789	**0.965**	0.549	**0.91**
N	0.376	**0.594**	0.597	**0.669**	0.366	**0.615**
E	0.381	**0.596**	0.065	**0.675**	0.365	**0.614**
Total	1.282	**2.025**	1.992	**2.309**	1.28	**2.138**

Validation Events

Total Number of Windows

	SPiRaL	***CANV_SP***	*WUS256*	***CANV_WUS***	*CSEM_NA*	***CANV_CS***
Z	3714	**4543**	4176	**5076**	3275	**4457**
N	2787	**2953**	2930	**2953**	2324	**3090**
E	3155	**3272**	3156	**3272**	2867	**3361**
Total	9656	**10768**	10262	**11496**	8466	**10908**

Time-Bandwidth Product (days-Hz)

	SPiRaL	***CANV_SP***	*WUS256*	***CANV_WUS***	*CSEM_NA*	***CANV_CS***
Z	0.077	**0.117**	0.109	**0.137**	0.077	**0.12**
N	0.06	**0.091**	0.086	**0.101**	0.055	**0.092**
E	0.078	**0.106**	0.1	**0.112**	0.071	**0.111**
Total	0.216	**0.315**	0.294	**0.35**	0.203	**0.323**

Table 1.1. Window picking statistics at 20-80 seconds for the starting models and the final models. Table 1.1a shows the total number of windows picked in each component across all station-event pairs for the starting and final models. Table 1.1b shows the time-bandwidth product (days-Hz) in each component over all the picked windows.

With the details of the window picking algorithm in mind, we turn to the results of the window picking. Table 1.1 shows summary statistics for the windows picked from the starting and final models. We chose to analyze two different metrics of the final window sets: the total number of windows picked by each model and their time-bandwidth product. The time-bandwidth product (total window duration times the frequency bandwidth) provides a measure of the information content in the signals that is explained by a given seismic model. The total duration of selected windows based on a common event, path and receiver data set and the same window picking algorithm provides a quantitative metric of waveform fit performance.

The starting models have different characteristics in terms of the number of windows picked and the time-bandwidth product. CSEM_NA picks the least number of windows overall and has the shortest time-bandwidth product (i.e. the least amount of information included in the window set). Even though CSEM_NA is an adjoint tomography model that is optimized to fit waveforms, it is only iterated down to 30 seconds minimum period, and so is very smooth when meshed at

20 seconds. We therefore do not expect to have as many windows from CSEM_NA as SPiRaL and WUS256, which both contain shorter period data. WUS256 contains the most number of windows and includes the most data out of all three starting models. Compared to CSEM_NA and SPiRaL, WUS256's window set contains 8,500 more windows and 19 more days of data—more than 50% of the data contained in CSEM_NA's window set. SPiRaL has roughly 3,000 more windows than CSEM_NA, but has a similar time-bandwidth product, indicating that SPiRaL picks shorter windows than CSEM_NA and WUS256.

Compared to the differences between the starting models, the final models show remarkable similarity in number and duration of windows. All three models pick around 74,000 windows (an average of ~2 windows per station-event pair), with CANV_SP picking the least number of windows, and CANV_WUS picking the most. CANV_WUS performs the best of the three models both in terms of the number of windows picked and the amount of information contained in those windows. WUS256 has shown better data fits than both SPiRaL and CSEM_NA (Rodgers et al., 2022), leading CANV_WUS to include more surface wave dispersion data in the windows than the other final models. CANV_WUS includes 14% more data than CANV_SP and 8% more data than CANV_CS. Compared to the spread in time-bandwidth product between the starting models, the variation in the final models is minimal.

To test our models' fit on independent data, we created a validation dataset of events that were not included in the inversions. Our validation dataset is composed of 15 events that occurred between 1 November 2020 and 28 February 2022. We use the same domain and magnitude constraints as our inversion dataset for the validation dataset. We chose not to include events that occurred prior to 1 January 2000 in our validation dataset because recent events have nearly 3 times as many stations contributing data compared with events in the 1990s due to the explosion of broadband stations in California for earthquake early warning (e.g., Strauss and Allen, 2016).

The trends seen in the windowing statistics for the inversion dataset also apply to the validation events. WUS256 picks the most number and duration of windows of the three starting models, amounting to 29% more information included in the window set compared to CSEM_NA. As for the final models, both CANV_WUS and CANV_CS contain nearly identical amounts of data in the east component, though CANV_WUS still picks more data in the vertical and north components. CANV_SP picks the least amount of data in the validation dataset, but still has similar statistics to CANV_CS in terms of number of windows picked and time-bandwidth product.

To summarize, window picking statistics serve as a proxy for waveform fit in both our inversion dataset and validation dataset. The window picking statistics in the final models closely resemble each other in both absolute number of windows and the time-bandwidth product of the windows for both datasets. Therefore, we can extrapolate that the three final models are moving towards the same window set independently. It is also important to note that all three final models also include more data than any of the starting models. This means that all three final models fit the waveforms better than our best-fitting starting model, regardless of the resolution of their respective starting models.

1.5.2.2 Inversion and Validation Event Misfits

While window picking statistics provide a proxy for the similarity of waveform fits in the time-domain, it does not provide a quantitative measure of the misfit between the observed data and our models. Therefore, we compute both the time-frequency phase misfit (Fichtner et al., 2008) and a normalized L2 misfit for all models for both the inversion and validation datasets. Comparing the mean misfit values for each event allows for a more detailed understanding of the fit of the final models to the observed data.

Because the traditional L2 misfit is heavily biased towards high amplitude–and therefore near-source–receivers, we use a normalized L2 misfit, which compares the similarity in waveform shape between the observed and synthetic data. Normalizing the L2 misfit allows for an equal contribution of far-field stations to the total misfit value for a given event, providing a better proxy for how each model fits the data at all stations. To be able to compare the models fairly, we calculated both the time-frequency phase misfit and normalized L2 misfit values for each model using the window set of WUS256. We chose to use the windows from WUS256 because it has the highest number of windows and best waveform fits out of the three starting models. We did not to use a window set from one of the final models so as not to bias the comparison of the final models. The results of the event-based misfit calculations are shown in Figure 1.19. Figure 1.19 shows the cumulative misfit per event for SPiRaL and CSEM_NA (dashed lines) and the three final models (solid lines). Misfit values are plotted relative to the misfit values of WUS256 for both the inversion and validation datasets.

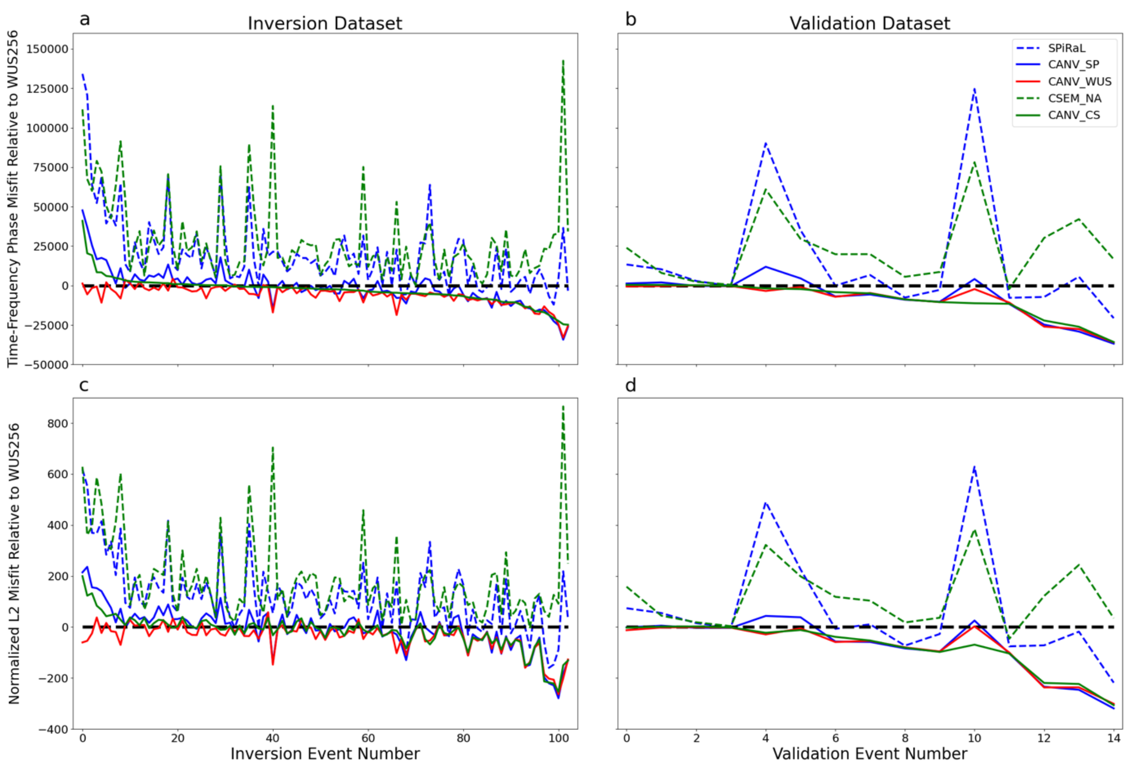

Figure 1.19. Cumulative misfit per event for the inversion dataset (a and c) and the validation dataset (b and d) relative to the misfit values of WUS256 (Rodgers et al., 2022). Figures 1.19a and 1.19b show the time-frequency phase misfit values (Fichtner et al., 2008) for both datasets plotted on the same scale; Figures 1.19c and 1.19d show the normalized L2 norm values for both datasets plotted on the same scale. Dashed lines indicate starting models, while solid lines indicate final models.

The most striking feature of the misfits is both the variability of misfit values for the starting models and the marked consistency of the misfit values of the final models. Both the time-frequency phase misfit and normalized L2 misfits show similar trends on an event-by-event basis for both the inversion and validation datasets.

SPiRaL and CSEM_NA have higher misfit values compared to WUS256 for most events in both the inversion and validation datasets. The misfit values are highest for CSEM_NA, indicative of poorer fit to the data than SPiRaL or WUS256. SPiRaL also has consistently higher misfit values than WUS256; as with the other statistics discussed, we expect WUS256 to have a lower misfit than SPiRaL because WUS256 uses SPiRaL as its starting model. The large spikes in misfit for SPiRaL and CSEM_NA do not seem to have a trend by location. The misfit for the SPiRaL and CSEM_NA tends to be higher for larger events (Mw<6.0). This is likely a breakdown of the point source approximation for larger magnitude events, and so are not able to capture the complexity of these waveforms.

The misfit values for the final three models follow the same trend for both the inversion and validation datasets. The misfits for CANV_SP and CANV_CS tend to be higher than that of CANV_WUS, especially for events where the starting model has spikes in the misfit values. All three models have misfit values that are lower than WUS256 in 40% of the inversion events and 67% of the validation events. The smaller percentage of events where all three models have lower misfits than WUS256 in the inversion dataset is affected mainly by larger misfit values for CANV_SP and CANV_CS. These higher misfit values correlate with events where SPiRaL and CSEM_NA have anomalously high misfit values.

The most striking feature of the misfit values across the inversion and validation datasets is the consistency in misfit values across the final models. The consistency in misfit values points to the similarity in final model waveforms regardless of the misfit in the starting models. Therefore, we provide more evidence that the final models are converging towards the same model in the data space.

Calculating the event-based misfit for the starting and final models confirms the results from the window picking statistics comparison: regardless of the misfit values of the starting models, the final models have lower misfits than their respective starting models, and often perform better than WUS256. Therefore, the event-based misfits provide quantitative confirmation of the similarity in waveform fits of the three final models, and therefore the convergence of the three final models towards the same model.

1.5.2.3 Envelope Similarity of Synthetic vs. Observed Data

The previous two sections have covered waveform fits based on the goodness of fit for the observed and synthetic waveforms for a given model(s). To get an objective view of waveform fit across the whole waveform, we compared the envelope of the observed data with both our starting and final models. Comparing envelopes allows us to determine the similarity between both the phase and amplitude of the waveforms, allowing for an unbiased measure of waveform fit.

To calculate the envelopes, we began by removing any station-event pair where the signal-to-noise ratio (SNR) of the observed data was less than 10. We chose to remove these data to ensure that noisy data would not skew the interpretation of the results. After we removed noisy data, we windowed our data over the whole waveform. We chose this window to include wave speeds between 8 km/s and 2 km/s for each station-event pair. This section of the waveform captures most of the seismogram and corresponds to the high and low wave speed limits of our models. Windowing by wave speed assures an unbiased comparison of the synthetic data regardless of the similarity of the synthetic and observed data. Once the data is windowed, we compute the envelope for the observed data as well as all for the starting and final models. Each envelope is computed by squaring the amplitude of the data, taking its Hilbert transform, and then taking the square root (Kanasewich, 1981). To determine the similarity of the envelopes, we calculate the Pearson correlation coefficient (Pearson, 1895) for the envelope of the observed data versus the synthetic data. The Pearson correlation coefficient, known better as the cross-correlation coefficient, is a measure of the normalized covariance of two datasets:

$$r = \frac{\sum_{i=0}^{i=n}(x_i-\underline{x})(y_i-\underline{y})}{\sqrt{\sum_{i=0}^{i=n}(x_i-\underline{x})^2(y_i-\underline{y})^2}} \tag{4}$$

where x_i is the ith value of the observed envelope, $\underline{x}$ is the mean value of the observed envelope, y_i is the ith value of the synthetic envelope for a given model, and $\underline{y}$ is the mean value of the synthetic envelope. Cross-correlation values range from -1.0 (anti-correlated) to 1.0 (perfectly correlated). For the purpose of this study, we only look at positive cross-correlation values. Station-event pairs with negative cross-correlation values account for less than 2% of the total station-event pairs, so do not affect the interpretation of the results.

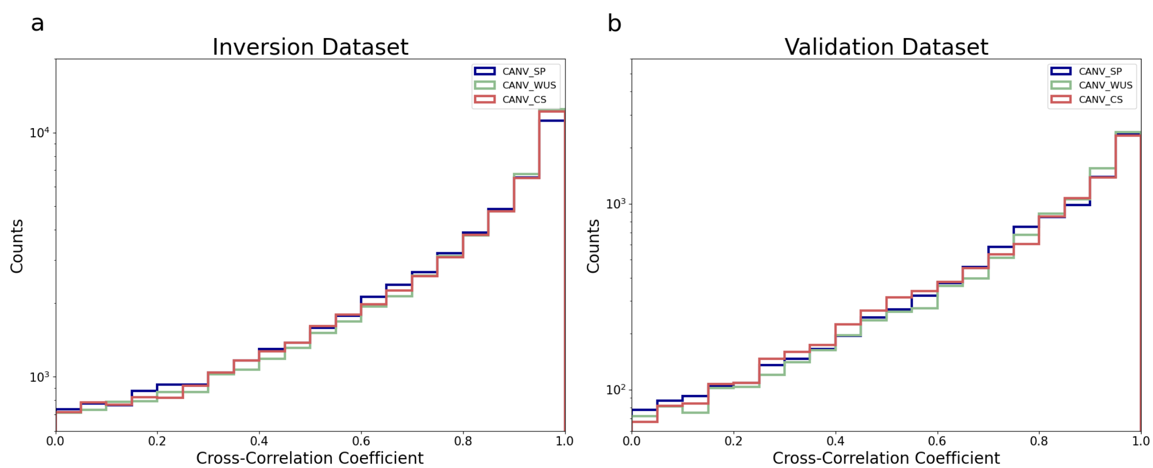

Figure 1.20. Histograms for the Pearson cross-correlation values for the envelopes of the observed data versus the envelopes of the final models. The total counts (y-axis) are plotted on a logarithmic scale. Correlation coefficients are binned by 0.05, for a total of 20 bins. Histograms for the inversion dataset (left column) and validation dataset (right column) have different scales.

Figure 1.20 shows a histogram of the number of station-event pairs that fall into each cross-correlation value bin for the three final models. The counts in each bin show little variability in both the inversion and validation datasets. The cross-correlation values in the inversion dataset show nearly identical values from 0.75 to 1.0. CANV_SP has a lower number of waveforms that have cross-correlation values between 0.95 and 1.0 compared to CANV_WUS and CANV_CS. This observation is consistent with results from automated window picking, where CANV_SP performed slightly poorer than the other two models (Table 1.1). Even with slightly lower values in the highest cross-correlation value bins, the majority of CANV_SP's waveforms have cross-correlation values above 0.6, which suggests that the waveforms are still well-correlated to the observed data.

From the comparison of the final models against each other, we can extrapolate that the waveforms across the final models are similar to each other over the whole waveform window, not just in windows chosen based on the similarity between observed and synthetic data. It is important to emphasize that based on the cross-correlation values, we show that all areas of the waveform, not just the sections included in the automated window set, are highly correlated to the observed data. The cross-correlation values for the starting models are variable (see Figure A.1), yet the final models all converge towards similar values regardless of where they start from.

Comparing the envelopes of the observed and synthetic data over the whole waveform window provides an unbiased confirmation of improved waveform fits for the CANV* models. The envelope cross-correlation, combined with the misfit values and window picking statistics, provide strong evidence that all three CANV* models are moving towards the same Earth model. Adjoint waveform tomography is dependent on a starting model, and we have shown that regardless of the smoothness or artefacts seen in the starting model, a multi-scale approach can resolve discrepancies in tectonic structure and waveform fits.

1.6 Conclusions

Adjoint waveform tomography relies on a starting model to begin inversions. However, previous studies have only considered a single starting model beyond the forward modelling stage because of computational cost. In this study, we used an efficient AWT workflow to investigate the impact of the starting model on the resulting Earth model and waveform fit. We considered three starting models for a broad region covering California. We found that the models resulting from a conservative, multiscale inversion approach show good agreement by measures of Earth model similarity (model space) and waveform simulation performance (data space). The three models were able to overcome smoothness and artefacts in the respective starting models to produce three models that contain similar tectonic features and comparable waveform fits in California. This is the first AWT study to explicitly consider three different starting models and demonstrate the robustness of AWT to obtain consistent results.

To compare the results of the three models produced, we were interested in providing quantitative methods of determining similarity in both the model space and data space. Comparing seismic velocity models has often relied on qualitative comparisons such as the similarity of tectonic structure to other models or visual comparison of waveform fits for select source-receiver pairs. In this paper, we proposed five methods of comparison–both qualitative and quantitative–for determining the similarity of different seismic models. We used k-means clustering and structural similarity (SSIM) index analysis to show that the three final models can resolve large-scale tectonic features to a high degree of similarity both qualitatively and quantitatively. To determine the similarity of waveform fits, we studied windowing statistics, event-dependent misfit values, and envelope similarity. All three methods produce the same result: the CANV* models perform equally well at fitting the data, even outside of the windowed portions of the data.

The performance of the CANV* models suggests that we can converge towards a similar model regardless of the starting model used. However, there are important caveats to consider with these results:

- Station/Event Coverage- California provide impressive station coverage and good azimuthal coverage for events, and so is an ideal environment for adjoint waveform tomography. In an environment with poor station coverage or azimuthally restricted sources, the choice of starting model will likely have a bigger influence.
- Methodology- Methodology- We chose to take a careful multi-scale approach to our inversions, both in terms of the data that we include and the inversion steps we make. We allowed the L-BFGS algorithm to choose the step-size at each iteration, closely monitoring and confirming that the predicted and actual misfit reduction were consistent. This approach led to more iterations than are commonly seen in contemporary work, but we believe that this careful path through misfit space is a key factor in starting model independence.
- Wavelength- The final models we present are iterated down to 20 seconds minimum period, which is low resolution for a regional velocity model. Artefacts in the final models that are related to the starting models are likely to have a greater effect at shorter periods, where data are more complex and affected by small-scale structures. Because of the computational cost of running three California-scale models to short periods, we suggest using a smaller region where many starting models are available (e.g., Southern California) to test the effect of starting models down to 5 seconds or below. We defer this question to a later study.

With these caveats in mind, we argue that the choice of starting model has minimal effect on the final inversion results at long periods. This implies that adjoint methods can resolve artefacts in starting models, and we can be confident that we are marching towards a global minimum with conservative iteration approaches. This also suggests that all starting models are in the locally convex region of the misfit functional, which also justifies the use of uncertainty quantification using a Gaussian approximation and information derived from the Hessian (Bui-Thanh et al., 2013). The minimal effect of the starting model also means that starting with a one-dimensional starting model (e.g., Boehm et al., 2022; Metivier et al., 2016) is not required to minimize artefacts of the starting model in areas with dense ray coverage. 1D starting models require significantly more iterations due to the layered structure and lack of lateral heterogeneity; using a 3D starting model will minimize computational time while still not contributing artefacts

1.7 Acknowledgements

Simulations were run on the Lassen GPU-accelerated platform operated by Livermore Computing. This work was supported in part by Lawrence Livermore National Laboratory Directed Research and Development project 20-ERD-008. This work was performed under the auspices of the U.S. Department of Energy by Lawrence Livermore National Laboratory under Contract DE-AC52-07NA27344. C. Doody is also supported under SCEC Award #22130. We thank the associate editor and two anonymous reviewers for their helpful comments.

Chapter 2

Moment tensor catalogue for California and Nevada using 3D Green's functions

2.1 Abstract
Moment tensors provide valuable information on fault properties, magnitude, and stress regimes in tectonically active regions. Traditionally, moment tensor Green's functions are calculated using one-dimensional velocity models that do not take into account lateral heterogeneity in the Earth. To produce more accurate moment tensors, we used CANVAS, an adjoint waveform tomography model of California and Nevada, to calculate 3D Green's functions. We inverted moment tensors for 115 local events in California and Nevada ranging from Mw4.5-6.5 using MTTime (Chiang, 2020), a time-domain moment tensor inversion code. The resulting moment tensor catalogue has an average variance reduction of 80% and has magnitude and depth values that are similar to local catalogue solutions. 3D Green's functions also allow waveform fits out to great distances (>800km) from the source, which has implications for improved moment tensors for offshore events or for events where local station data are not available.

2.2 Introduction
Moment tensors are mathematical representations of earthquake source characteristics, with the earthquake approximated as a point source; they provide valuable information on source properties ranging from fault type to moment magnitude. Moment tensors are visualized as beachballs, where the shading represents the radiation pattern from the source (see Figure 2.1). Moment tensors are vital to full waveform inversion seismic tomography, where accurate source parameters are necessary to simulate accurate synthetic seismograms (Dziewonski et al., 1981).

Traditionally, researchers have used the Global Centroid Moment Tensor (GCMT) catalogue (Dziewonski et al., 1981; Ekström et al., 2012) to provide source parameters. The GCMT catalogue is advantageous because the solutions are produced rapidly and are of consistent quality across all regions. However, there are inherent problems with the GCMT catalogue that hinder its ability to provide accurate solutions. Firstly, the GCMT Green's Functions are calculated in a 1D Earth model with 3D path corrections, not in a fully 3D model (Dziewonski et al., 1981; Hjorleifsdottir and Ekstrom, 2010; Ekström et al., 2012; Sawade et al., 2022). Multiple studies have shown that the GCMT method for moment tensor calculation leads to overestimated scalar moment in continental events, as well as systematic overestimation of the depth and centroid time of events (Hjorleifsdottir and Ekström, 2010; Sawade et al., 2022). 3D Green's Functions also better predict amplitude (Abercrombie and Ekström, 2001; Dalton and Ekström, 2006) and moment tensor orientation (Foster et al., 2014). GCMT solutions are also calculated using long-period teleseismic data, which may not be accurate enough to resolve smaller magnitude events (M_W<5.0). Therefore, updating sources in seismic tomography models is highly advantageous to remove as much error from the source as possible.

In this study, we used `mttime`, a time-domain moment tensor inversion code (Chiang, 2020), to compute moment tensors in California and Nevada using 3D Green's Functions. The 3D Green's Functions are computed using CANVAS (Doody et al., 2023), an adjoint waveform tomography model of California and Nevada, which is obtained by successive iterations down to a minimum period of 20 seconds. In order to decrease the minimum period band in CANVAS, recomputing sources was necessary to remove source errors that could affect the ability to accurately model shorter period seismograms. This study presents those recomputed sources. Firstly, we look at two events to highlight the power of 3D Green's Functions to be able to resolve moment tensors that are similar to local catalogue solutions in the region. We then show that the 3D moment tensor solutions perform well using only distant stations and have more consistent waveform fits than 1D moment tensor solutions. Finally, we compare the inverted MTTime solutions to the GCMT solutions to illustrate the ability of 3D Green's Functions to produce results that better model observed waveforms. Calculating moment tensors using 3D Green's Functions could allow us to obtain more accurate source mechanisms for events where nearby stations do not exist or are inaccessible.

2.3 Methods

`mttime` is a python package for time-domain moment tensor inversion code (Chiang, 2020). It uses complete seismic waveforms to invert for the moment tensor; the methodology used is based on Time-Domain Moment Tensor (TDMT; Dreger et al., 1998; Dreger and Woods, 2002; Dreger, 2003). TDMT is widely used in regional moment tensor inversion (Fukuyama et al., 1998; Pasyanos et al., 1996; Sccognamiglio et al., 2009; Tajima et al., 2002). `mttime` uses the Kikuchi and Kanamori (1991) approach to moment tensor parameterization. This method parameterizes the moment tensor as a linear combination of six basis Green's functions; the advantage of this approach is that each subgroup of the system has a specific solution such that the linear inversion can be parameterized to solve the generalized complete moment tensor. The Kikuchi and Kanamori approach allows for the use of 3D Green's functions, which take advantage of the lateral heterogeneity that exists in tectonically complex regions such as California and Nevada. It also allows for the computation of either deviatoric or full moment tensors. Since all earthquakes in this study are tectonic, we opt to compute deviatoric moment tensors, but hope to explore the full moment tensors in a later study.

We invert for events between Mw4.5-6.5 that occurred between 1 January 2000 and 31 October 2020. 103 of the events were used in the inversion of CANVAS, the adjoint waveform tomography model of California and Nevada that we use to calculate 3D Green's functions. The remaining 12 events were excluded from the original inversion dataset because they did not pass quality control (i.e., low signal-to-noise ratio). We began the inversion process by choosing stations for the inversion; instead of using all available stations, we binned stations by their distance and azimuth from the source. Each bin covered 30˚ azimuth and 200km distance, with a maximum distance of 1200 km from the source. We then calculated the signal-to-noise ratio (SNR) at each station by averaging the SNR of all three components; the station with the highest SNR in each bin is chosen for the inversion. Though stations were distributed in distance, the location of the source restricted the azimuthal distribution of the stations; events that occurred in Baja California, for example, consistently had fewer stations used in the inversions than events that occurred in the Walker Lane region of eastern California. Therefore, the number of stations used in the inversion varied from 8 to over 40 stations depending on azimuthal coverage.

3D Green's functions were calculated using CANVAS (Doody et al., 2022). The Green's functions were calculated at 1km depth increments ranging from 1km to 30km; for events that occurred in Mendocino or for events where the GCMT depth was below 25km, we extended the Green's functions down to 45km depth. We then inverted moment tensors for all depths using the pre-selected stations. We inverted the moment tensors in the 20-50 second period band and used 300 seconds of data sampled to 1sps. If the inversion included stations that were >1000 km from the source, we used 400 seconds of data for all stations. We inverted for deviatoric moment tensors for all sources.

The best-fitting moment tensor solutions are picked based on a few criteria: the variance reduction, the double couple percentage, and the depth similarity to local catalogue solutions. We begin by looking for the solutions with the highest variance reduction, indicating the best waveform fits. As we are mainly interested in improved sources to improve waveform fits for further iterations of CANVAS at shorter periods, waveform fit was the most important factor in choosing a preferred solution. For depths that have similar variance reductions, we choose the solution with the highest double couple percentage even if the variance reduction is marginally lower. We choose events with high double couple percentages because our dataset is tectonic, and so therefore should be mostly double couple. In areas known for lower double couple percentages (e.g. the Geysers, Walker Lane), we relax constraints around double couple values. If the solution with the highest variance reduction/double couple percentage combination differs by more ±5 km from the GCMT depth, we compare the depth to local catalogue solutions. We do not limit our solutions to be within a given depth range of the GCMT or local solution depths; however, we will preferentially pick solutions that are similar in depth to other trusted solutions. To compare the inverted solutions with the GCMT solutions originally used to calculate CANVAS, we forward modelled the GCMT solutions onto the stations used in our inversion to compare the waveform fits of the two solutions.

2.4 Results

2.4.1- Case Studies: Santa Barbara and Mendocino

We present summary results of our moment tensor inversions below. Because of the large number of moment tensors calculated in this study, we will cover two moment tensors in depth and then provide summary statistics for the entire moment tensor catalogue. However, we will also compare the inverted solution with local catalogue solutions from the Advanced National Seismic System (ANSS), which includes solutions contributed from the Northern California Earthquake Data Center (NCEDC) and the Southern California Earthquake Data Center (SCEDC). We show that the inverted solutions from this study more closely match local catalogues than the GCMT.

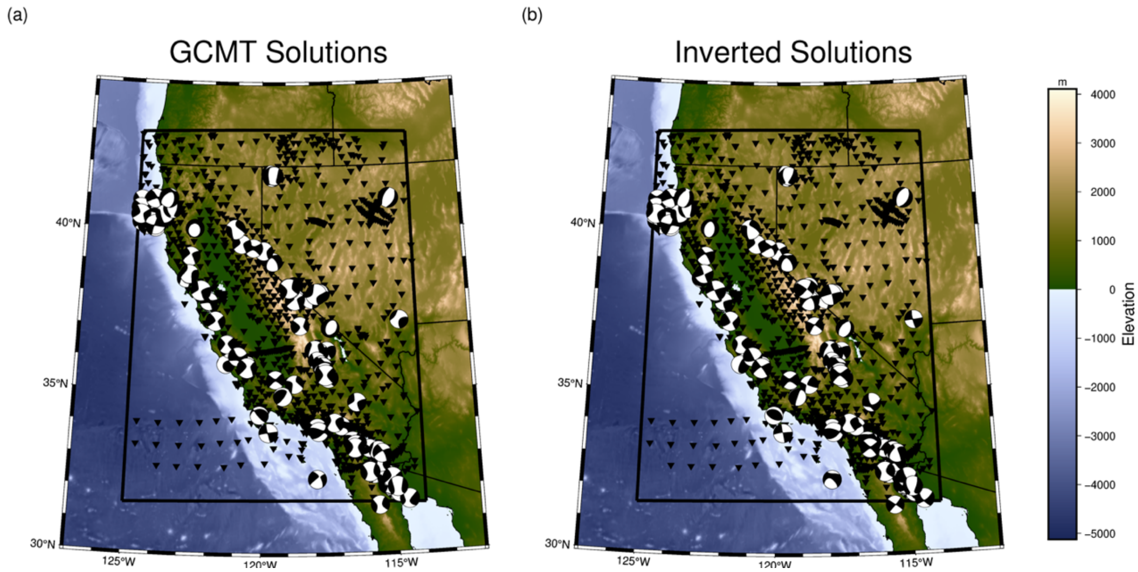

Figure 2.1. Beachball diagrams of 115 earthquakes from (a) the Global Centroid Moment Tensor (GCMT) catalogue, and (b) the results of this study. Black inverted triangles indicate stations with available data across all events. The bold black box indicates the extent of CANVAS; all events and stations are located within this domain.

Figure 2.1 shows beachball diagrams for the 115 moment tensors calculated in this study. Compared to the GCMT solutions, the solutions from this study show broad agreement with the GCMT mechanisms in terms of focal plane orientations. Strike, dip, and rake angles are broadly consistent between the GCMT and this study, suggesting that fault planes in the GCMT catalogue are already well-resolved. Visual comparison of the events also show that the inverted solutions tend to have a larger double couple (DC) component than the GCMT solutions. One of the primary factors in determining the best-fitting solutions for this study was high DC percentage, which can explain the overall higher double couple percentage.

To compare waveforms, we begin by looking at the results for the 29 May 2013 Mw 4.8 earthquake that occurred off the coast of Isla Vista, CA. Station coverage for this event is extensive, with stations spanning 180˚ of azimuth and out to distances of over 1000km (Figure 2.2b). 18 stations were originally picked for the inversion (Figure 2.2b); 4 stations were removed due to poor waveform quality. Waveform data from the 13 remaining stations were inverted at depths of 1km to 30km; the best fitting solution was chosen at 14km depth. The solution at 14km depth had the highest variance reduction of all solutions. Two solutions at 12km and 15km depth had higher DC%, however, the difference is negligible at such high DC values.

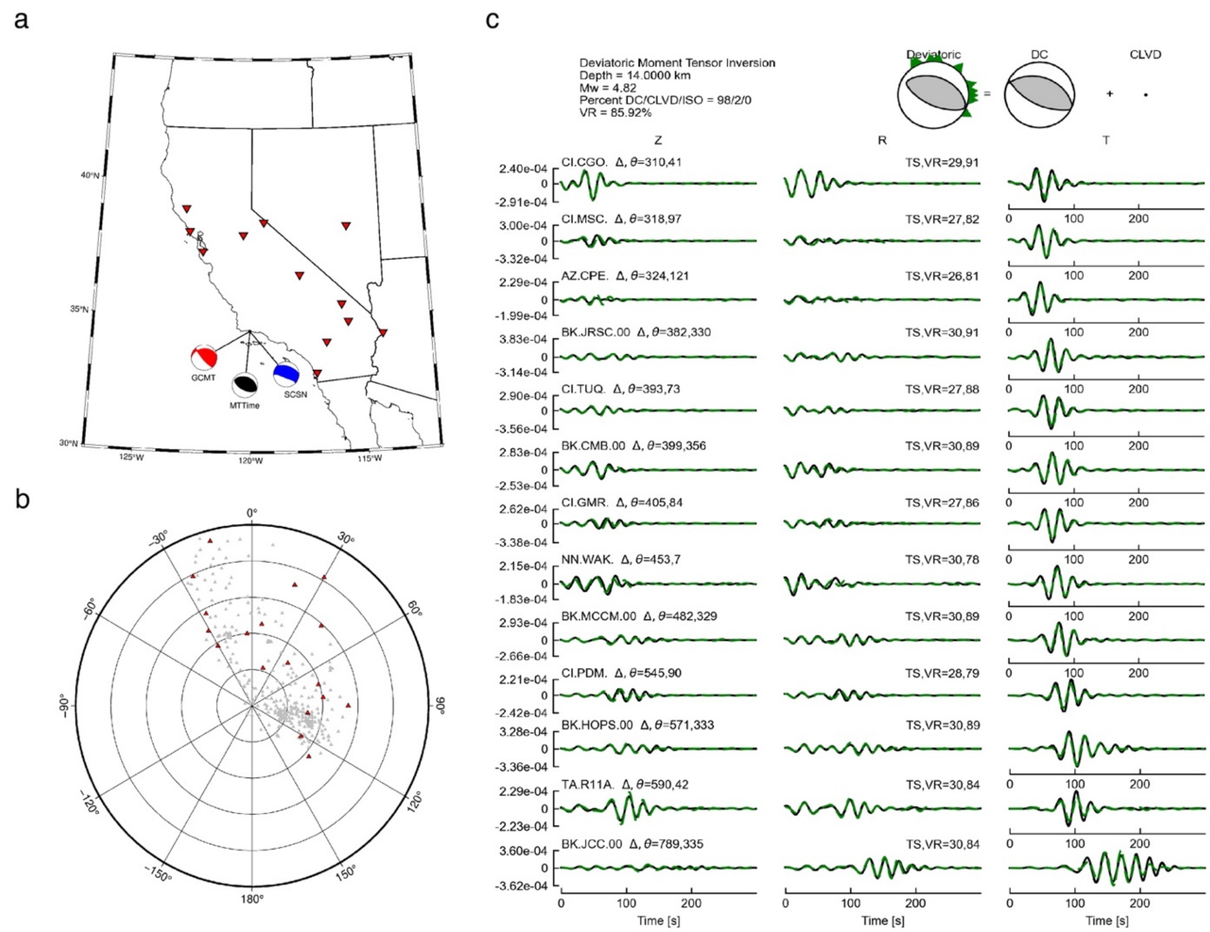

Figure 2.2. Inverted solution for a Mw 4.8 event off the coast of Santa Barbara, CA that occurred on 29 May 2013. Panel a shows the GCMT (red beachball), ANSS (blue beachball), and this study's (black beachball) moment tensor solutions for the event; the red inverted triangles show the location of the stations used in the inversion. Panel b shows all available stations by distance and azimuth from the source; the red triangles are the stations with the highest signal-to-noise ratio (SNR) in the given bins. Stations closer than 200km from the source are not used in the inversion. Panel c shows the waveform fits for the inverted solution (green) compared to the observed waveforms (black). Summary information on the moment tensor is shown to the left of the beachball diagram. Stations are sorted by distance; the distance and azimuth from the event are listed above the vertical component waveforms. The time shift (TS) and variance reduction (VR) for each station are shown above the radial component waveforms.

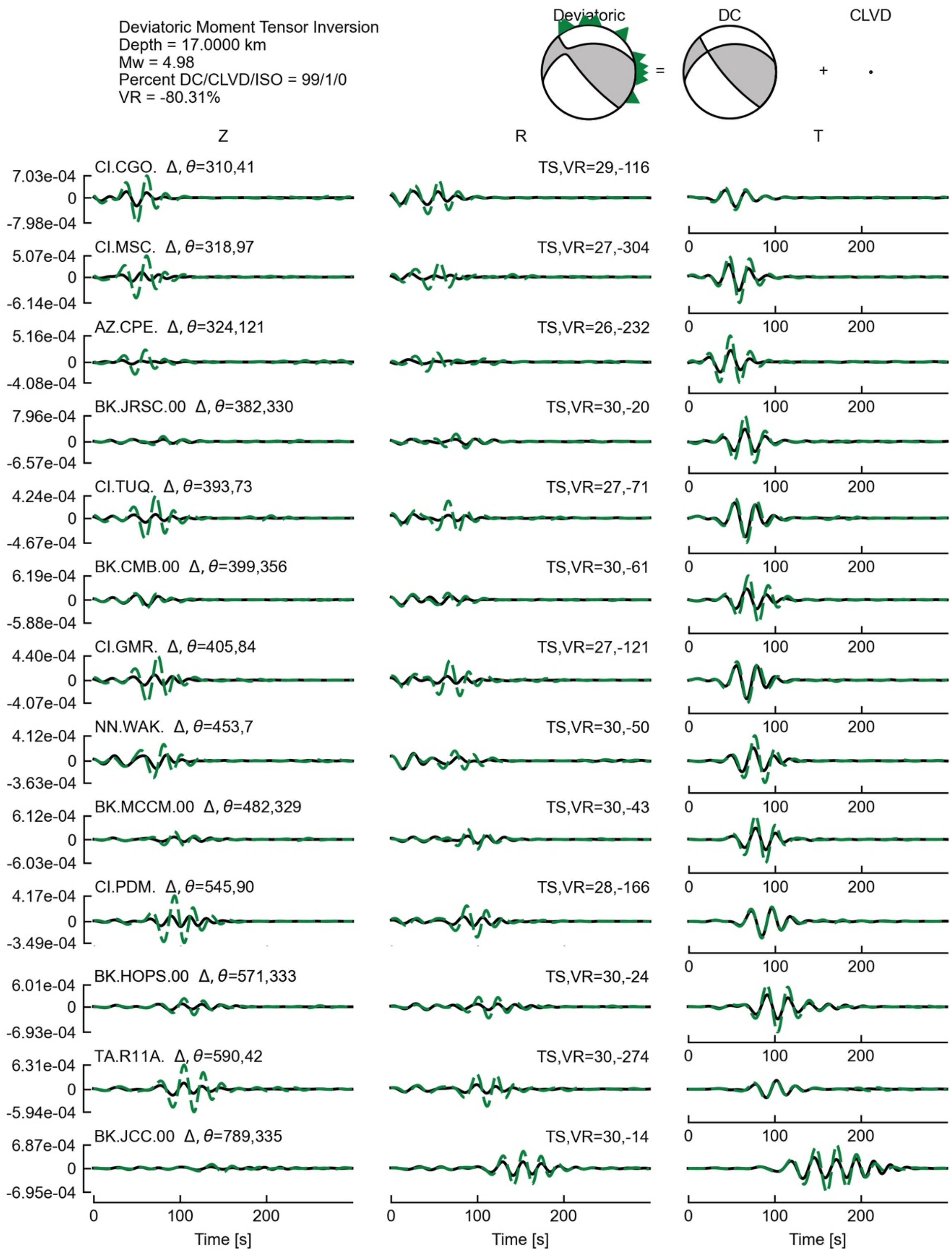

Figure 2.3. Waveform fits for the 2013 Santa Barbara event using the GCMT solution parameters. The stations and time shifts are the same as those used in the inverted solution. Note the difference in amplitude between the inverted solution (Figure 2.2c) and the GCMT solutions in this figure.

The GCMT solution has a moment magnitude of 4.94 and hypocenter depth of 17km. The GCMT mechanism for this event is mostly reverse with a small amount of obliquity (Figure 2.2a). The solution has a DC% of 99%; however, the GCMT solution struggles to fit the waveform amplitudes in the vertical and transverse components across all stations (Figure 2.3), resulting in an overall variance reduction of -80.31%. The solution from the Southern California Seismic Network (SCSN) more closely resembles the result of this study. The SCSN mechanism (Figure 2.2a) is also purely reverse, though with a 47% CLVD component. The moment tensor depth for the SCSN solution is also at 14km. The SCSN magnitude is 0.02 smaller than the MTTime solution, which is a negligible difference. When forward modelled onto the stations used to invert our solution, the SCSN solution has a variance reduction of 73% at 14km depth (moment tensor preferred depth). The strike, dip, and rake of both fault planes are also within $\pm 3^{\circ}$ of the MTTime solution, which indicates that the local solution and the inverted solution prefer the same fault orientations, unlike the GCMT fault planes.

In comparing different solutions for the Santa Barbara event, we show that the MTTime solution from this study provides similar fault plane orientations, magnitude, and depth to local catalogue solutions. The MTTime solution also has the largest variance reduction of the three moment tensors, performing particularly well at fitting distant stations.

From the example of the 2013 Santa Barbara earthquake, we show that the MTTime solutions match well with the local moment tensor solution from the SCSN. The MTTime solution outperforms both the GCMT and SCSN solutions in terms of waveform fit, particularly at the most distant stations. Using 3D Green's functions has been shown to improve fits at distant stations (>200 km from the source) compared to 1D Green's functions (Chiang et al., 2022) since they are able to capture lateral heterogeneities along the ray path. Therefore, using 3D Green's functions expands the ability to compute accurate moment tensors in regions where local station coverage is sparse.

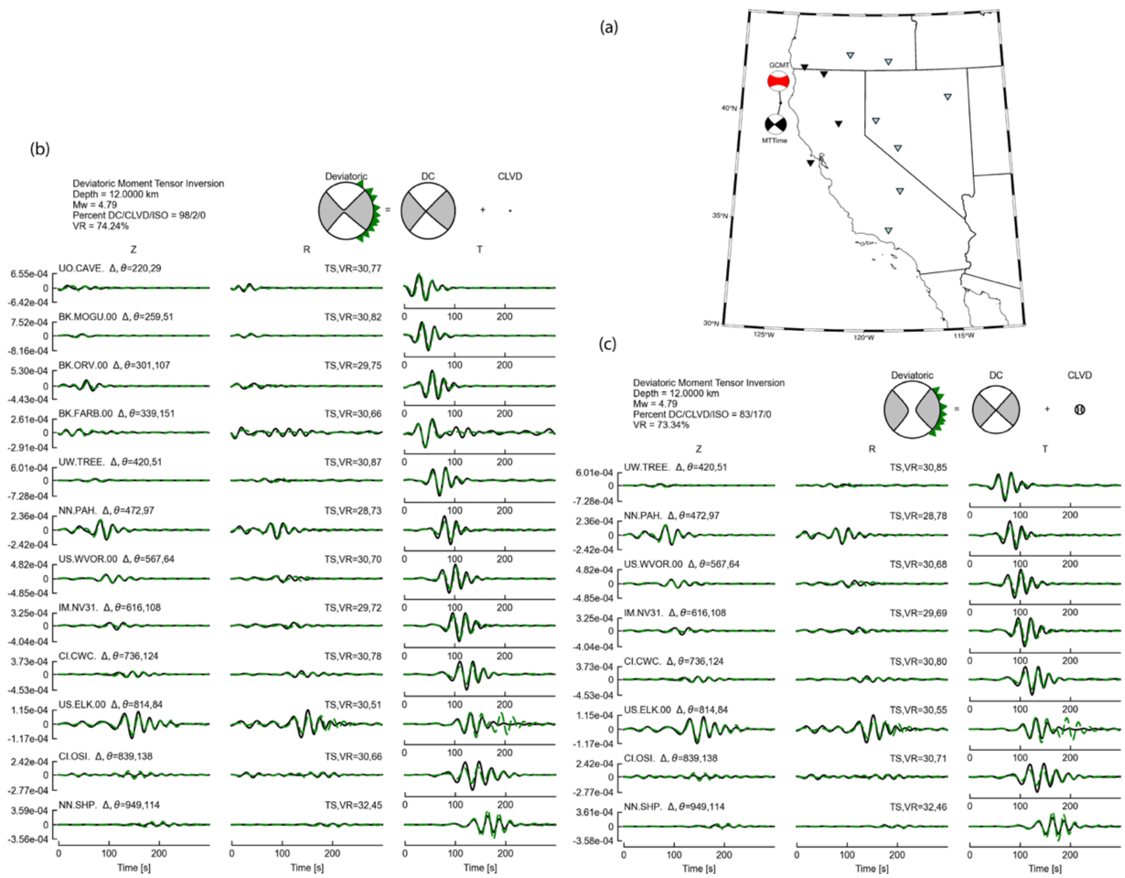

Figure 2.4. Inversion results for an off-shore Mendocino earthquake from 22 March 2020. Panel a shows the location of the earthquake and the stations used in the inversion; the GCMT solution (red beachball) is shown next to the MTTime solution (black beachball) for comparison. Stations less than 400km from the source are plotted in black, while stations greater than 400km are plotted in blue. Panel b shows the inverted solution using all 12 stations; panel c shows the inverted solution when only using stations >400km from the source.

To test the effect of sparse coverage on the inversion results, we computed two moment tensors for a Mw 4.8 earthquake that occurred off-shore on the Mendocino Fracture Zone on 22 March 2020. This event is on the western-most edge of CANVAS and occurs nearly 50km from the coast. The GCMT solution (red beachball, Figure 2.4a) has a magnitude of Mw 4.92 and depth of 25km. Though the strike, dip, and rake of the GCMT solution is within 5˚ of the inverted solution, the GCMT has a 34% double-couple component. The full MTTime solution (black beachball, Figure 2.4a; Figure 2.4b), on the other hand, has 98% double couple, with a depth of 12km and magnitude of Mw 4.79. These values match the NCEDC solution, which is calculated using stations that are within 250km of the source.

We tested the robustness of the 3D Green's functions by recalculating the moment tensor for this event using only stations that are greater than 400km from the source (Figure 2.4c). Using distant stations decreases the number of stations used in the inversion by one-third (Figure 2.4a); however, only using distant stations does not affect the moment tensor result significantly. At 12km depth, the distant station solution has the same magnitude as the original solution and a variance reduction that is less than 1% lower than the original solution. The biggest change to the distant solution is in the double couple percentage. The original solution had a 98% DC, meaning that the moment release is nearly purely tectonic. When using only distant stations, the DC percentage lowers to 83%. Though the DC percentage is 15% lower, both the full solution and distant solution have high DC percentages, making the drop in DC percentage negligible for interpreting the moment tensors. The distant station solution has a 100% DC component at 14km depth with a magnitude of M_W 4.8. Detailed uncertainty analysis could provide insight into which solution best fits the data (e.g., using MTUQ, Silwal and Tape, 2016), but we defer uncertainty analysis to a later study.

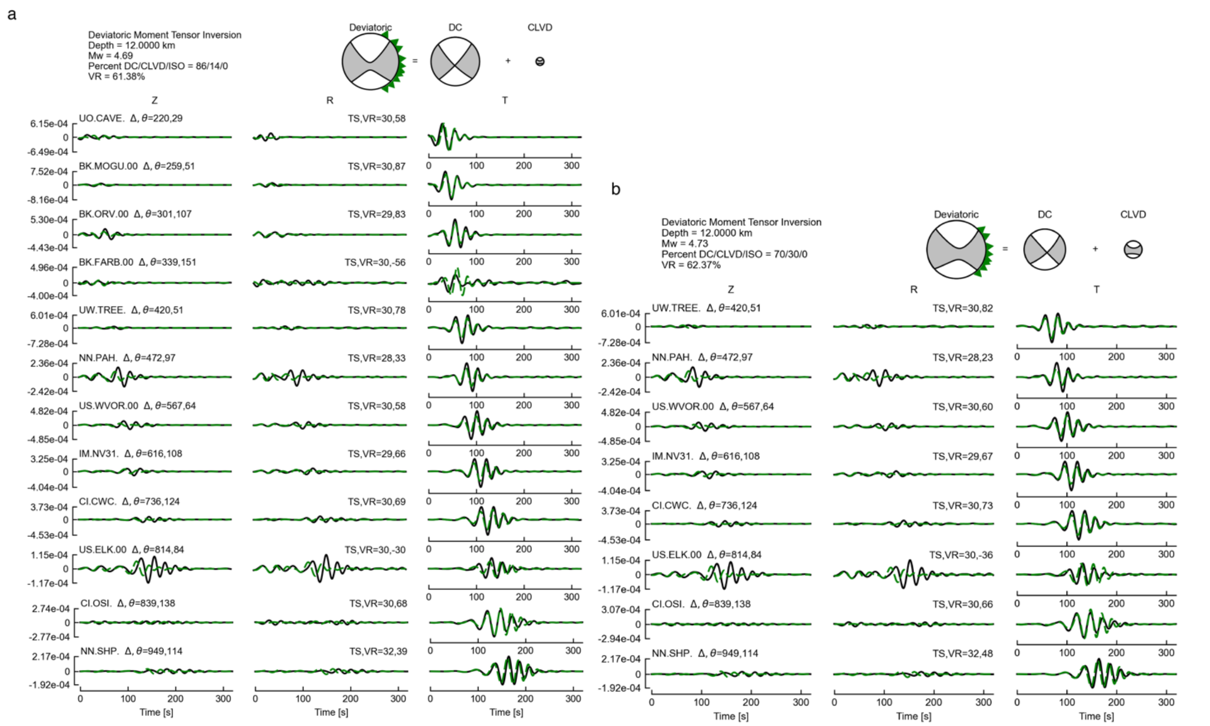

Figure 2.5. Solutions for the 22 March 2020 calculated using 1D Green's functions. Panel a shows the 1D solution with all available stations (Figure 2.4a); Panel b shows the 1D solution using only stations that are further than 400km from the epicenter (blue triangles, Figure 2.4a). The time shifts used are the same time shifts used for the 3D solutions.

We also tested the performance of 1D Green's functions for the same Mendocino event (Figure 2.5). We calculated 1D Green's functions using the frequency-wavenumber integration approach; we used the Computer Programs in Seismology (Herrmann, 2013) for the wave propagation solver. This methodology is used by both the NCEDC and SCEDC to calculate moment tensors for both catalogues (Dreger et al., 1998; Hutton et al., 2006). We used Gil7 (Dreger and Romanowicz, 1994) as velocity model used to calculate Green's functions. To test the robustness of the 1D Green's functions, we computed 1D solutions using all stations used in the 3D moment tensor inversion (all triangles, Figure 2.4a) as well as using only stations greater than 400 km from the epicenter (blue triangles, Figure 2.4a). We held the depths of the solutions fixed at 12km, which is the preferred depth of the 3D solutions; we also imposed the same time shifts on each station as were used in the 3D solutions.

The 1D solution using all stations has a lower magnitude than the 3D solution, dropping to M_W 4.69, with an overall variance reduction of 61.38%. The fault planes have a similar orientation to the 3D solution, though the dip values are slightly shallower in the 1D solutions (75˚ for 1D vs.

85˚ for 3D). The double-couple percentage is 86%, which is similar to the 3D double-couple percentage of 98%. Though most stations show similar variance reductions, 3 stations that are well-fit with the 3D solution are poorly fit in 1D (BK.FARB, NN.PAH, and US.ELK). The path from the epicenter to BK.FARB (Farallon Islands) travels off-shore; since Gil7 has a Moho depth of 25km, which is much deeper than to be expected off-shore, this could explain the poor fit at BK.FARB. NN.PAH (Pah Rah Ranges, Nevada) and US.ELK (Elko, Nevada) are both east-northeast of the epicenter, and travel through the Klamath Mountains, the northernmost Central Valley, the Sierra Nevada, and the Basin and Range province for US.ELK (see Chapter 3 for locations and descriptions of the listed terranes). The alternating fast and slow velocities along each path are difficult to capture with a 1D model, causing the degradation in fit.

The 1D solution using the distant stations increased the magnitude of the event by 0.4 to M_W 4.73 and increased the variance reduction to 62.37% due to the removal of BK.FARB. The double-couple percentage drops to 70%. The strike of the fault planes are still consistent with the 3D and 1D solution using all stations, but the dip angles change significantly. While the 1D solution had dip angles around 75˚ for both fault planes, the 1D solution using distant stations has a steep dip angle of 87˚ on one fault plane, and a shallower dip angle of 70˚ on the second fault plane. The trend is waveform fits is the same as in the solution with all stations included, though the variance reduction at each station is higher for the stations that fit well, and lower for the NN.PAH and US.ELK compared to the 1D solution with all stations included.

Overall, we show that the MTTime solutions presented in the two case studies have better waveform fits than the GCMT solutions, and more closely resemble local catalogue solutions in magnitude, depth, and fault plane orientation. This indicates that resolving lateral heterogeneity in Green's functions provides more consistent mechanisms and better waveform fits than using 1D Green's functions. The performance of 1D Green's functions is highly dependent on the source-receiver path (see also Chiang et al., 2022). We also show that calculating 3D Green's Functions improves the accuracy of waveform fits at distant stations from the source. The accuracy of the solution is not degraded by only using distant stations, which has broad implications for improved moment tensor solutions for offshore events or events where local stations are non-existent or inaccessible.

2.4.2 Comparison with GCMT solutions

The case studies discussed in the previous section highlight the power of using 3D Green's functions to calculate moment tensors in both the ability to resolve moment tensor solutions that are on par with local catalogue solutions and the ability to fit waveforms at great distance from the source. To better understand the power of 3D Green's functions on a broad scale, we compared the solutions from this study to the GCMT solutions that serve as the focal mechanisms for CANVAS (Figure 2.6).

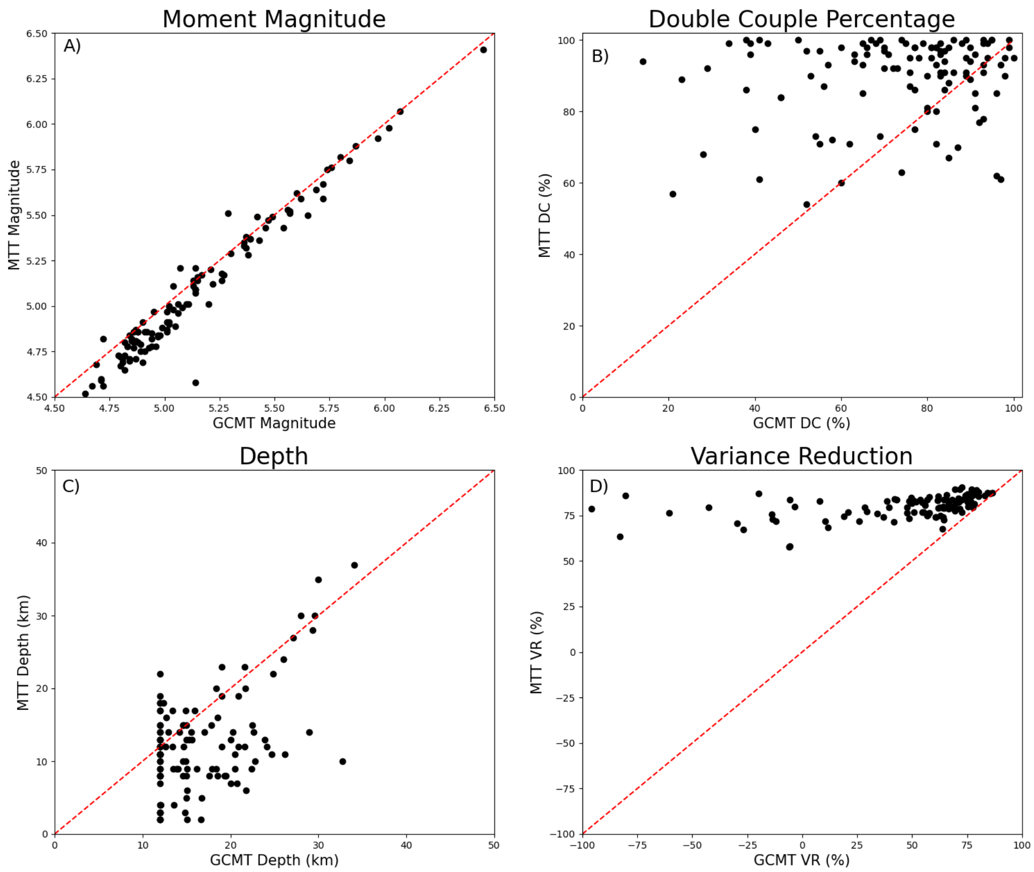

Figure 2.6. Summary Statistics of the 115 inverted events comparing values from the GCMT and this study. We compare magnitude (Panel a), double couple percentage (Panel b), preferred depth (Panel c), and the variance reduction of both solutions modelled on the same dataset. GCMT values are plotted on the x-axis for all panels, and the results of this study are plotted on the y-axis. The red dashed line represents the one-to-one line of the two values.

Figure 2.6 shows the comparison between the GCMT solutions and the MTTime solutions in magnitude, depth, double couple percentage, and variance reduction. Magnitude, depth, and double couple percentage values are taken from the GCMT catalogue (globalcmt.org; Ekström et al., 2012). In order to create a fair comparison of the solutions for variance reduction values, the GCMT solutions are used to forward model waveform fits using the 3D Green's functions calculated for this study. The stations and time shifts used in the inverted solution are kept constant.

For magnitude values, the MTTime and GCMT solutions are similar at the top end of the magnitude range used in this study (Mw>5.75). However, MTTime has consistently lower magnitude values below Mw 5.75, especially at the lowest magnitudes (Mw<4.75). Other studies have shown that the GCMT magnitude tends to be overestimated for crustal continental events (Hjörleifsdótir and Ekström, 2010; Sawade et al., 2022), which could explain the discrepancy with the MTTime magnitudes. The MTTime magnitudes more closely match local catalogue magnitudes (Figure 2.7c), which supports the theory that GCMT magnitudes are overestimated. Another possible cause of the magnitude discrepancy is in the attenuation model used to calculate CANVAS. CANVAS uses PREM's attenuation model (Dziewonski and Anderson, 1981), which has known inadequacies (Romanowicz and Durek, 2000). The attenuation model chosen could affect the amplitude of the synthetics used in the inversion, which in turn affect the moment estimation. Therefore, testing different attenuation models (e.g.,QL6; Durek and Ekström, 1996) could confirm or rule out its contribution to lowered magnitudes for the MTTime solutions; QL6 is also used as the attenuation model in GCMT workflow, so using QL6 would provide a more fair comparison of the MTTime solutions with the GCMT solutions.

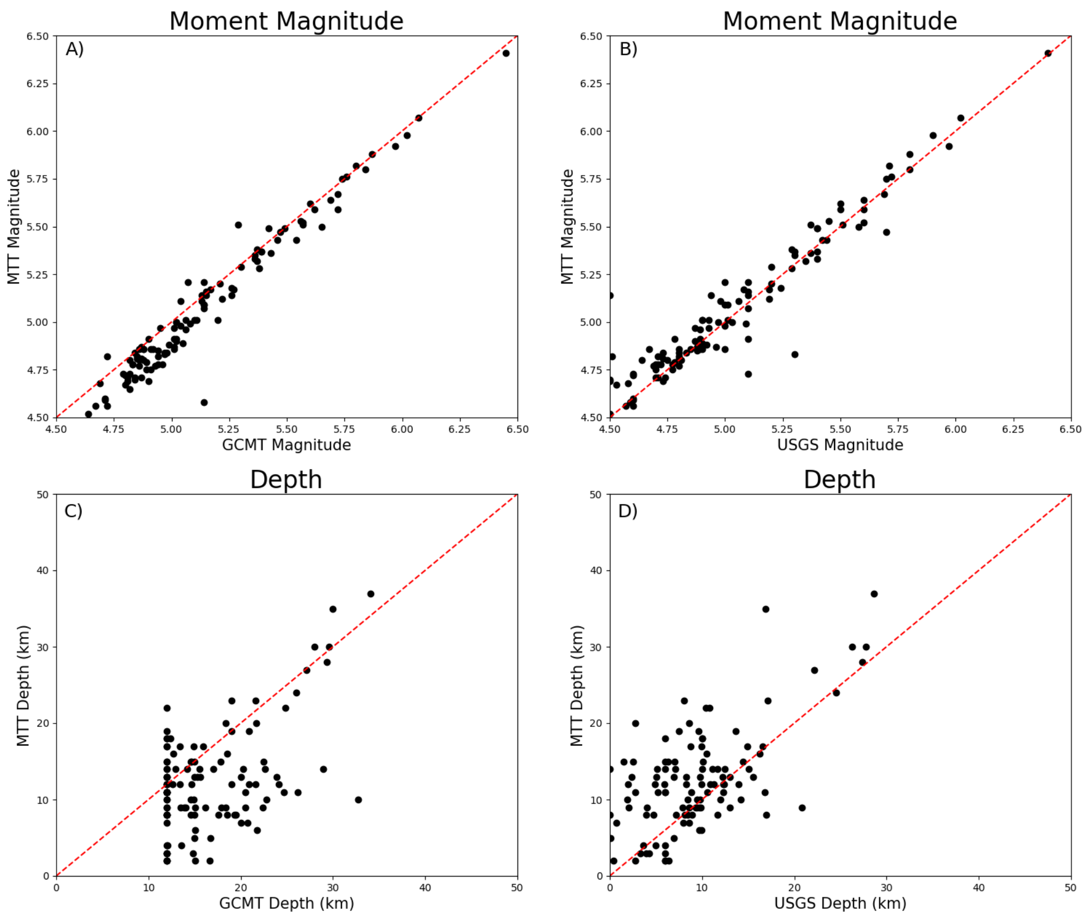

Figure 2.7. Summary statistics for the inverted solutions compared to the GCMT (left column) and USGS (right column) solutions. Inverted values are plotted on the y-axis, where as GCMT/USGS values are plotted on the x-axis. The top row compares moment magnitude values, while the bottom row compares depth of event. The red dotted line in each panel represents the one-to-one line. Values above the line mean that the inverted solutions are larger magnitude/deeper, while values below the line mean that the GCMT/USGS solutions are larger magnitude/deeper.

As for the depth of our solutions, the MTTime solutions are an average of 4.4km shallower than the GCMT solution (Figure 2.6b). This can mainly be explained by the fact that the GCMT has a minimum depth requirement of 12km; most of the earthquakes in this study occur at depths shallower than 12km. However, events that occur deeper than 12 km depth still have shallower preferred MTTime depths than the GCMT solutions. Compared to the USGS solutions, the MTTime solutions are on average 3.3km deeper than the USGS (Figure 2.7d). Hypocentral depth is generally a poorly-constrained earthquake source parameter for shallow events (Craig, 2019;

Florez and Prieto, 2017; Tsai and Aki, 1969), particularly when 3D heterogeneity is not taken into account (Richards-Dinger and Shearer, 2000). Since the USGS hypocentral depths calculated by the National Earthquake Information Center (NEIC) are calculated using 1D travel-time differences of pP-P waves at teleseismic stations, the discrepancy in depth is likely related to methodological differences.

The final parameter we varied in calculating the MTTime sources was the double couple percentage (DC %). The DC % for the MTTime solutions were on average 16% higher than the DC % of the GCMT solutions (Figure 2.6c). On the surface, this indicates that the MTTime solutions have a larger tectonic component, which is to be expected for the events of this study. However, there are a few important caveats to interpreting the DC % results. We preferentially choose solutions that have high DC % under the assumption that tectonic events should have high DC %. This assumption does not hold everywhere, however. For example, moment tensors in the Geysers Geothermal field in northern California tend to have higher CLVD components due to fluid injection (e.g., Boyd et al., 2018). Events in the Walker Lane region of eastern California also have higher CLVD components (Dreger et al., 2000; Panning et al., 2001; Shuler et al., 2013), which could be linked to volcanic processes in Long Valley (e.g., Dreger et al., 2000; Minson and Dreger, 2008). Though we attempt to take these anomalous regions into account, we ultimately will choose a solution with a higher DC % if the waveform fits prefer higher DC %. Uncertainty analysis could provide clarity on whether sources with higher CLVD would also be possible, so we refrain from analyzing DC/CLVD % for a future study.

To determine how well the solutions fit the data, we analyzed the waveform fits of the MTTime and GCMT solutions using the overall variance reduction. Variance reduction is a simple misfit function that measures the goodness of fit of a synthetic and observed seismogram where:

$$Variance\ Reduction\ = 100 * \left(1 - \sum_{i=0}^{n} \left(\frac{synthetic_i - observed_i}{observed_i}\right)^2\right) \qquad (1)$$

where *n* is the total number of points in the seismogram and the *synthetic* and *observed* values are the displacement values at point *i* in the seismogram. Variance reduction is highly sensitive to both phase and amplitude, making it a good indicator of waveform fit. Variance reduction is expressed as a percentage, and its values range from -∞% to 100%, where 100% indicates a perfect match between the observed and synthetic data.

The MTTime solutions have a 54% higher variance reduction than the GCMT solutions, meaning that MTTime solutions consistently fit the data better than the GCMT solutions (Figure 2.6d). A majority of the MTTime solutions show a minor (<25%) increase in variance reduction, while nearly 20% of events in the MTTime catalog have at least a 50% increase in the variance reduction compared to the GCMT solution. A small number of events have significantly different mechanisms than the GCMT solutions (e.g., the 2013 Santa Barbara event in Section 3.1); the source provided by the GCMT is not able to fit the data in amplitude, and so variance reduction values are below zero. The second factor that can cause the GCMT solutions to have low variance reduction values is discrepancies in depth. Sources that are far deeper than expected tend to poorly fit the data, so the shallower MTTime solutions have higher variance reductions even if the mechanism is similar.

2.5 Conclusions

The moment tensor solutions presented in this study fit waveform data better, have magnitudes similar to local catalogue solutions, resolve depth discrepancies present in the GCMT solutions, and produce solutions with higher double couple percentages than the GCMT catalog. By taking 3D heterogeneity fully into account, we can exploit data from stations up to 1200km from the source and have shown that we can get nearly identical solutions when only using distant stations. The ability to use distant stations to create accurate moment tensor solutions has broad implications for better source constraints on events where there are no local networks available, such as for off-shore events or explosion monitoring.

The largest barrier to the use of 3D Green's Functions is their computational cost. 3D Green's functions require supercomputing power to compute and take an order of magnitude longer to calculate than a 1D Green's Function for the same path. Therefore, calculating 3D Green's Functions on the fly is not suitable for rapid response moment tensor solutions. One possible solution is to institute 3D path corrections using the 3D model at long wavelengths, which allow for faster computational times by approximating the effect of 3D structure (e.g., Romanowicz, 1982). However, this barrier could be overcome through creating a reciprocal 3D Green's Function catalog. A reciprocal catalogue would calculate Green's tensors for arbitrary source-receiver pairs throughout a domain. These pre-computed Green's functions can then be used to rapidly model synthetic seismograms for a source and receiver in similar locations to the ones used to create the Green's Function. By eliminating the need to calculate 3D Green's Functions on the fly, the benefits of 3D Green's Functions are accessible to real-time applications. We hope to further this study by creating a reciprocal Green's Function catalogue for California and Nevada. Though the period band of the current model limits us to Mw>4.5, we plan to continue iterating CANVAS such that we can resolve periods down to 10 seconds, which would allow us to compute moment tensors for events down to Mw 3.5.

2.6 Acknowledgements

Simulations were run on the Lassen GPU-accelerated platform operated by Livermore Computing. This work was supported in part by Lawrence Livermore National Laboratory Directed Research and Development project 20-ERD-008. This work was performed under the auspices of the U.S. Department of Energy by Lawrence Livermore National Laboratory under Contract DE-AC52-07NA27344. C. Doody is also supported under SCEC Award #22130. We thank the associate editor and two anonymous reviewers for their helpful comments.

Chapter 3

CANVAS: An adjoint waveform tomography model of California and Nevada

3.1 Abstract
We present California-Nevada Adjoint Simulations (CANVAS), an adjoint waveform tomography model of the crust and uppermost mantle iterated to a minimum period of 12 seconds. CANVAS is iterated in two distinct stages: the first stage with source mechanisms from the GCMT, and the second stage with the source mechanisms calculated in Chapter 2. We show that updating the source mechanisms significantly improves waveform fits and azimuthal coverage of windowed data used to calculate the gradients. As for the model itself, we improved waveform fits over our starting model, WUS256 (Rodgers et al., 2022), particularly in the dispersed surface waves. CANVAS resolves tectonic features seen in other models and is able to accurately define the depth to basement of major basins, including the Central Valley and the Ventura Basin. We hope that CANVAS can serve as a starting model for iterating to shorter periods over the state, or for crustal tomography models on smaller scales.

3.2 Introduction
Sitting at the junction of the Pacific plate and North American plate, California and Nevada encompass a complex tectonic setting that includes the subduction of the Gorda Plate in northwestern California (e.g., Stoddard, 1987; Wilson, 1989), the right-lateral transform boundary of the San Andreas fault (e.g., Anderson, 1971; Lawson, 1908; Powell and Weldon, 1992), and the Basin and Range province, an extensional regime that covers a large swath of the American southwest (e.g., Nolan, 1943). The active deformation over the plate boundary creates a significant seismic hazard across most of California and western Nevada (Hatem et al., 2023). Understanding the seismic risk to the populations of California and Nevada requires accurate seismic velocity modelling; accurate velocity modelling provides more accurate estimations of shaking during large earthquakes (Rodgers et al., 2020). Accurate velocity models are also necessary for calculating stress variation using moment tensors (Cheng et al., 2023), which is also vital for understanding seismic hazard.

Over the past 30 years, many seismic tomography models of California, whether of the whole state or of a sub-region of it, have been proposed (e.g., Chen et al., 2007; Lin et al., 2010; Pollitz, 1999; Shaw et al., 2015; Stanciu and Humphreys, 2021; Suess and Shaw, 2003; Tape et al., 2009; Thurber et al., 2009; Wang et al., 2022). Models that include the whole state (Lin et al., 2010; Stanciu and Humphreys, 2021) have been derived using ambient noise tomography (Lin et al., 2010) and travel-time tomography (Stanciu and Humphreys, 2021). Here, we present a model of California and Nevada computed using adjoint waveform tomography (AWT). AWT has multiple advantages over previous approaches. Travel-time tomography is a ray-based approach that is computationally efficient for computing mantle structure, but does not consider 3D wavefield effects, causing it to perform more poorly in tectonically complex regions (Liu and Gu, 2012; Rickers et al., 2012; Tarantola, 1984). Ambient noise tomography, on the other hand, excels at resolving small-scale geologic features at shallow depths (e.g., Barak et al., 2015; Bowden et al., 2016; Lin et al., 2013; Lin et al., 2014), but the models struggle to fit waveform data (Rodgers et al., 2022). AWT solves the 3D elastic wave equation to generate synthetic seismograms (Afanasiev et al., 2019; Komatitsch and Tromp, 2002a, b); the synthetics are then compared to the observed seismograms, and the velocity model is iteratively updated to optimize the fit between the observed and synthetic data. AWT accounts for 3D wavefield effects such as wavefront healing and focusing/defocusing effects, which allows the model to capture tectonic complexity in detail. AWT requires significant computational cost on high-performance computing systems (Romanowicz, 2003; Thrastarson et al., 2022), which limits its accessibility.

Below, we present the California-Nevada Adjoint Simulations (CANVAS) model, a multi-scale adjoint waveform tomography model iterated to a minimum period of 12 seconds. The model resolves known tectonic features in the region; basins are also broadly visible without *a priori* input of basin structure. The main power of CANVAS is its waveform fits, particularly its ability to fit dispersed surface waves at distant stations. CANVAS's ability to accurately model waveforms suggest the model is useful for other seismological applications such as moment tensor inversion and as a starting model for smaller-scale regional full waveform inversion.

3.3 Data

Between 1 January 2000 and 31 October 2020, 123 events occurred in our domain of interest (bold black box, Figure 3.1) with moment magnitudes (M_W) between 4.5 and 6.5. The minimum magnitude threshold is chosen because smaller events have a low signal-to-noise ratio (SNR) at the longer periods used in early iterations of the model. The maximum magnitude threshold is chosen so that we can use the point-source approximation for the events; events larger than M_W 6.5 have source durations that overlap with the periods of interest and so can no longer be approximated as a point source.

Figure 3.1 shows the events used in different period bands of this study. We began with 103 events of the 123 available. The 21 events that were left out were removed during quality control because of noisy data when bandpass filtered to 30-100 seconds; events where less than 50% of stations had at least one window picked were considered 'poor' quality. Focal mechanisms for Stage 1 are taken from the Global Centroid Moment Tensor (GCMT) catalogue; using the model obtained at the end of Stage 1, we used `mttime` (Chiang, 2020) to invert for source parameters (see Chapter 2 for a detailed description of mttime). After recomputing source parameters, 8 events that did not pass initial quality control had enough windows picked to be added to the inversion dataset, bringing the total to 111 events. In the period band of 12-60 seconds, an additional 6 events passed quality control, totaling 117 events in the inversion dataset. Adding in 15 additional events increased path coverage in western Nevada and northernmost California (Figure 3.1). We used data from over 1300 seismic stations from over 40 permanent and temporary arrays throughout our domain; data was downloaded from the Federation of Digital Seismic Networks (FDSN) web services and stored in the Adaptable Seismic Data Format (ASDF; Krischer et al., 2016).

To test model performance on unused data, we also assembled a validation dataset. The validation dataset consists of 15 events that occurred between 1 November 2020 and 31 March 2022; these events have the same magnitude constraints as the inversion dataset. For a map of inversion dataset, please see Figure 1.1 of Chapter 1.

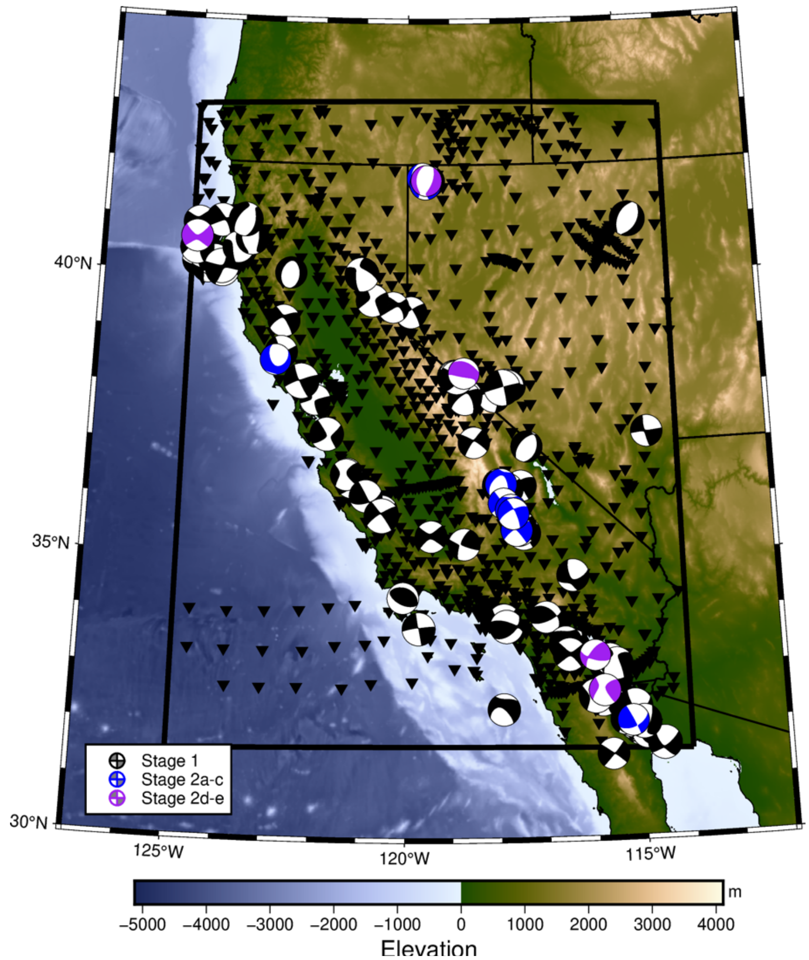

Figure 3.1. Event locations for the inversion dataset of CANVAS. Black beachballs denote the 103 events that were part of the original inversion dataset. Blue beachballs denote events that were added after inverting for source parameters at the end of Stage 1. Purple beachballs denote events that were added when the minimum period was reduced to 12 seconds (Stage 2d-e).

3.4 Methods

Adjoint waveform tomography (AWT) is both computationally- and data-intensive, requiring a workflow that can accommodate large amounts of data and manage large jobs on high-performance computing (HPC) machines. AWT workflow management software has become widely available in the past 10 years (Krischer et al., 2015; Modrak et al., 2018; Chow et al., 2020; Thrastarson et al., 2021), and is mostly based on Python (van Rossum and Drake, 2009). In this study, we used Salvus (www.mondaic.com), a full waveform inversion (FWI) workflow manager that handles all steps from data acquisition to inversions. Salvus has been used successfully to compute AWT models at regional scales (Doody et al., 2023; Gao et al., 2021; Rodgers et al., 2022; Wehner, Blom, et al., 2022; Wehner, Rawlinson, et al., 2022). The description below provides a broad overview of the methodology used; detailed information on the window picking algorithm can be found in Doody et al. (2023) and a thorough discussion of kernel conditioning can be found in Rodgers et al. (2022).

	Period Band	Source Catalogue	No. of Events	Source/Receiver Cutouts	ROI Max Depth	Minimum Velocity	No. of Iterations
Stage 1: GCMT Solutions							
a	30-100s	GCMT	103	75 km/35 km	50 km	2.4 km/s	24
b	25-100s	GCMT	103	75 km /35 km	15 km	2.4 km/s	22
c	20-80s	GCMT	103	35 km /0 km	0 km	2.4 km/s	26
Stage 2: Inverted Solutions							
a	20-80s	MTTime	111	35 km /0 km	0 km	2.4 km/s	25
b	15-60s	MTTime	111	35 km /0 km	0 km	2.4 km/s	17
c	15-60s	MTTime	111	35 km /0 km	0 km	2.0 km/s	23
d	12-60s	MTTime	117	35 km /0 km	0 km	1.5 km/s	9
e	12-60s	MTTime	117	35 km /0 km	0 km	1.0 km/s	15

Table 3.1. Inversion parameters for the 161 iterations of CANVAS.

To avoid getting trapped in a local minimum of the misfit surface, we took a deliberate, careful, multi-scale approach to constructing CANVAS. Table 3.1 lists the parameterization of the two main stages and 9 sub-stages of model iterations; it includes information on source parameters, events used, gradient treatments, and the number of iterations run at each sub-stage. The two main stages are divided based on the source parameters used. In Stage 1, focal mechanism solutions are taken from the Global Centroid Moment Tensor (GCMT) catalogue (Dziewonski et al., 1981; Ekström et al., 2012). We iterate over three period bands in Stage 1: 30-100 seconds (Stage 1a), 25-100 seconds (Stage 1b), and 20-80 seconds (Stage 1c). The maximum period was lowered in Stage 1c to improve the signal-to-noise ratio of the smaller events in the inversion dataset (M_W<5.0). Between Stage 1 and Stage 2, we inverted moment tensors for both the inversion and validation datasets using 3D Green's Functions calculated using the model at the end of Stage 1. We chose to invert for moment tensors to mitigate source errors that could affect waveform fits at short periods. The methodology used and the results of the moment tensor catalogue can be found in Chapter 2.

Once the new source parameters were computed, we replaced the GCMT source parameters with our inverted parameters and began Stage 2 (Table 3.1). Stage 2 is iterated in 3 successive period bands: 20-80 seconds (Stage 2a), 15-60 seconds (Stage 2b-c), and 12-60 seconds (Stage 2d-e). Beginning at Stage 2c, we began reducing the minimum allowed group velocity to accommodate slower wavespeeds in the uppermost crust. In the window picking stage, the details of which are discussed at length in Chapter 1, windows can only be picked in a given group velocity range. The maximum allowed group velocity was set to 8 km/s; the minimum group velocity, however, was iteratively lowered to accommodate crustal wavespeeds. In Stage 1 and Stages 2a and 2b, the minimum velocity is set to 2.4 km/s, which is far higher than the shear wave speeds in the uppermost crust (e.g., Fletcher and Erdem, 2017; Lin et al., 2010). We lowered the minimum velocity to 2.0 km/s at Stage 2c, 1.5 km/s at Stage 2d, and 1.0 km/s at Stage 2e. We inverted for the 5 radial anisotropy parameters V_{PV}, V_{PH}, V_{SV}, V_{SH}, and density throughout. Density is poorly constrained in the inversions due to its negligible effect on phase information; however, inverting for density is paramount for constraining velocities since ignoring density can result in poor recovery of wavespeeds (Blom et al., 2017; Płonka et al., 2016).

Forward simulations in Salvus are run using the spectral element method (Afanasiev et al., 2019). Once the synthetics were calculated, we picked windows based on a modified version of the window picking algorithm proposed in Krischer et al. (2015). The window picking algorithm was not restricted to picking only body waves or surface waves; we allowed windows to be picked from any part of the waveform. After window picking, we apply the station weighting algorithm from Ruan et al. (2019) to remove some geographic bias from our dataset. This algorithm downweighs the misfit values of stations that are geographically clustered and upweights stations where coverage is sparse. We used the time-frequency phase misfit function (Fichtner et al., 2008) to calculate the misfit between the observed and synthetic data. The time-frequency phase misfit function calculates misfit by transforming the data into the time-frequency domain (Kristekova et al., 2006; 2009), then calculates the weighted phase difference and envelope similarity between the observed and the synthetic data.

Once the misfit is calculated, we calculated sensitivity kernels for each event based on the interaction of the forward and adjoint wavefields. The event kernels are then summed together to create one gradient to be used for calculating the model update (Fichtner, 2010; Fichtner et al., 2006; Tape et al., 2007; Tarantola, 1988; Tromp et al., 2005). The gradient is then smoothed using anisotropic smoothing. The gradient is smoothed at 0.5 wavelengths laterally and 0.2 wavelengths vertically.

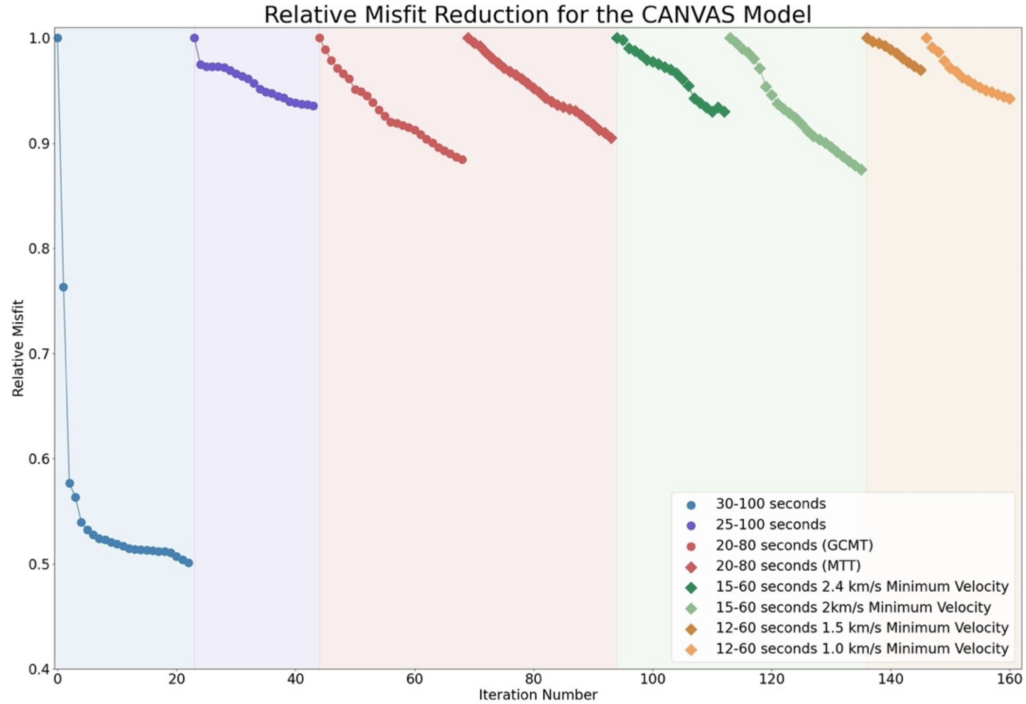

Figure 3.2. Relative time-frequency phase misfit function of CANVAS through 161 iterations. The shaded colors denote the period band: blue- 30-100 seconds, purple- 25-100 seconds, red- 20-80 seconds, green- 15-60 seconds, and orange- 12-60 seconds. Circular markers denote iterations where source mechanisms are taken from the GCMT (Ekström et al., 2012), while diamond markers denote iterations where we use the recomputed sources. At 15-60 seconds and 12-60 seconds, the iterations are broken down by the minimum velocity. See Table 3.1 for more information on the parameterization for each period band.

Since gradients are often inaccurate near the sources and receivers (Tromp et al., 2005), we set kernel values to zero in a spherical region of a given radius around the source and receiver locations; in Stage 1a (Table 3.1), source cut-outs had a radius of 75km and receiver cut-outs had a radius of 35km. At the beginning of Stage 1c, we removed the receiver cut-outs to begin updating the crust; at this point, we rely on the amount of data and crossing paths to eliminate any receiver artefacts. When we removed the receiver cut-outs, we also decreased the source cut-outs to 35km with the same reasoning as the receivers. In Stages 1a and 1b (Table 3.1), we also include a region of interest (Doody et al., 2023; Rodgers et al., 2022). The region of interest dampens updates above a given depth to avoid artefacts from the high-amplitude and highly heterogeneous shallow structure which cannot be constrained at longer periods. Instituting a region of interest allows us to constrain deep structure first before attempting to constrain crustal structure. In Stage 1a, we used a region of interest of 50km; it is reduced to 15km in Stage 1b, and then is removed completely beyond Stage 1c.

The model updates are computed using the trust-region Limited-memory Broyden-Fletcher-Goldfarb-Shanno (L-BFGS) algorithm, which is a quasi-Newton optimization algorithm (e.g., Conn et al., 2000; Nocedal and Wright, 2006). We followed the trust-region methodology of Boehm et al. (2018) which solves an auxiliary optimization problem that minimizes a quadratic approximation of the misfit surface near the current model. This approach is powerful in that the size of model updates are constrained by the ratio of the actual and predicted misfit values for a given model update. Good alignment between the predicted misfit from the quadratic approximation and the actual misfit allow us to make many model updates and be confident in our ability to not get trapped in local minima. Model updates are rejected when the total misfit across all events can no longer be reduced. When a model update is rejected, we reduced the trust-region radius to attempt to find a more modest model update that could reduce the overall misfit. If three consecutive model updates were rejected, we ended the sub-stage.

3.5 Results

Before discussing the model, we begin by examining the effect of source parameters on synthetics to illustrate the necessity of updating sources in adjoint tomography workflows. We break our analysis of CANVAS into two sections: waveform fit and tectonic structure. CANVAS is optimized to fit dispersed surface waves, so we focus our analysis on long paths to highlight CANVAS's ability to fit waveforms as they travel through diverse tectonic units. For tectonic structure, we show that CANVAS resolves major tectonic features observed in other tomography models; since the model is coarse compared to other crustal tomography models, we defer detailed tectonic analysis to a later study.

3.4.1 Effect of source catalogue on synthetics

As noted in the Methods section and discussed at length in Chapter 2, we inverted for source mechanisms at 20-80 seconds before iterating at shorter periods. The idea behind refining source mechanisms is to reduce errors in the source mechanisms and to improve waveform fits (Liu et al., 2004; Lei et al., 2020; Sawade et al., 2022). To illustrate the importance of inverting for source parameters, we looked at waveforms and window picking data for the M_W 4.8 Santa Barbara earthquake discussed in Chapter 2.

Figure 3.3 shows observed and synthetic data at the Berkeley Digital Seismic Network (BDSN; BDSN, 2014) station BK.JRSC. JRSC is located at the Jasper Ridge Biological Preserve in Stanford, California, which is about 400km from the source. Synthetics are calculated using the model at the end of Stage 1; the red waveforms use the GCMT source, while the green waveforms use the inverted sources. The observed waveforms show complexity in the vertical (top panel) and radial (middle panel) components. Both the GCMT and inverted solutions fit the body waves well in these components, though the GCMT solution shows a small time delay. In the surface waves, the GCMT synthetics have a negative time shift and significantly overestimate the amplitudes on all components. The GCMT synthetics also struggle to resolve the beginning of the Rayleigh wave in the radial component (~120-140 seconds after origin time; middle panel). Compared to the GCMT synthetics, the inverted synthetics show smaller time shifts in the vertical component and amplitudes that are closer to the observed data. The inverted synthetics are also better able to capture the entire surface wave packet in all three components. The impact of the change in source parameters is largest in the transverse component. The GCMT synthetics show a small negative time shift and has twice the amplitude of the observed data. Though the inverted solution synthetics have a small negative time shift in the later part of the Love wave, it is able to accurately capture the amplitudes in the observed data.

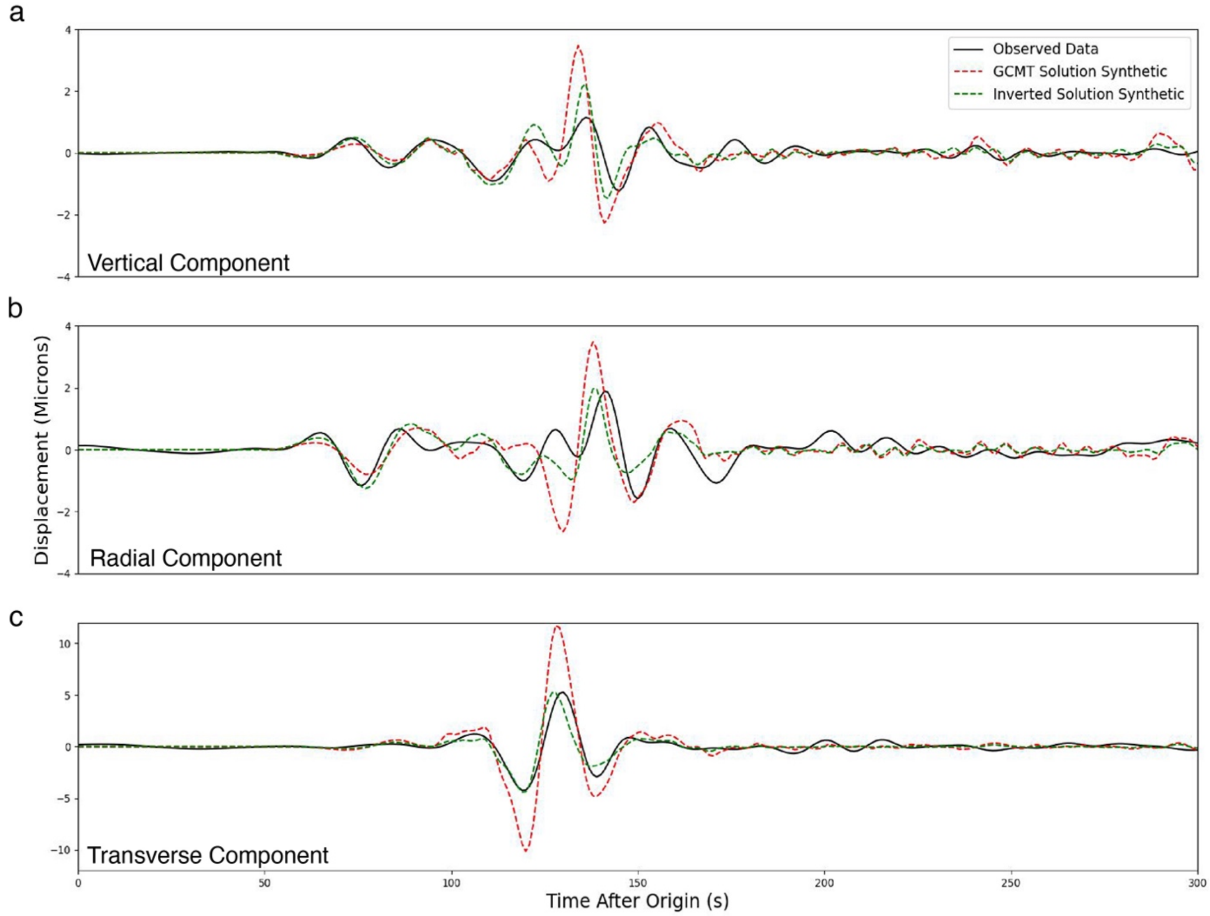

Figure 3.3. Waveform comparison of synthetics with different source parameters at station BK.JRSC for a magnitude 4.8 event off the coast of Santa Barbara (29 May 2013). The red waveforms have source parameters from the GCMT; the green waveforms use the inverted source parameters from chapter 3. The black waveforms are the observed data. The top panel shows the vertical component, the middle the radial component, and the bottom the transverse component. Waveforms are bandpass filtered to 20-80 seconds.

The data from BK.JRSC show the impact of source parameters on a single source-receiver pair; to understand the impact over all source-receiver pairs for this event, we compared the windows picked for the GCMT synthetics and the inverted synthetics (Figure 3.4). Figure 3.4 shows the aggregate windows picked for the GCMT synthetics (Figure 3.4a) and the inverted synthetics (Figure 3.4b). Each line represents a window at a given station; the color indicates which component(s) contributed windows and the length of the line denotes the length of the window.

The GCMT synthetics pick windows at 150 stations of the 364 stations available, for a total of 303 windows (~2 windows per station); the total window length amounts to just over 5 hours. The azimuthal distribution (rosette plot, Figure 3.4a) is heavily skewed to the northeast; stations to the east and east-southeast of the earthquake contribute less than 20% of the windows, with most stations at these azimuths only contributing windows in the north component (orange bin at 100-100˚ azimuth). By contrast, the inverted synthetics have 175 stations contributing windows, raising it above the quality control threshold of 50% of available stations contributing windows. The aggregate window length increases by 1.5 hours, and 94 windows are added. Most of these windows are added in stations to the east of the event where the GCMT synthetics struggle to capture windows (rosette plot, Figure 3.4b). This azimuth (100-110˚) falls along the nodal plane of the inverted event's source mechanism; because the GCMT solution has significantly different nodal planes from those of the inverted solution, this can explain the GCMT synthetics' difficulty in constraining waveforms to the east of the event.

The difference in the synthetics between the model with the GCMT source parameters and the model with the inverted parameters showcase the importance of inverting for source parameters to improve synthetic waveforms in FWI workflows. Inverting sources with updated versions of the model creates a positive feedback loop of improving synthetics to improve the model, then the improved model improves the synthetics to provide more accurate moment tensor solutions. For about half of solutions, the difference between the GCMT and inverted solutions are relatively small, which means that the difference in synthetics is minimal. However, for the events where there are large discrepancies between the sources, inverting for source mechanisms can increase the number of usable stations and events for the inversion, the amount and aggregate time of windows chosen, and the ray path coverage throughout the domain.

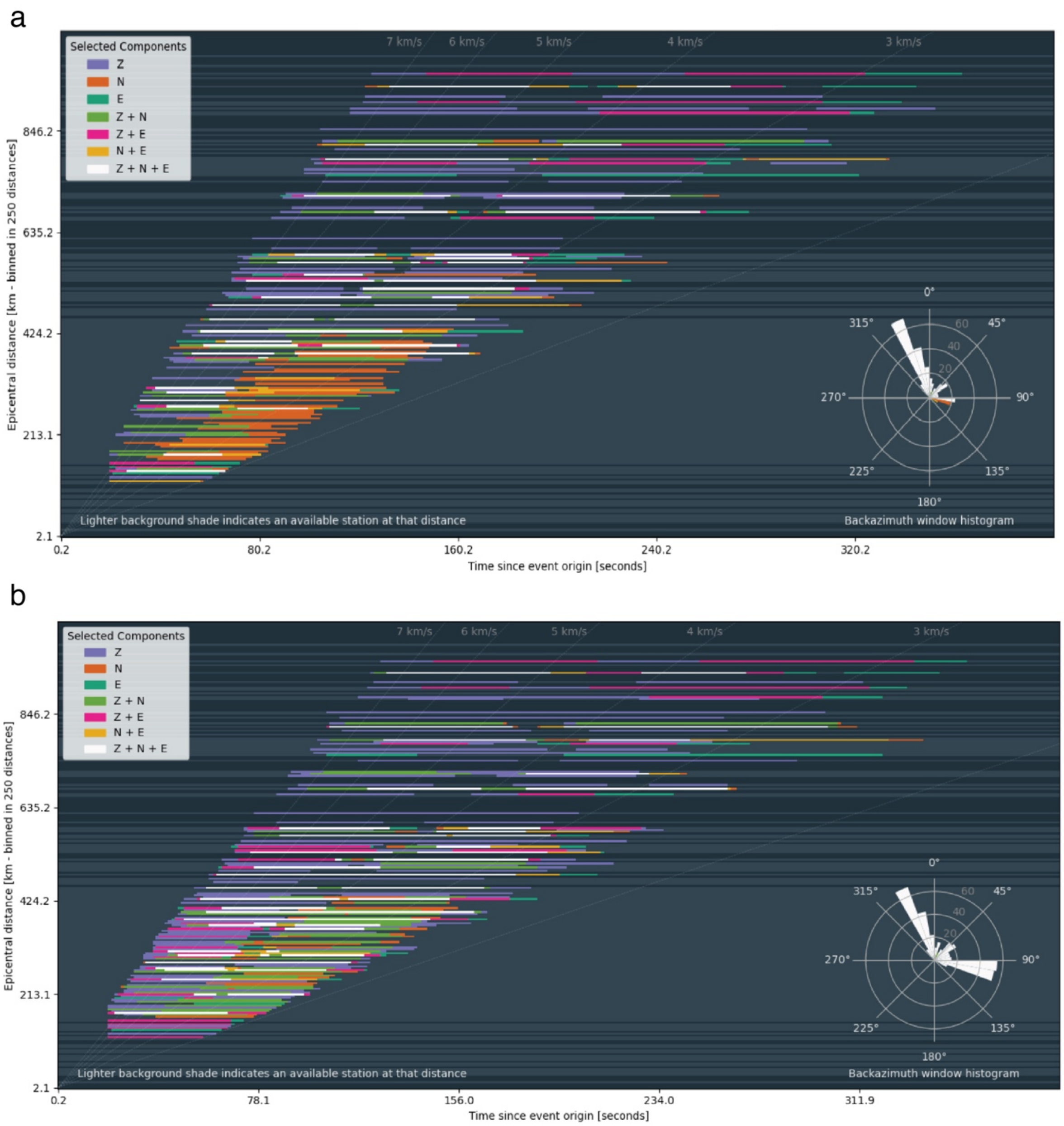

Figure 3.4. Aggregate window statistics for a M_w 4.8 event off the coast of Santa Barbara that is included in the inversion dataset. Panel a shows windows picked for synthetics where source parameters are taken from the GCMT; panel b shows the windows picked for synthetics that use the inverted sources from Chapter 2 for source parameters. Each gray line represents a station with data, where stations are sorted by distance from the source. Colored lines show windows picked from the available data; the colors denote what component(s) windows were picked in (see legend). The length of the line denotes the length of the window. Rosette plots in the bottom right-hand side of each panel denote the number of stations with windows binned by azimuths.

3.4.2 Waveform Fits

To illustrate CANVAS's ability to fit waveforms, we show waveform comparisons with WUS256 for four events. Three events are taken from the inversion dataset, and one event is from the validation dataset. We chose events that occur in a variety of locations within our model domain and focus on long paths that sample diverse tectonic settings.

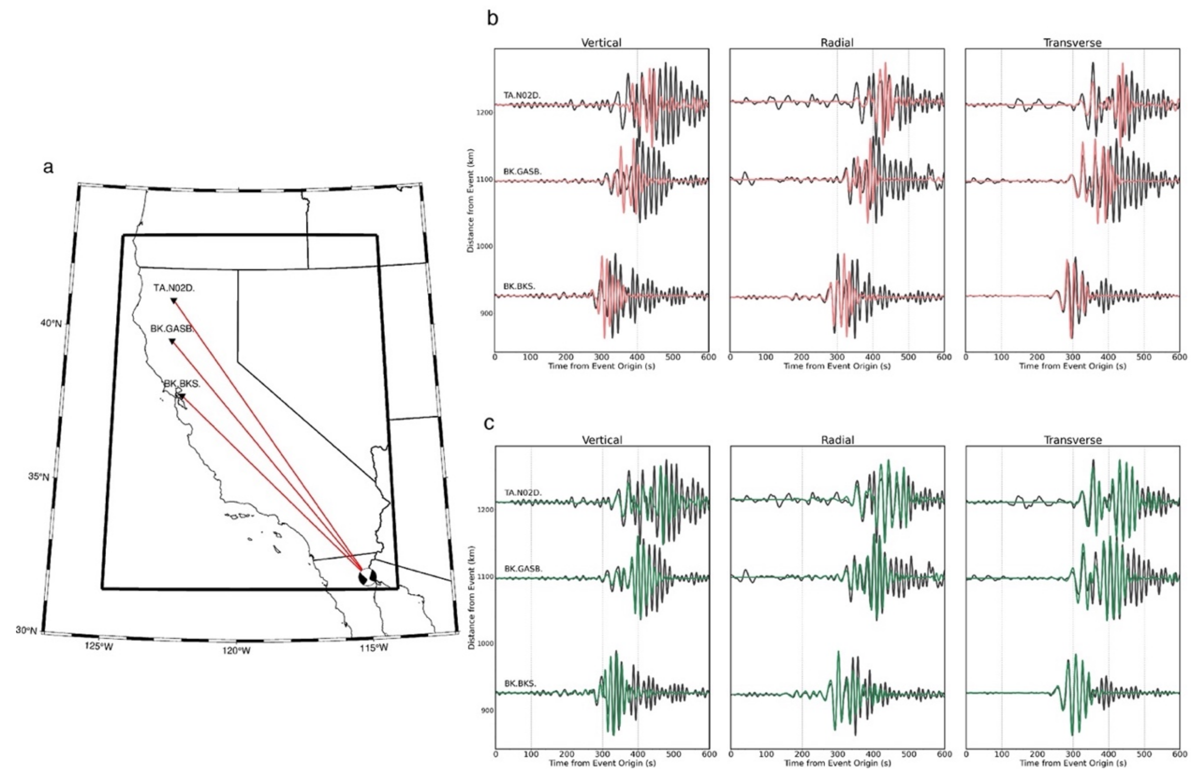

Figure 3.5. Waveform comparison of WUS256 (red waveforms, Panel b) and CANVAS (green waveforms, Panel c) for an M_W 4.76 event in Baja California (20 September 2010, Panel a). Observed data is plotted in black in panels b and c. All data are bandpass filtered to 12-60 seconds.

Figure 3.5 shows waveforms from a M_W 4.76 event in Baja California (20 September 2010). The event occurred between the northernmost terminus of the East Pacific Rise and the Imperial Fault in southern California (Figure 3.5a) and was an aftershock of the 2010 M_W 7.2 El Mayor-Cucapah earthquake. We chose three stations in Northern California to compare observed and synthetic waveforms. The path between the event and stations sample a variety of tectonic regions, including the low velocities of the Salton Sea (e.g., Ajala et al., 2019; Wang et al., 2022) and the Central Valley (e.g., Barak et al., 2015). Station TA.N02D, a temporary USArray station (https://www.usarray.org) over 1200 km from the source, passes through the Sierra Nevada mountains, which is a high velocity region.

Figure 3.5b shows waveform fits for WUS256 (red waveforms; Rodgers et al., 2022) compared to the observed data (black waveforms). For all three stations, WUS256 captures the beginning of the waveform well, though the stations show a slight time delay in the vertical component. However, WUS256 is unable to capture the dispersed surface waves in any component; there are some parts where the synthetics match in phase, but the amplitude of the synthetics is significantly smaller than in the observed data. By contrast, CANVAS captures the dispersed surface waves well, particularly at TA.N02D. CANVAS still struggles to fit the entirety of the surface wave packet. However, CANVAS is still beginning to capture the coda; pushing to lower velocities could help to continue to improve waveform fit.

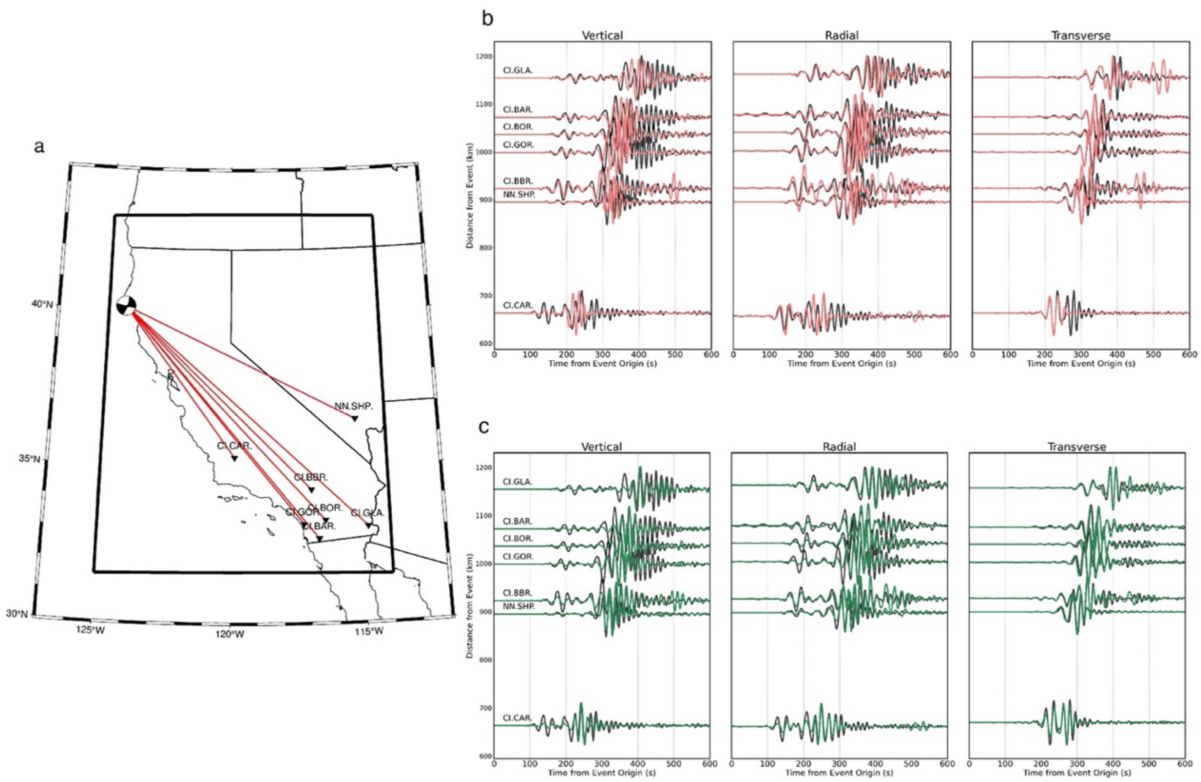

Figure 3.6. Waveform comparison of WUS256 (red waveforms, Panel b) and CANVAS (green waveforms, Panel c) for an M_W 5.72 event off the coast of Mendocino (28 January 2015, Panel a). Observed data is plotted in black in panels b and c. All data are bandpass filtered to 12-60 seconds.

In Figure 3.6a, we show waveforms for an event near the Mendocino Triple Junction that occurred in 2015. This event occurred at 35km depth, so the seismic waves travelled through deeper structure than for the previous event. WUS256 (Figure 3.6b) shows good fits to the first arriving P-waves, as well as the beginning of the surface wave packet; like the Baja California event, WU256 struggles to constrain the dispersed surface waves. The poor fit can likely be explained by the fact that WUS256 has a minimum velocity of 2.4 km/s, so it cannot resolve the wavespeeds of the upper crust. CANVAS can resolve the dispersed surface wave, capturing the entirety of the surface wave packet for most stations. The difference in fit between WUS256 and CANVAS is clearest at station CI.CAR, a Southern California Seismic Network (SCEDC, 2013) station on the Carrizo Plain. The transverse component in particular shows a complex waveform with the Love wave broken up into two distinct sections. WUS256 can resolve the first portion but shows no sensitivity to the later arrivals. CANVAS, on the other hand, captures the entire wave packet, though it is still unable to resolve a portion of the coda.

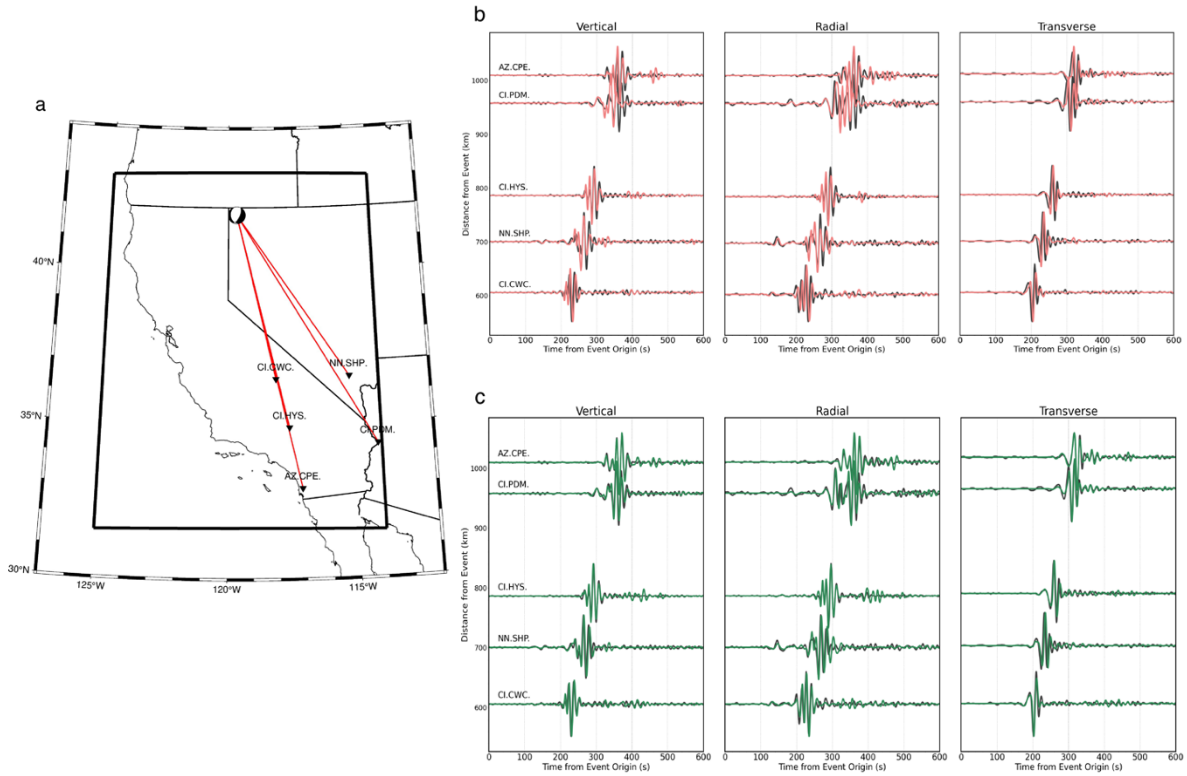

Figure 3.7. Waveform comparison of WUS256 (red waveforms, Panel b) and CANVAS (green waveforms, Panel c) for an Mw 4.56 event in northwestern Nevada (5 November 2014, Panel a). Observed data is plotted in black in panels b and c. All data are bandpass filtered to 12-60 seconds.

For the final illustration, we chose one of the smallest events in the dataset to test the limits of CANVAS's ability to fit observed waveforms. Stations CI.CWC, CI.HYS, and AZ.CPE have the same azimuth, and cross through the Long Valley Caldera at the Nevada/California border (Figure 3.7a). WUS256 shows good fits to the closer stations (CI.CWC, NN.SHP, CI.HYS), though there is a slight time delay in the transverse component. For the more distant stations (CI.PDM, AZ.CPE), WUS256 fits the transverse component well but struggles to fit the vertical and radial components, particularly for CI.PDM. These time delays and poor fits are resolved in CANVAS. The paths where WUS256 shows a time delay pass through the southern Sierra Nevada. The root of the Sierra Nevada in CANVAS is broader and higher velocity than in WUS256, which can explain the discrepancy between the fits obtained for the two models.

The previous three events were contained in the inversion dataset, so we also show data from one of the validation events to highlight CANVAS's performance on unused data. Figure 3.8 shows waveforms from the 13 November 2020 Mina, Nevada earthquake. We chose stations with a wide range of azimuths to investigate CANVAS's performance through as many tectonic regimes as possible. Therefore, we will discuss each waveform, beginning at the north of the model.

BK.MOD is located on the Modoc Plateau near the border of Oregon; the ray path from the Mina earthquake mainly samples the Basin and Range province, which is an extensional tectonic regime that covers a large portion of the American West. WUS256 shows good fit to the first arrivals and the surface wave arrivals; however, it struggles to fit the scattered surface waves. While CANVAS is unable to recover the scattered Rayleigh wave in the vertical component, it can recover a large portion of the scattered surface waves in the radial component. This area is on the northernmost and easternmost edge of CANVAS's path coverage, but the improved waveform fits by CANVAS show that the model is still improving in these regions. The path to BK.WEAV, located in Weaverville, California (southwest of Mount Shasta), samples more tectonic regimes than BK.MOD. The first half of the path traverses the Basin and Range province before crossing the northernmost extent of the Sierra Nevada and the northernmost Central Valley. WUS256 shows good fit to the observed data amplitude-wise but has a slight positive time shift for the body wave, and a slight negative time shift in the Love wave. These time delays are resolved in CANVAS due to both a stronger fast velocity region in the Sierra Nevada and slower velocities in the Central Valley; the change in the Central Valley is the most likely cause of the improved fit in the Love waves. CANVAS is also able to resolve some parts of the dispersed surface waves recorded at BK.WEAV, but does not perform as well as at BK.MOD.

Though BK.FORD (Fort Ord, California) has the shortest path length of all of the stations, the path traverses the Long Valley Caldera near the border with Nevada, the middle of the Sierra Nevada, the Central Valley, and the southern Coast Ranges that bound the western extent of the Central Valley. WUS256 has time delays and amplitude mismatches on all components, though the overall fit to the body waves and the fundamental surface wave arrival is good. CANVAS corrects the time delay in the vertical and radial component, though there is still a small positive time shift in the transverse component. CANVAS is better able to capture the fundamental surface waves, but similarly cannot fit the dispersed surface waves. Resolving smaller-scale structure will likely increase the fit to the scattered surface waves.

The southernmost paths to stations CI.CIA (Channel Islands) and CI.GLA (Glamis, California) sample fewer tectonic regimes than the previous stations, but traverse the Coso Volcanic Field, the Los Angeles Basin (CI.CIA), the Mojave Desert, and close to the Salton Trough (CI.GLA). CI.CIA has very little dispersed energy after the fundamental surface wave arrival; WUS256 shows the best fits at this station, though there is still a positive time shift in the body waves and surface waves in the radial and transverse components. CANVAS shows marginal improvement over WUS256, mainly resolving the time shift and matching the amplitude of the observed body wave first arrival. For CI.GLA, CANVAS similarly fixes the phase shift present in WUS256, but is unable to resolve the complexity in the waveform. This is likely due to fine scale structure to the east of the Salton Sea that is poorly resolved; path coverage in CANVAS is also limited in this area, which could also cause CANVAS to perform similarly to WUS256.

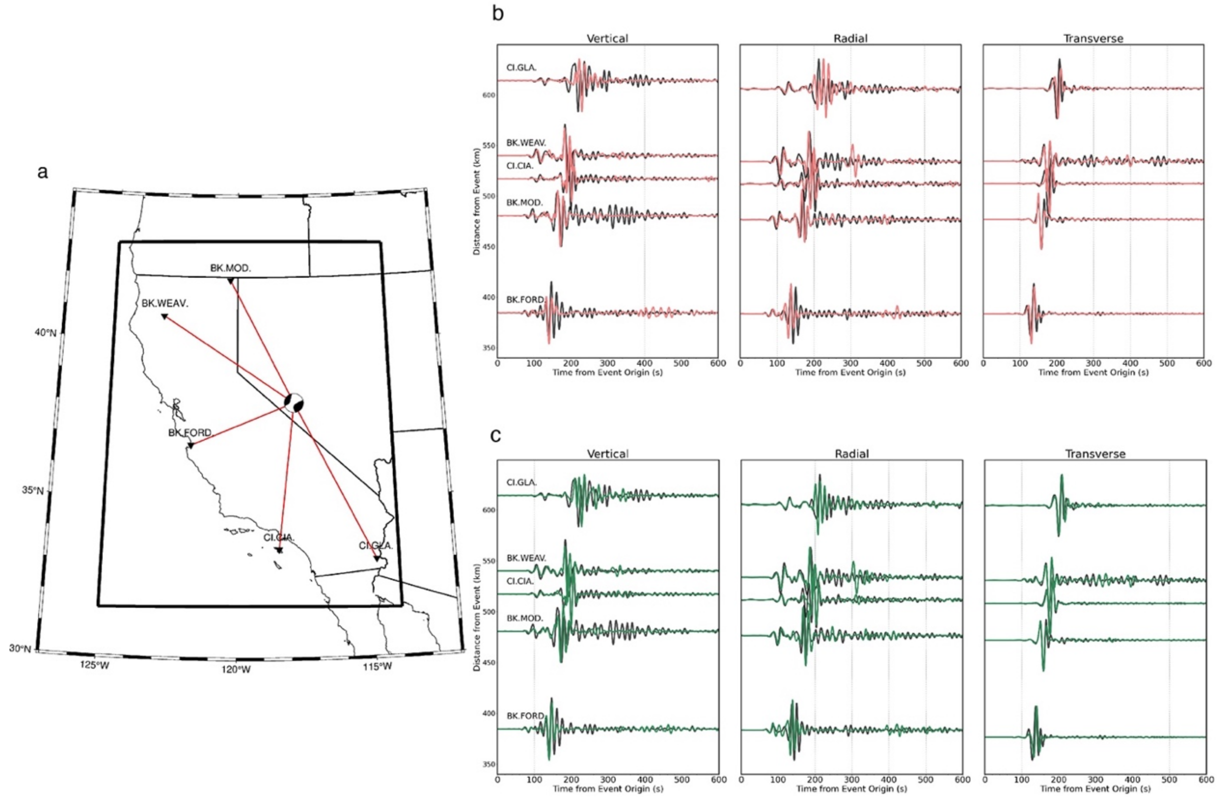

Figure 3.8. Waveform comparison of WUS256 (red waveforms, Panel b) and CANVAS (green waveforms, Panel c) for an M_W 5.21 validation event in Mina, Nevada (13 November 2020, Panel a). Observed data is plotted in black in panels b and c. All data are bandpass filtered to 12-60 seconds.

Overall, we show that CANVAS improves waveform fits compared to WUS256 over a wide variety of paths through the model. CANVAS is particularly powerful at resolving dispersed surface waves over great distances, as seen in the examples of the events in Baja California and Mendocino. Further improvements to waveform fits can be gained by increasing path coverage in northern and southeastern California, as well as constraining smaller-scale structures in the model that are currently beyond the resolution of the model. We hope that iterating CANVAS to shorter periods and extending windows to encompass the entire surface wave packets will continue to improve our ability to fit waveforms.

3.4.3 Tectonic Structure in CANVAS

Since the main motivation behind CANVAS is to optimize waveform fits, we focus on confirming tectonic features seen in other models. Greater tectonic analysis of CANVAS is deferred to a later study once the model is iterated to shorter periods. Because our resolution is limited in eastern Nevada, we extend our interpretation only to California and westernmost Nevada along the Walker Lane.

High Velocity Features

Figure 3.9 shows map view plots of CANVAS at 5 km (Figure 3.9a, c) and 15 km (Figure 3.9b, d) for isotropic V_S (Figure 3.9a-b) and isotropic V_P (Figure 3.9c-d). Figure 3.10 shows cross-sections for isotropic V_S of the model at different latitudes. At 5 km depth, the V_S and V_P model show high velocities in the north in the Klamath Mountain Province of northwestern California (KMP in Figure 3.9a; Snoke and Barnes, 2006). This high-velocity body is thought to be an extension of the Great Valley Ophiolite body, an ultra-mafic feature that underlies the Central Valley (GVOB in Figure 3.9b; Jachens et al., 1995; Godfrey et al., 1997; Thurber et al., 2009). To the east of the GVOB, high velocity features are associated with the root of the Sierra Nevada mountains (SN in Figure 3.9d). The Coast Ranges present as a high velocity anomaly to the west of the Central Valley, extending from the Marin Headlands in northern California to San Luis Obispo in central California. The Coast Ranges present as a stronger high velocity anomaly in V_P, with the faster velocities extending to the terminus of the Coast Ranges near the Mendocino Triple Junction. In southern California, the highest velocities are associated with the Peninsular Ranges along the southwestern coast; similar high velocities have been seen in previous studies (PR in Figure 3.9a; e.g., Tape et al., 2009).

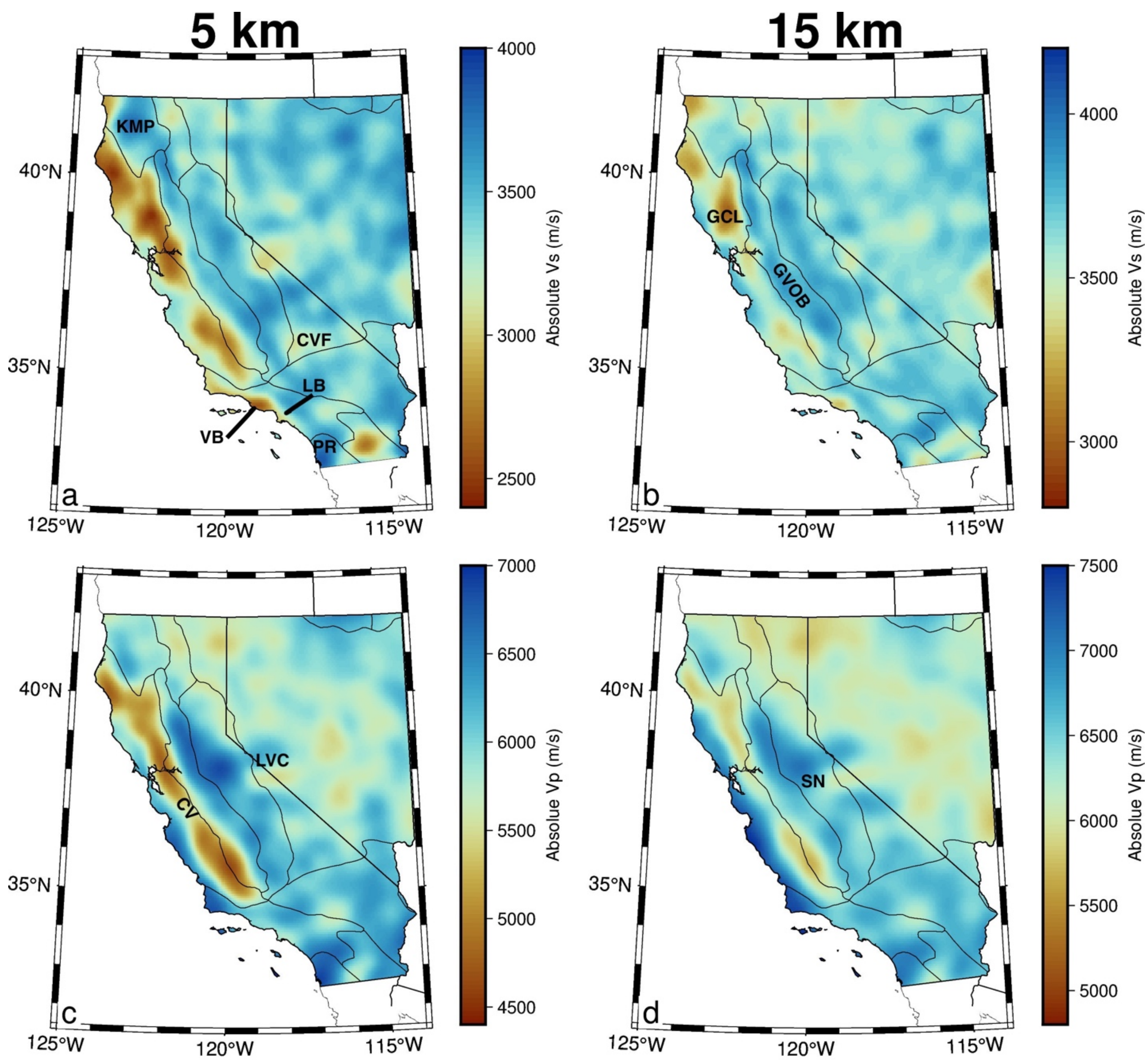

Figure 3.9. Map view of CANVAS at 5 km (a,c) and 15 km (b,d) depth. Panels a and b show absolute isotropic V_S, while panels c and d show absolute isotropic V_P. Warmer colors denote slower regions, while cooler colors denote

faster regions. Tectonic features of interest are labelled throughout: KMP- Klamath Mountain Province, CVF- Coso Volcanic Field, LB- Los Angeles Basin, VB- Ventura Basin, PR- Peninsular Ranges, GCL- Geysers-Clear Lake, GVOB- Great Valley Ophiolite Body, LVC- Long Valley Caldera, CV- Central Valley, SN- Sierra Nevada mountains. The thin black lines in all panels denote the physiographic regions proposed in Fenneman and Johnson (1943).

Low Velocity Features

The most prominent low velocity feature in CANVAS is the Central Valley (CV in Figure 3.9c). The Central Valley is a series of deep sedimentary basins extending from Redding to the north and the Tehachapi mountains in the south. In CANVAS, the Central Valley is divided into a northern and southern section; the central section, which corresponds to the San Joaquin Valley, presents as a faster anomaly because the San Joaquin Valley has a shallower basement depth than other regions of the Central Valley (Faunt et al., 2010). Compared to the geomorphic province location of Fenneman and Johnson (1948), the Central Valley appears offset to the west. This is due to the Central Valley's deepest sediments being to the west (Wentworth et al., 1995); the westward dip of the Central Valley has been seen in other models (e.g., Lin et al., 2010).

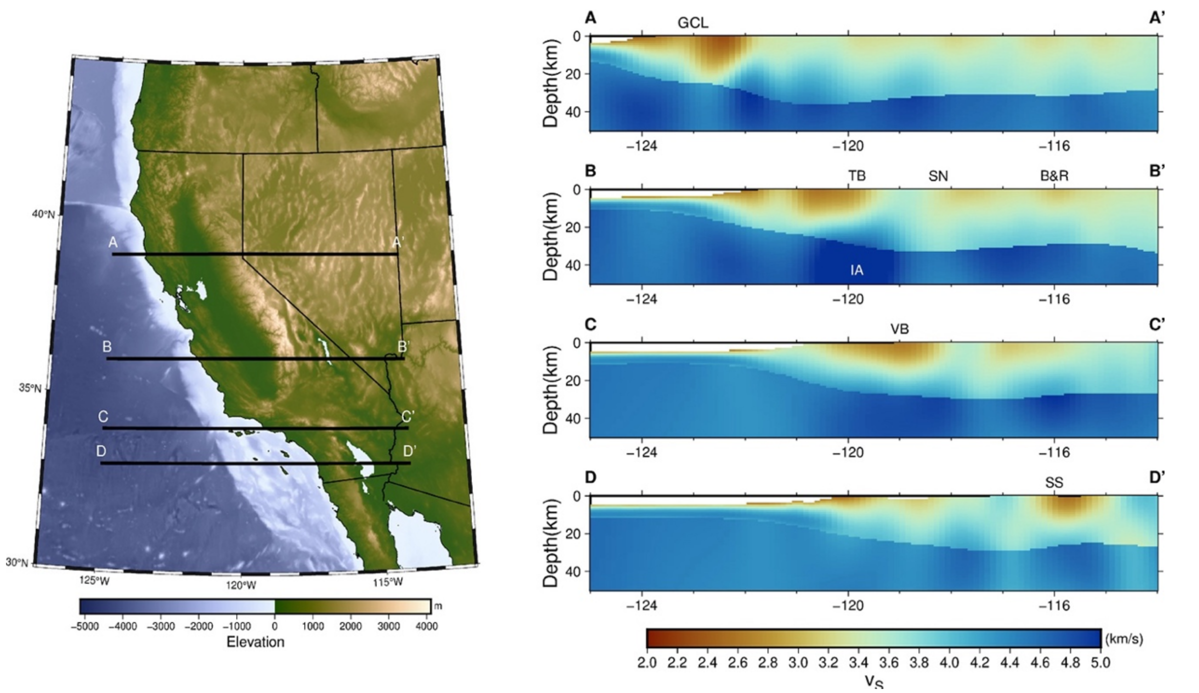

Figure 3.10. Cross-sections of the crust and uppermost mantle in CANVAS. The map on the left shows the location of each cross-section. Section A-A' (39˚N) shows the vertical extent of the Geysers-Clear Lake low velocity anomaly (GCL). Section B-B'(36˚N) includes the Tulare Basin (TB), which is the southernmost extent of the Central Valley, the Sierra Nevada (SN) and its root, the Isabella Anomaly (IA),and a small portion of the Basin and Range province (B&R). Section C-C' (33˚N) shows the Ventura Basin (VB), which extends to about 18km depth in our models. Finally, Section D-D' (32˚N) passes through the Salton Sea (SS). The sharp contrasts in each cross-section denote the Moho, which is held fixed in the model and uses Moho depths from Crust1.0 (Laske et al., 2013).

To the north of the Central Valley, the Geysers-Clear Lake volcanic region is clearly visible, particularly in V_S (GCL in Figure 3.9b, Section A-A' in Figure 3.10). These low velocities have been interpreted as partial melt (Thurber et al., 2009), which also explains the stronger anomaly in V_S than in V_P. To the north of Geysers-Clear Lake, a low velocity anomaly near the Mendocino Triple Junction is thought to be a slab window in the Gorda slab caused by the northward migration of the Mendocino Triple Junction (Beaudoin et al., 1998; Dickinson and

Snyder, 1979; Furlong et al., 2003; Furlong and Schwartz, 2004; Romanowicz, 1980; Verdonck and Zandt, 1994; Zandt and Humphreys, 2008). In northeastern California, low velocity regions are associated with volcanic activity in the Cascade Ranges, including Mount Shasta and the Lassen Volcanic field. Along the border with Nevada, low velocities associated with the Long Valley Caldera are visible in both V_P and V_S at both depths (LVC in Figure 3.9c). In V_S, the Coso Volcanic Field presents as a low velocity anomaly south of the Sierra Nevada (CVF in Figure 3.9a; the low velocities are bounded by the Garlock Fault in the south. To the west, two low velocity features are seen near the coast, corresponding to the Ventura and Los Angeles Basins (VB and LB in Figure 3.9a). The Ventura Basin presents as a strong low velocity anomaly down to 15km; the depth to basement is about 18km (Section C-C' in Figure 3.10; Rand, 1951). The Los Angeles Basin has a maximum depth of 8km (Ma and Clayton, 2016), so is only visible at 5km depth. The Los Angeles Basin is significantly smaller than the Ventura Basin, so we are only beginning to resolve it at the periods of interest. Pushing the model to shorter periods would help to better constrain the Los Angeles Basin. Finally, the Salton Sea appears as a low velocity anomaly in V_S above 10km depth (Section D-D' in Figure 3.10; Share et al., 2021; Wang et al., 2022); this region is associated with thin crust, high heat flows, and Holocene volcanic activity (e.g., Ajala et al., 2019; Wright et al., 2015).

3.6 Conclusions

Though California and Nevada are heavily studied, no adjoint waveform tomography model of the entire state has been proposed. Therefore, we presented CANVAS, an adjoint waveform tomography model of California and Nevada, which is iterated down to a minimum period of 12 seconds. The resolution of CANVAS is still coarse compared to other crustal tomography studies (e.g., Lin et al., 2010; Ma and Clayton, 2016; Tape et al., 2009), but shows significant promise at constraining small-scale tectonic features. To minimize source error that could propagate into our synthetic data, we inverted for source mechanisms after reaching a minimum period of 20 seconds. We illustrated how inverting for source mechanisms produces synthetics that better match observed data, particularly in terms of amplitude; these refined synthetics allow for more windows to be picked, and therefore more data to be included in the inversion. Inverting for sources creates a positive feedback loop between model refinement and source refinement that is necessary to resolve complex waveforms at shorter periods.

We showed that CANVAS significantly improves the fit of dispersed surface waves across a variety of azimuths throughout our domain. Changes in the amplitude of structures within CANVAS have also resolved phase shifts that were present in WUS256. Synthetics for paths that sample particularly tectonically complex regions could be refined further and will benefit from iterating to shorter periods to better resolve smaller-scale tectonic features. We have shown that CANVAS recovers known tectonic structure in California. With no *a priori* information, CANVAS can resolve the Central Valley, the Ventura Basin, the Los Angeles Basin, and the Salton Trough; the velocity structure shown also matches known depths to basement, showing that waveform data alone can provide constraints on basin geometry. Pushing CANVAS to shorter periods would allow for more accurate constraints, particularly on smaller basins such as the Los Angeles Basin. CANVAS could therefore serve as a starting model for regional tomography models throughout California to constrain local structure across the state.

3.7 Acknowledgements

Simulations were run on the Lassen GPU-accelerated platform operated by Livermore Computing. This work was supported in part by Lawrence Livermore National Laboratory Directed Research and Development project 20-ERD-008. This work was performed under the auspices of the U.S. Department of Energy by Lawrence Livermore National Laboratory under Contract DE-AC52-07NA27344. C. Doody is also supported under SCEC Award #22130.

Conclusion

We have presented CANVAS, an adjoint waveform tomography model of California and Nevada that reaches a minimum period of 12 seconds. We began by testing different models for our region to study the effect of starting models on the final inversion results. We showed that using a careful, multi-scale approach, artefacts from the starting model could be mitigated or completely removed. We then inverted source mechanisms for 115 events to minimize source errors. We found that using 3D Green's functions to invert moment tensors produced better and more consistent waveform fits compared to 1D Green's functions. The inverted solutions also averaged 54% higher variance reduction than the Global Centroid Moment Tensor (GCMT) solutions. Finally, we used the new source mechanisms to invert CANVAS to a minimum period of 12 seconds. CANVAS improved waveform fits compared to its starting model, WUS256 (Rodgers et al., 2022), particularly the fits to the dispersed surface waves. The model can accurately resolve the depth to basement of large basins in California, as well as other crustal and upper mantle features.

There are still many next steps that we plan to pursue for all three projects:

Chapter 1. Currently, one caveat to our conclusion that the starting models have no effect on the final models is that it only holds at long wavelengths. To test whether the starting model affects the final inversion results at shorter periods, we plan to run the same test on a smaller region, as iterating to shorter periods on a statewide scale is computationally costly. A good target region would be southern California, as many possible starting models exist in the region (e.g., Tape et al., 2009; Shaw et al., 2015; Suess and Shaw, 2003; Wang et al., 2022). Southern California also has dense station coverage and azimuthally well-distributed sources, which would provide ample path coverage throughout the domain. We hope to run the models to a minimum period of 5 seconds; with the path coverage available in southern California, we expect to come to the same conclusion that the starting model has little effect on the final inversion results if a careful methodology is followed.

Chapter 2. In the near future, we plan on calculating a reciprocal Green's function database in California and Nevada to increase the accessibility of 3D Green's functions. The catalogue proposed in Chapter 2 presently has a minimum magnitude of M_W 4.5. Now that CANVAS has a minimum period of 12 seconds, we plan on inverting source mechanisms for smaller magnitude events to validate the effectiveness of 3D Green's functions on smaller events. We would also like to invert full moment tensors so that we can also include exotic events, such as explosions and mine collapses, in the catalogue. We also intend to automate more steps in selecting the preferred solution, as the current methodology requires making assumptions about double couple percentages and depths that could be biased by the reviewer. We also will include uncertainties in a future catalogue using software such as MTUQ (Silwal and Tape, 2016). Providing uncertainties would give us more confidence in interpreting the tectonic implications of the catalogue results.

Chapter 3. CANVAS is still coarse compared to most crustal tomography models, so iterating the model to shorter periods is necessary to better resolve the upper crustal structure. We hope to iterate CANVAS to a minimum period of 10 seconds. Though an ideal minimum period for rupture propagation modelling would be 1 second, this is too computationally costly to run at the statewide scale. To provide shorter period models for area of high seismic hazard, we plan on using smaller regions around the San Francisco Bay area and the Los Angeles Basin and iterate to 1 second using CANVAS as a starting model. Moving to smaller regions would allow us to include smaller events (down to M_W 3-3.5) and introduce accelerometer data at short periods. We would like to focus on the Bay Area, as southern California is historically better studied. The Bay Area has very dense accelerometer networks used for structural health monitoring, which would provide extensive path coverage throughout the region. We hope that these very short period models can help provide more accurate seismic hazard analysis throughout California.

Bibliography

Abercrombie, R. E., & Ekström, G. (2001). Earthquake slip on oceanic transform faults. *Nature,* **410(6824)**. https://doi.org/10.1038/35065064

Afanasiev, M., Boehm, C., Van Driel, M., Krischer, L., Rietmann, M., May, D. A., Knepley, M. G., & Fichtner, A. (2019). Modular and flexible spectral-element waveform modelling in two and three dimensions. *Geophysical Journal International, 216*(3). https://doi.org/10.1093/gji/ggy469

Ajala, R., Persaud, P., Stock, J. M., Fuis, G. S., Hole, J. A., Goldman, M., & Scheirer, D. (2019). Three-dimensional basin and fault structure from a detailed seismic velocity model of Coachella Valley, Southern California. *Journal of Geophysical Research: Solid Earth, 124*(5). https://doi.org/10.1029/2018JB016260

Aki, K., Christoffersson, A., & Husebye, E. S. (1977). Determination of the three-dimensional seismic structure of the lithosphere. *Journal of Geophysical Research, 82*(2). https://doi.org/10.1029/JB082i002p00277

Aki, K., & Lee, W. H. K. (1976). Determination of three-dimensional velocity anomalies under a seismic array using first p arrival times from local earthquakes – 1. A homogeneous initial model. *J Geophys Res, 81*(23). https://doi.org/10.1029/JB081i023p04381

Anderson, D. L. (1971). The San Andreas Fault. *Scientific American*, **225(5)**. https://doi.org/10.1038/scientificamerican1171-52

Arthur, D. & Vassilvitskii, S. (2007). K-means++: The advantages of careful seeding. *Proceedings of the Eighteenth Annual ACM-SIAM Symposium on Discrete Algorithms. https://doi.org/10.1145/1283383.1283494*

Barak, S., Klemperer, S. L., & Lawrence, J. F. (2015). San Andreas Fault dip, Peninsular Ranges mafic lower crust and partial melt in the Salton Trough, Southern California, from ambient-noise tomography. *Geochemistry, Geophysics, Geosystems,* **16(11)**. https://doi.org/10.1002/2015GC005970

Beaudoin, B. C., Hole, J. A., Klemper, S. L., & Tréhu, A. M. (1998). Location of the southern edge of the Gorda slab and adjacent asthenospheric window: results from seismic profiling and gravity. *Journal of Geophysical Research: Solid Earth*, **103(B12)**, 30101-30115. https://doi.org/10.1029/98JB02231

Blom, N., C. Boehm & A. Fichtner (2017). Synthetic inversions for density using seismic and gravity data, *Geophys. J. Int.*, 209(2), 1204–1220, https://doi.org/10.1093/gji/ggx076

Boehm, C., Martiartu, N. K., Vinard, N., Balic, I. J., & Fichtner, A. (2018). Time-domain spectral-element ultrasound waveform tomography using a stochastic quasi-newton method. *Proceedings of SPIE.* https://doi.org/10.1117/12.2293299

Boehm, C., L. Krischer, I. Ulrich, P. Marty, M. Afanasiev, & A. Fichtner (2022). Using optimal transport to mitigate cycle-skipping in ultrasound computed tomography. *Proc. SPIE 12038, Medical Imaging 2022: Ultrasonic Imaging and Tomography*, 1203809 (4 April 2022). https://doi.org/10.1117/12.2605894.

Bowden, D. C., Kohler, M. D., Tsai, V. C., & Weeraratne, D. S. (2016). Offshore Southern California lithospheric velocity structure from noise cross-correlation functions. *Journal of Geophysical Research: Solid Earth,* **121(5)**. https://doi.org/10.1002/2016JB012919

Boyd, O. S., Dreger, D. S., Gritto, R., & Garcia, J. (2018). Analysis of seismic moment tensors and in situ stress during Enhanced Geothermal System development at The Geysers geothermal field, California. *Geophysical Journal International,* **215(2)**. https://doi.org/10.1093/GJI/GGY326

Boyd, O. S., Dreger, D. S., Lai, V. H., & Gritto, R. (2015). A systematic analysis of seismic moment tensor at the geysers geothermal field, California. *Bulletin of the Seismological Society of America,* **105(6)**. https://doi.org/10.1785/0120140285

Bozdag, E., Peter, D., Lefebvre, M., Komatitsch, D., Tromp, J., Hill, J., Podhorszki, N., and Pugmire, D. (2016). Global adjoint tomography: first-generation model. *Geophysical Journal International*, **207(3)**. https://doi.org/10.1093/gji/ggw356

Bui-Thanh, T., Ghattas, O., Martin, J., & Stadler, G. (2013). A computational framework for infinite-dimensional Bayesian inverse problems part 1: the linearized case, with application to global seismic inversion. *SIAM Journal on Scientific Computing*, **35(6)**, https://doi.org/10.1137/12089586X

Bunks, C., Saleck, F. M., Zaleski, S., & Chavent, G. (1995). Multiscale seismic waveform inversion. *Geophysics, 60*(5). https://doi.org/10.1190/1.1443880

Chai, C., Ammon, C. J., Maceira, M., & Herrmann, R. B. (2015). Inverting interpolated receiver functions with surface wave dispersion and gravity: Application to the western U.S. and adjacent Canada and Mexico. *Geophysical Research Letters, 42*(11). https://doi.org/10.1002/2015GL063733

Chen, P., Zhao, L., & Jordan, T. H. (2007). Full 3D tomography for the crustal sturcture of the Los Angeles region. *Bulletin of the Seismological Society of America*, **97(4)**, 1094-1120. https://doi.org/10.1785/0120060222

Cheng, Y., Allen, R. M., & Taira, T. (2023). A new focal mechanism calculation algorithm (REFOC) using inter-event relative radiation patterns: application to the earthquakes in the

Parkfield area. *Journal of Geophysical Research: Solid Earth*, **128(3)**. https://doi.org/10.1029/2022JB025006

Chiang, A., Rodgers, A., Krischer, L., Afanasiev, M., Boehm, C., Simmons, N., & Doody, C. (2021). Regional moment tensor inversion using a three-dimensional Earth model and its application to the Western United States (abstract S13B-06). *Presentation at Fall 2021, American Geophysical Union Annual Meeting*.

Chiang, A., & USDOE National Nuclear Security Administration. (2020). Time Domain Moment Tensor Inversion in Python (Version 0.1) [Computer software]. https://www.osti.gov//servlets/purl/1602708. https://doi.org/10.11578/dc.20200303.3

Chow, B., Kaneko, Y., Tape, C., Modrak, R., & Townend, J. (2020). An automated workflow for adjoint tomography-waveform misfits and synthetic inversions for the North Island, New Zealand. *Geophysical Journal International, 223*(3). https://doi.org/10.1093/gji/ggaa381

Conn, A.R., N.I.M. Gould & P. L. Toint (2000). Trust Region Methods, SIAM-MPS, Philadelphia, USA.

Cottaar, S., & Lekic, V. (2016). Morphology of seismically slow lower-mantle structures. *Geophysical Journal International, 207*(2). https://doi.org/10.1093/gji/ggw324

Craig, T. J. (2019). Accurate Depth Determination for Moderate-Magnitude Earthquakes Using Global Teleseismic Data. *Journal of Geophysical Research: Solid Earth,* **124(2)**. https://doi.org/10.1029/2018JB016902

Dalton, C. A., & Ekström, G. (2006). Constraints on global maps of phase velocity from surface-wave amplitudes. *Geophysical Journal International,* **167(2)**. https://doi.org/10.1111/j.1365-246X.2006.03142.x

Dickinson, W. R. & Synder, W. S. (1979). Geometry of subducted slabs related to San Andreas transform. *The Journal of Geology*, **87(6)**, 609-627.

Doody, C. (2023a). Dataset for 'Comparing adjoint waveform tomography models of California using different starting models.' [Dataset]. Zenodo. https://doi.org/10.5281/zenodo.7830683

Doody, C. (2023b). clairedd/fwi-starting-model-comp: v1.0.0 (v1.0.0). Zenodo. https://doi.org/10.5281/zenodo.7839070

Doody, C. D., Rodgers, A. J., Afanasiev, M., Boehm, C. T., Krischer, L., Chiang, A., & Simmons, N. (2023). Comparing adjoint waveform model of California using different starting models. *Journal of Geophysical Research: Solid Earth*. https://doi.org/10.1029/2023JB026463

Doughtery, S. L., Jiang, C., Clayton, R. W., Schmandt, B., & Hansen, S. M. (2020). Seismic evidence for a fossil slab origin for the Isabella Anomaly. *Geophysical Journal International*, **224(2)**, 1188-1196. Https://doi.org/10.1093/gji/ggaa472

Dreger, D. S. (2003). TDMT_INV: time domain seismic moment tensor inversion. *International Geophysics*, **81**, 1627-1627. https://doi.org/10.1016/S0074-6142(03)80290-5

Dreger D. S. & Romanowicz, B. (1994) Source characteristics of events in the San Francisco Bay region. *US Geologic Survey Open File Report*, **94–176**: 301–309.

Dreger, D. S., Tkalčić, H., & Johnston, M. (2000). Dilational processes accompanying earthquakes in the Long Valley Caldera. *Science,* **288(5463)**. https://doi.org/10.1126/science.288.5463.122

Dreger, D., Uhrhammer, R., Pasyanos, M., Franck, J., & Romanowicz, B. (1998). Regional and far-regional earthquake locations and source parameters using sparse broadband networks: A test on the Ridgecrest sequence. *Bulletin of the Seismological Society of America,* **88(6)**. https://doi.org/10.1785/bssa0880061353

Dreger, D., & Woods, B. (2002). Regional distance seismic moment tensors of nuclear explosions. *Tectonophysics,* **356(1-3)**. https://doi.org/10.1016/S0040-1951(02)00381-5

Durek, J. J., & Ekström, G. (1996). A radial model of anelasticity consistent with long-period surface-wave attenuation. *Bulletin of the Seismological Society of America,* **86(1)**.

Dziewonski, A. M. & Anderson, D. L. (1981). Preliminary reference earth model. *Physics of the Earth and Planetary Interiors*, **25**, 297-356.

Dziewonski, A. M., Chou, T. A., & Woodhouse, J. H. (1981). Determination of earthquake source parameters from waveform data for studies of global and regional seismicity. *Journal of Geophysical Research,* **86**. https://doi.org/10.1029/JB086iB04p02825

Dziewonski, A. M., Hager, B. H., & O'Connell, R. J. (1977). Large-scale heterogeneities in the lower mantle. *Journal of Geophysical Research*, **82(2)**. https://doi.org/10.1029/JB082i002p00239.

Dziewonski, A. M., & Woodhouse, J. H. (1983). An experiment in systematic study of global seismicity: Centroid- moment tensor solutions for 201 moderate and large earthquakes in 1981. *Journal of Geophysical Research,* **88(4).** https://doi.org/10.1029/JB088iB04p03247

Ekström, G., Nettles, M., & Dziewoński, A. M. (2012). The global CMT project 2004-2010: Centroid-moment tensors for 13,017 earthquakes. *Physics of the Earth and Planetary Interiors, 200-201*. https://doi.org/10.1016/j.pepi.2012.04.002

Eymond, W. K. Jordan, T. H. (2019). Tectonic regionalization of the Southern California crust from tomographic cluster analysis. *Journal of Geophysical Research*, **124**, 11840-11865. https://doi.org/10.1029/2019JB018423.

Faunt, C. C., Belitz, K., & Hanson, R. T. (2010). Development of a three-dimensional model of sedimentary texture in valley-fill deposits of Central Valley, California, USA. *Hydrogeology Journal,* **18(3)**. https://doi.org/10.1007/s10040-009-0539-7

Fenneman N. M., and Johnson, D. W. (1946). Physiographic divisions of the conterminous United States. *U.S. Geological Survey*. https://doi.org/10.3133/70207506

Fichtner, A. (2010). Full seismic waveform modelling and inversion. Berlin, Heidelberg: Springer. https://doi.org/10.1007/978-3-642-15807-0

Fichtner, A., Bunge, H.-P., & Igel, H. (2006). The adjoint method in seismology I. Theory. *Physics of the Earth and Planetary Interiors*, **157**(1-2), 86-104. https://doi.org/10.1016/j.pepi.2006.03.016

Fichtner, A., Kennett, B. L. N., Igel, H., & Bunge, H. P. (2008). Theoretical background for continental- and global-scale full-waveform inversion in the time-frequency domain. *Geophysical Journal International,* **175(2)**. https://doi.org/10.1111/j.1365-246X.2008.03923.x

Fichtner, A., Kennett, B. L. N., Igel, H., & Bunge, H.-P. (2009). Full seismic waveform tomography for upper-mantle structure in the Australasian region using adjoint methods. *Geophysical Journal International, 179*(3). https://doi.org/10.1111/j.1365-246X.2009.04368.x

Fichtner, A., & Leeuwen, T. V. (2015). Resolution analysis by random probing. *Journal of Geophysical Research: Solid Earth, 120*(8). https://doi.org/10.1002/2015JB012106

Flath, H. P., Wilcox, L. C., Akçelik, V., Hill, J., van Bloemen Waanders, B., & Ghattas, O. (2011). Fast algorithms for Bayesian uncertainty quantification in large-scale linear inverse problems based on low-rank partial Hessian approximations. *SIAM Journal on Scientific Computing*, **33(1)**, 407-432. https://doi.org/10.1137/090780717

Fletcher, J. B., & Erdem, J. (2017). Shear-wave Velocity Model from Rayleigh Wave Group Velocities Centered on the Sacramento/San Joaquin Delta. *Pure and Applied Geophysics,* **174(10)**. https://doi.org/10.1007/s00024-017-1587-x

Flinders, A. F., Shelly, D. R., Dawson, P. B., Hill, D. P., Tripoli, B., & Shen, Y. (2018). Seismic evidence for significant melt beneath the Long Valley Caldera, California, USA. *Geology, 46*(9). https://doi.org/10.1130/G45094.1

Florez, M. A., & Prieto, G. A. (2017). Precise relative earthquake depth determination using array processing techniques. *Journal of Geophysical Research: Solid Earth,* **122(6)**. https://doi.org/10.1002/2017JB014132

Foster, A., Ekström, G., & Hjörleifsdóttir, V. (2014). Arrival-angle anomalies across the USArray Transportable Array. *Earth and Planetary Science Letters,* **402**. https://doi.org/10.1016/j.epsl.2013.12.046French, S., Lekic, V., & Romanowicz, B. (2013). Waveform tomography reveals channeled flow at the base of the oceanic asthenosphere. *Science*, **342(6155)**, 227-230. https://doi.org/10.1126/science.1241514.

French, S. & Romanowicz, B. (2014). Whole-mantle radially anisotropic shear velocity structure from spectral-element waveform tomography. *Geophysical Journal International*, **199(3)**, 1303-1327. https://doi.org/10.1093/gji/ggu334.

Fukuyama, E., Ishida, M., Dreger, D., & Kawai, H. (1998). Automated seismic moment tensor determination by using on-line broadband seismic waveforms. *Zishin*, **51**, 149-156.

Furlong, K. P., Lock, J., Guzofski, C., Whitlock, J., & Benz, H. (2003). The mendocino crustal conveyor: Making and breaking the California crust. *International Geology Review,* **45(9)**. https://doi.org/10.2747/0020-6814.45.9.767

Furlong, K. P., & Schwartz, S. Y. (2004). Influence of the Mendocino Triple Junction on the tectonics of coastal California. *Annual Review of Earth and Planetary Sciences*, **32(1)**, 403-433. https://doi.org/10.1146/annurev.earth.32.101802.120252

Gao, G., Florez, H., Vink, J. C., Wells, T. J., Saaf, F., & Blom, C. P. A. (2021). Performance analysis of trust region subproblem solvers for limited-memory distributed BFGS optimization method. *Frontiers in Applied Mathematics and Statistics, 7.* https://doi.org/10.3389/fams.2021.673412

Gao, Y., Tilmann, F., van Herwaarden, D. P., Thrastarson, S., Fichtner, A., Heit, B., Yuan, X., & Schurr, B. (2021). Full waveform inversion beneath the Central Andes: Insight into the dehydration of the Nazca slab and delamination of the back-arc lithosphere. *Journal of Geophysical Research: Solid Earth, 126*(7). https://doi.org/10.1029/2021JB021984

Gebraad, L., Boehm, C., & Fichtner, A. (2020). Bayesian elastic full-waveform inversion using Hamiltonian monte carlo. *Journal of Geophysical Research: Solid Earth, 125*(3). https://doi.org/10.1029/2019JB018428

Godfrey, N. J., Beaudoin, B. C., Klemperer, S. L., Levander, A., Luetgert, J., Meltzer, A., Mooney, W., & Tréhu, A. (1997). Ophiolitic basement to the Great Valley forearc basin, California, from seismic and gravity data: Implications for crustal growth at the North American continental margin. *Bulletin of the Geological Society of America,* **109(12)**. https://doi.org/10.1130/0016-7606(1997)109

Han, L., Hole, J. A., Stock, J. M., Fuis, G. S., Williams, C. F., Delph, J. R., Davenport, K. K., Livers, A. J. (2016). Seismic imaging of the metamorphism of young sediment into new crystalline crust in the actively rifting Imperial Valley, California. *Geochemistry, Geophysics, Geosystems*, **17(11)**, 4566-4584. https://doi.org/10.1002/2016GC006610

Hatem, A., Reitman, N. G., Briggs, R. W., Gold, R. D., Jobe, J. A., & Burgette, R. J. (2022). Western U.S. geologic deformation model for use in the U.S. National Seismic Hazard Model 2023. *Seismological Research Letters*, **93(6)**, 3053-3067. https://doi.org/10.1785/0220220154

Hawley, W. B., & Allen, R. M. (2019). The fragmented death of the Farallon Plate. *Geophysical Research Letters, 46*(13). https://doi.org/10.1029/2019GL083437

Hayes, G. P., Moore, G. L., Portner, D. E., Hearne, M., Flamme, H., Furtney, M., & Smoczyk, G. M. (2018). Slab2, a comprehensive subduction zone geometry model. *Science, 362*(6410). https://doi.org/10.1126/science.aat4723

Herrmann, R. B. 2013. "Computer Programs in Seismology: An Evolving Tool for Instruction and Research." *Seismological Research Letters* **84 (6)**, 1081-1088. https://doi.org/10.1785/0220110096

Hjörleifsdóttir, V., & Ekström, G. (2010). Effects of three-dimensional Earth structure on CMT earthquake parameters. *Physics of the Earth and Planetary Interiors,* **179(3-4)**. https://doi.org/10.1016/j.pepi.2009.11.003

Hutton, K., Hauksson, E., Clinton, J., Franck, J., Guarino, A., Scheckel, N., Given, D. & Yong, A. (2006). *Seismological Research Letters*, **77(3)**, 389-395.

Ichinose, G. A., Anderson, J. G., Smith, K. D., & Zeng, Y. (2003). Source parameters of eastern California and western Nevada earthquakes from regional moment tensor inversion. *Bulletin of the Seismological Society of America,* **93(1)**. https://doi.org/10.1785/0120020063

Jachens, R. C., Griscom, A., & Roberts, C. W. (1995). Regional extent of Great Valley basement west of the Great Valley, California: implications for extensive tectonic wedging in the California Coast Ranges. *Journal of Geophysical Research,* **100**. https://doi.org/10.1029/95jb00718

Jiang, C., Schmandt, B., Hansen, S. M., Dougherty, S. L., Clayton, R. W., Farrell, J., & Lin, F. (2018). Rayleigh and S wave tomography constraints on subduction termination and lithospheric foundering in central California. *Earth and Planetary Science Letters*, **488**, 14-26. https://doi.org/10.1016/j.epsl.2018.02.009

Kanasewich, E. R. (1981). Time sequence analysis in geophysics. University of Alberta Press.

Kennett, B. L. N., Engdahl, E. R., & Buland, R. (1995). Constraints on seismic velocities in the Earth from traveltimes. *Geophysical Journal International, 122*(1), https://doi.org/10.1111/j.1365-246X.1995.tb03540.x

Kikuchi, M. & Kanamori, H. (1991). Inversion of complex body waves—III. *Bulletin of the Seismological Society of America*, **81(6)**, 2335-2350.

Kluyver, T., Ragan-Kelley, B., Pérez, F., Granger, B., Bussonnier, M., Frederic, J., Kelley, K., Hamrick, J., Grout, J., Corlay, S., Ivanov, P., Avila, D., Abdalla, S., & Willing, C. (2016). Jupyter notebooks—a publishing format for reproducible computational workflows. Paper presented at *Positioning and power in academic publishing: players, agents and agendas: proceedings of the 20th international conference on electronic publishing.* Amsterdam: IOS Press, 87-90. https://doi.org/10.3233/978-1-61499-649-1-87

Kohler, M. D. (1999). Lithospheric deformation beneath the San Gabriel mountains in the southern California Transverse Ranges. *Journal of Geophysical Research: Solid Earth, 104,* https://doi.org/10.1029/1999jb900141

Komatitsch, D. & J. Tromp (2002a). Spectral-element simulations of global seismic wave propagation—I. Validation, *Geophys. J. Int.*, **149(2)**, 390–412, https://doi.org/10.1046/j.1365-246X.2002.01653.x

Komatitsch, D. & J. Tromp (2002b). Spectral-element simulations of global seismic wave propagation—II. Three-dimensional models, oceans, rotation and self gravitation, *Geophys. J. Int.*, **150(1)**, 303–318, https://doi.org/10.1046/j.1365-246X.2002.01716.x

Krischer, L., Fichtner, A., Boehm, C., & Igel, H. (2018). Automated large-scale full seismic waveform inversion for North America and the North Atlantic. *Journal of Geophysical Research: Solid Earth, 123*(7). https://doi.org/10.1029/2017JB015289

Krischer, L., Fichtner, A., Zukauskaite, S., & Igel, H. (2015). Large-scale seismic inversion framework. *Seismological Research Letters, 86*(4). https://doi.org/10.1785/0220140248

Krischer, L., Smith, J., Lei, W., Lefebvre, M., Ruan, Y., de Andrade, E. S., Podhorszki, N., Bozdağ, E., & Tromp, J. (2016). An adaptable seismic data format. *Geophysical Journal International, 207*(2). https://doi.org/10.1093/gji/ggw319

Kristeková, M., Kristek, J., & Moczo, P. (2009). Time-frequency misfit and goodness-of-fit criteria for quantitative comparison of time signals. *Geophysical Journal International, 178*(2). https://doi.org/10.1111/j.1365-246X.2009.04177.x

Kristeková, M., Kristek, J., Moczo, P., & Day, S. M. (2006). Misfit criteria for quantitative comparison of seismograms. *Bulletin of the Seismological Society of America, 96*(5). https://doi.org/10.1785/0120060012

Laske, G., Masters, G., Ma, Z., & Pasyanos, M. (2013). Update on CRUST1.0- a 1-degree global model of Earth's crust. *Geophysical Research Abstracts,* **15**, Abstract EGU2013-2658.

Lawson, A. C. (1910). The California Earthquake of April 18, 1906. *Bulletin of the American Geographical Society,* **42(2)**. https://doi.org/10.2307/199583

Lei, W., Ruan, Y., Bozdag, E., Peter, D., Lefebvre, M., Komatitsch, D., Tromp, J., Hill, J., Podhorszki, N., & Pugmire, D. (2020). Global adjoint tomography—model GLAD-M25. *Geophysical Journal International*, **223(1)**. https://doi.org/10.1093/gji/ggaa253.

Lekic, V., Cottaar, S., Dziewonski, A., & Romanowicz, B. (2012). Cluster analysis of global lower mantle tomography: A new class of structure and implications for chemical heterogeneity. *Earth and Planetary Science Letters, 357-358.* https://doi.org/10.1016/j.epsl.2012.09.014

Lekic, V., & Romanowicz, B. (2011). Tectonic regionalization without a priori information: A cluster analysis of upper mantle tomography. *Earth and Planetary Science Letters, 308*(1-2), https://10.1016/j.epsl.2011.05.050

Lévěque, J. -, Rivera, L., & Wittlinger, G. (1993). On the use of the checker-board test to assess the resolution of tomographic inversions. *Geophysical Journal International, 115*(1). https://doi.org/10.1111/j.1365-246X.1993.tb05605.x

Li, C., Peng, Z., Yao, D., Meng, X., & Zhai, Q. (2022). Temporal changes of seismicity in Salton Sea Geothermal Field due to distant earthquakes and geothermal productions. *Geophysical Journal International*, *232*(1), 287-299. https://doi.org/10.1093/gji/ggac324

Lin, F. C., Li, D., Clayton, R. W., & Hollis, D. (2013). High-resolution 3D shallow crustal structure in Long Beach, California: Application of ambient noise tomography on a dense seismic array. *Geophysics,* **78(4)**. https://doi.org/10.1190/geo2012-0453.1

Lin, F. C., Tsai, V. C., & Schmandt, B. (2014). 3-D crustal structure of the western United States: Application of Rayleigh-wave ellipticity extracted from noise cross-correlations. *Geophysical Journal International,* **198(2)**. https://doi.org/10.1093/gji/ggu160

Lin, G., Thurber, C. H., Zhang, H., Hauksson, E., Shearer, P. M., Waldhauser, F., Brocher, T. M., & Hardebeck, J. (2010). A California statewide three-dimensional seismic velocity model from both absolute and differential times. *Bulletin of the Seismological Society of America, 100*(1). https://doi.org/10.1785/0120090028

Lin, G., & Wu, B. (2018). Seismic velocity structure and characteristics of induced seismicity at the Geysers Geothermal Field, Eastern California. *Geothermics, 71.* https://doi.org/10.1016/j.geothermics.2017.10.003

Liu, Q., Beller, S., Lei, W., Peter, D., & Tromp, J. (2022). Pre-conditioned BFGS-based uncertainty quantification in elastic full-waveform inversion, Geophys. J. Int., 228(2), 796 815. https://doi.org/10.1093/gji/ggab375

Liu, Q., & Gu, Y. J. (2012). Seismic imaging: From classical to adjoint tomography. *Tectonophysics*, **566-567**, 31-66.https://doi.org/10.1016/j.tecto.2012.07.006

Liu, Q., & Peter, D. (2019). Square-root variable metric based elastic full-waveform inversion-part 2: Uncertainty estimation. *Geophysical Journal International,* **218(2)**. https://doi.org/10.1093/gji/ggz137

Liu, Q., Polet, J., Komatitsch, D., & Tromp, J. (2004). Spectral-element moment tensor inversions for earthquakes in southern California. *Bulletin of the Seismological Soceity of America*, **94(5)**, 1748-1761. https://doi.org/10.1785/012004038

Lloyd, S. P. (1982). Least squares quantization in PCM. *IEEE Transactions on Information Theory, 28*(2). https://doi.org/10.1109/TIT.1982.1056489

Ma, Y., & Clayton, R. W. (2016). Structure of the Los Angeles Basin from ambient noise and receiver functions. *Geophysical Journal International,* **206(3)**. https://doi.org/10.1093/gji/ggw236

Majer, E. L., & McEvilly, T. V. (1979). Seismological investigations at the geysers geothermal field. *Geophysics,* **44(2)**. https://doi.org/10.1190/1.1440965

Martin, J., Wilcox, L. C., Burstedde, C., & Ghattas, O. (2012). A stochastic Newton MCMC method for large-scale statistical inverse problems with application to seismic inversion. *SIAM Journal on Scientific Computing*, **34(3)**, A1460-A1487. https://doi.org/10.1137/110845598

Métivier, L., Brossier, R., Mérigot, Q., Oudet, E., & Virieux, J. (2016). An optimal transport approach for seismic tomography: Application to 3D full waveform inversion. *Inverse Problems, 32*(11). https://doi.org/10.1088/0266-5611/32/11/115008

Minson, S. E., & Dreger, D. S. (2008). Stable inversions for complete moment tensors. *Geophysical Journal International,* **174(2)**. https://doi.org/10.1111/j.1365-246X.2008.03797.x

Modrak, R. T., Borisov, D., Lefebvre, M., & Tromp, J. (2018). SeisFlows—Flexible waveform inversion software. *Computers and Geosciences, 115.* https://doi.org/10.1016/j.cageo.2018.02.004

Modrak, R., & Tromp, J. (2016). Seismic waveform inversion best practices: Regional, global and exploration test cases. *Geophysical Journal International, 206*(3), https://doi.org/10.1093/gji/ggw202

Nocedal, J. & S. Wright (2006). Numerical Optimization, New York: Springer.

Nolan, T. B. (1943). *The Basin and Range Province in Utah, Nevada, and California*. https://doi.org/10.3133/pp197D

Northern California Earthquake Data Center. (2014). Berkeley Digital Seismic Network (BDSN) [Dataset]. Northern California Earthquake Data Center. https://doi.org/10.7932/BDSN

Panning, M., Dreger, D., & Tkalčić, H. (2001). Near-source velocity structure and isotropic moment tensors: A case study of the Long Valley Caldera. *Geophysical Research Letters,* **28(9)**. https://doi.org/10.1029/2000GL012389

Pasyanos, M. E. (2005). A variable resolution surface wave dispersion study of Eurasia, North Africa, and surrounding regions. *Journal of Geophysical Research: Solid Earth, 110*(12). https://doi.org/10.1029/2005JB003749

Pasyanos, M. E., Dreger, D. S., & Romanowicz, B. (1996). Toward real-time estimation of regional moment tensors. *Bulletin of the Seismological Society of America*, **86**, 1255-1269.

Pearson, K. (1895). Notes on regression and inheritance in the case of two parents. *Proceedings of the Royal Society of London*, **58**, 240-242.

Pedregosa, F., Varoquaux, G., Gramfort, A., Michel, V., Thirion, B., Grisel, O., Blondel, M., Prettenhofer, P., Weiss, R., Dubourg, V., Vanderplas, J., Passos, A., Cournapeau, D., Brucher, M., Perrot, M., & Duchesnay, É. (2011). Scikit-learn: Machine learning in python. *Journal of Machine Learning Research*, **12**. https://doi.org/10.5555/1953048.2078195

Płonka, A., Blom, N., & Fichtner, A. (2016). The imprint of crustal density heterogeneities on regional seismic wave propagation. *Solid Earth*, ***7(6)***, 1591–1608. https://doi.org/10.5194/se-7-1591-2016

Pollitz, F. (1999). Regional velocity structure in northern California from inversion of scatteres seismic surface waves. *Journal of Geophysical Research: Solid Earth*, **104(B7)**, 15043-15072. https://doi.org/10.1029/1999JB900118

Powell, R. E., & Weldon, R. J. (1992). Evolution of the San Andreas Fault. *Annual Review of Earth and Planetary Sciences,* **20**. https://doi.org/10.1146/annurev.ea.20.050192.002243

Rand, W. W. (1951). Ventura Basin. *AAPG Bulletin*, **35**. https://doi.org/10.1306/3d934181-16b1-11d7-8645000102c1865d

Rawlinson, N., & Spakman, W. (2016). On the use of sensitivity tests in seismic tomography. *Geophysical Journal International, 205*(2). https://doi.org/10.1093/gji/ggw084

Rawlinson, N., Fichtner, A., Sambridge, M., & Young, M. K. (2014). Seismic tomography and the assessment of uncertainty. *Advances in Geophysics, 55.* https://doi.org/10.1016/bs.agph.2014.08.001

Richards-Dinger, K., & Shearer, P. M. (2000). Earthquake locations in southern California obtained using source-specific station terms. *Journal of Geophysical Research: Solid Earth,* **105**. https://doi.org/10.1029/2000jb900014

Rickers, F., Fichtner, A., & Trampert, J. (2012). Imaging mantle plumes with instantaneous phase measurements of diffracted waves. *Geophysical Journal International, 190*(1). https://doi.org/10.1111/j.1365-246X.2012.05515.x

Ritsema, J., Deuss, A., Van Heijst, H. J., & Woodhouse, J. H. (2011). S40RTS: A degree-40 shear-velocity model for the mantle from new Rayleigh wave dispersion, teleseismic traveltime and normal-mode splitting function measurements. *Geophysical Journal International, 184*(3). https://doi.org/10.1111/j.1365-246X.2010.04884.x

Rodgers, A., Krischer, L., Afanasiev, M., Boehm, C., Doody, C., Chiang, A., & Simmons, N. (2022). WUS256: An adjoint waveform tomography model of the crust and upper mantle of the western United States for improved waveform simulations. *Journal of Geophysical Research: Solid Earth*, **127(7)**, https://doi.org/10.1029/2022JB024549

Rodgers, A. J., Pitarka, A. Pankajakshan, R., Sjögreen, B., & Petersson, N. A. (2020). Regional-scale 3D ground-motion simulations of Mw 7 earthquakes on the Hayward fault, northern California resolving frequencies 0-10 Hz and including site-response corrections. *Bulletin of the Seismological Society of America*, **110(6)**, 2862-2881. https://doi.org/10.1785/0120200147

Romanowicz, B. (1980). Large scale three dimensional P velocity structure beneath the western U.S. and the lost Farallon Plate. *Geophysical Research Letters*, **7(5)**, 345-348. https://doi.org/10.1029/GL007i005p00345

Romanowicz, B. (1982). Moment tensor inversion of long period Rayleigh waves: a new approach. *Journal of Geophysical Research: Solid Earth*, **87(B7)**, 5395-5407. https://doi.org/10.1029/JB087iB07p05395

Romanowicz, B. (2003). Global mantle tomography: Progress status in the past 10 years. *Annual Review of Earth and Planetary Sciences, 31*. https://doi.org/10.1146/annurev.earth.31.091602.113555

Romanowicz, B., & Durek, J. J. (2000). Seismological constraints on attenuation in the earth: A review. *Geophysical Monograph Series*. https://doi.org/10.1029/GM117p0161

Ruan, Y., Lei, W., Modrak, R., Örsvuran, R., Bozdag, E., & Tromp, J. (2019). Balancing unevenly distributed data in seismic tomography: a global adjoint tomography example. *Geophysical Journal International*, **219(2)**, 1225-1236. https://doi.org/10/1093/gji/ggz356

Sawade, L., Beller, S., Lei, W., & Tromp, J. (2022). Global centroid moment tensor solutions in a heterogeneous earth: the CMT3D catalogue. *Geophysical Journal International,* **231(3)**. https://doi.org/10.1093/gji/ggac280

SCEDC (2013): Southern California Earthquake Center. Caltech [Dataset]. https://doi.org/10.7909/C3WD3xH1

Scognamiglio, L., Tinti, E., & Michelini, A. (2009). Real-time determination of seismic moment tensor for the Italian region. *Bulletin of the Seismological Society of America*, **99(4)**, 2223-2242. https://doi.org/10.1785/0120080104

Share, P. E., Castro, R. R., Vidal-Villegas, J., Mendoza, L., & Ben-Zion, Y. (2021). High-resolution seismic imaging of the plate boundary in northern Baja California and southern California using double-pair double-difference tomography. *Earth and Planetary Science Letters,* **568**. https://doi.org/10.1016/j.epsl.2021.117004

Shaw, J. H., Plesch, A., Tape, C., Suess, M. P., Jordan, T. H., Ely, G., Hauksson, E., Tromp, J., Tanimoto, T., Graves, R., Olsen, K., Nicholson, C., Maechling, P. J., Rivero, C., Lovely, P., Brankman, C. M., & Munster, J. (2015). Unified Structural Representation of the southern California crust and upper mantle. *Earth and Planetary Science Letters,* **415**. https://doi.org/10.1016/j.epsl.2015.01.016

Shuler, A., Ekström, G., & Nettles, M. (2013). Physical mechanisms for vertical-CLVD earthquakes at active volcanoes. *Journal of Geophysical Research: Solid Earth,* **118(4)**. https://doi.org/10.1002/jgrb.50131

Silwal, V., & Tape, C. (2016). Seismic moment tensors and estimated uncertainties in southern Alaska. *Journal of Geophysical Research: Solid Earth,* **121(4)**. https://doi.org/10.1002/2015JB012588

Simmons, N. A., Myers, S. C., Morency, C., Chiang, A., & Knapp, D. R. (2021). SPiRaL: A multiresolution global tomography model of seismic wave speeds and radial anisotropy variations in the crust and mantle. *Geophysical Journal International, 227*(2). https://doi.org/10.1093/gji/ggab277

Snieder, R., & Wapenaar, K. (2010). Imaging with ambient noise. *Physics Today,* **63(9)**. https://doi.org/10.1063/1.3490500

Snoke, A. W., & Barnes, C. G. (2006). The development of tectonic concepts for the Klamath Mountains province, California and oregon. *Special Paper of the Geological Society of America,* **410**. https://doi.org/10.1130/2006.2410(01)

Stanciu, A. C. & Humphreys, G. Seismic architecture of the upper mantle underlying California and Nevada. *Journal of Geophysical Research: Solid Earth*, **126(12)**. https://doi.org/10.1029/2021JB021880

Stoddard, P. R. (1987). A kinematic model for the evolution of the Gorda Plate. *Journal of Geophysical Research: Solid Earth,* **92**. https://doi.org/10.1029/jb092ib11p11524

Strauss, J. A., & Allen, R. M. (2016). Benefits and costs of Earthquake Early Warning. *Seismological Research Letters, 87*(3). https://doi.org/10.1785/0220150149

Suess, M. P., & Shaw, J. H. (2003). P wave seismic velocity structure derived from sonic logs and industry reflection data in the Los Angeles basin, California. *Journal of Geophysical Research: Solid Earth,* **108**. https://doi.org/10.1029/2001jb001628

Tajima, T., Megngin, C., Derger, D., & Romanowicz, B. (2002). Feasibility of real-time broadband waveform inversion for simultaneous moment tensor and centroid location determination. *Bulletin of the Seismological Society of America*, **92(2)**, 739-750.

Tape, C., Liu, Q., Maggi, A., & Tromp, J. (2009). Adjoint tomography of the Southern California crust, *Science*, **325(5943)**, 988–992. https://doi.org/10.1126/science.1175298

Tape, C., Liu, Q., Maggi, A., & Tromp, J. (2010). Seismic tomography of the Southern California crust based on spectral-element and adjoint methods. *Geophysical Journal International, 180*(1). https://doi.org/10.1111/j.1365-246X.2009.04429.x

Tape, C., Liu, Q., & Tromp, J. (2007). Finite-frequency tomography using adjoint methods—Methodology and examples using membrane surface waves. *Geophysical Journal Internationial*, **168**, 1105-1129. https://doi.org/10.1111/j.1365-246X.2006.03191.x

Tarantola, A. (1984). Linearized inversion of seismic reflection data. *Geophysical Prospecting, 32*(6). https://doi.org/10.1111/j.1365-2478.1984.tb00751.x

Tarantola, A. (1987). Inverse problem theory: Methods for data fitting and model parameter estimation. *Inverse Problem Theory: Methods for Data Fitting and Model Parameter Estimation,* https://doi.org/10.1016/0031-9201(89)90124-6

Tarantola, A. (1988). Theoretical background for the inversion of seismic waveforms including elasticity and attenuation. *Pure and Applied Geophysics PAGEOPH, 128*(1-2). https://doi.org/10.1007/BF01772605

Thrastarson, S., van Herwaarden, D., & Fichtner, A. (2021). Inversionson: Fully Automated Seismic Waveform Inversions. *EarthArXiv.*

Thrastarson, S., van Herwaarden, D.-P., Krischer, L., and Fichtner, A. (2021). LASIF: Large-scale Seismic Inversion Framework, an updated version. *EarthArXiv*. https://doi.org/10.31223/X5NC84.

Thurber, C., Zhang, H., Brocher, T., & Langenheim, V. (2009). Regional three-dimensional seismic velocity model of the crust and uppermost mantle of northern California. *Journal of Geophysical Research: Solid Earth,* **114(1)**. https://doi.org/10.1029/2008JB005766

Tromp, J. (2020). Seismic wavefield imaging of earth's interior across scales. *Nature Reviews Earth and Environment*, **1**, 40-53. https://doi.org/10.1038/s43017-019-0003-8

Tromp, J., Tape, C., & Liu, Q. (2005). Seismic tomography, adjoint methods, time reversal, and banana-donut kernels. *Geophysical Journal International*, **160**, 195-216. https://doi.org/doi.org/10.1111/j.1365-246X.2004.02453.x

Tsai, Y-B., and Aki, K. (1969). Deterimination [sic] of focal depths of earthquakes in the mid-ocean ridges from amplitude spectra of surface waves.

Uieda, L., Tian, D., Leong, W. J., Schlitzer, W., Grund, M., Jones, M., Frölich, Y., Toney, L., Yao, J., Magen, Y., Tong, J.-H., Materna, K., Belem, A., Newton, T., Anant, A., Ziebarth, M., Quinn, J., & Wessel, P. (2023). PyGMT: a python interface for the Generic Mapping Tools (v0.9.0). Zenodo. https://doi.org/10.5281/zenodo.7772533

Uieda, L., & Wessel, P. (2019). PyGMT: Accessing the Generic Mapping Tools from Python. *AGU Fall Meeting 2019,* https://doi.org/10.6084/m9.figshare.11320280

Ulrich, I. E., Boehm, C., Zunino, A., & Fichtner, A. (2022). Analyzing resolution and model uncertainties for ultrasound computed tomography using Hessian information. *Proceeding of Medical Imaging 2022: Ultrasonic Imaging and Tomography*, **12038**, https://doi.org/10.1117/12.2608546

Vandecar, J. C., & Crosson, R. S. (1990). Determination of teleseismic relative phase arrival times using multi-channel cross-correlation and least squares. *Bulletin - Seismological Society of America, 80*(1). https://doi.org/10.1785/BSSA0800010150

Van Rossum, G., & Drake, F. L. (2009). *Python 3 Reference Manual*. Scotts Valley, CA: CreateSpace.

Verdonck, D. & Zandt, G. (1994). Three-dimensional crustal structure of the Mendocino Triple Junction region from local earthquake travel times. *Journal of Geophysical Research: Solid Earth*, **99(B12)**, 23843-23858. https://doi.org/10.1029/94JB01238

Virieux, J., & Operto, S. (2009). An overview of full-waveform inversion in exploration geophysics. *Geophysics, 74*(6). https://doi.org/10.1190/1.3238367

Wang, D., Wu, S., Li, T., Tong, P., & Gao, Y. (2022). Elongated magma plumbing system beneath the Coso Volcanic Field, California, constrained by seismic reflection tomography. *Journal of Geophysical Research: Solid Earth*, 127, e2021JB023582. https://doi.org/doi.org/10.1029/2021JB023582

Wang, K., Yang, Y., Jiang, C., Wang, Y., Tong, P., Liu, T., & Liu, Q. (2021). Adjoint Tomography of Ambient Noise Data and Teleseismic P Waves: Methodology and Applications to Central California. *Journal of Geophysical Research: Solid Earth,* **126(6)**. https://doi.org/10.1029/2021JB021648

Wang, Z., Bovik, A. C., Sheikh, H. R., & Simoncelli, E. P. (2004). Image quality assessment: From error visibility to structural similarity. *IEEE Transactions on Image Processing, 13*(4). https://doi.org/10.1109/TIP.2003.819861

Wehner, D., Blom, N., Rawlinson, N., Daryono, Böhm, C., Miller, M. S., Supendi, P., & Widiyantoro, S. (2022). SASSY21: A 3-D seismic structural model of the lithosphere and underlying mantle beneath Southeast Asia from multi-scale adjoint waveform tomography. *Journal of Geophysical Research: Solid Earth, 127*(3). https://doi.org/10.1029/2021JB022930

Wehner, D., Rawlinson, N., Greenfield, T., Daryono, Miller, M. S., Supendi, P., ChuanChuan, L., & Widiyantoro, S. (2022). SASSIER22: Full-Waveform Tomography of the Eastern Indonesian Region That Includes Topography, Bathymetry, and the Fluid Ocean. *Geochemistry, Geophysics, Geosystems,* **23(11)**. https://doi.org/10.1029/2022GC010563

Wentworth, C. M., Fisher, G. R., Levine, P., & Jachens, R. C. (1995). *The surface of crystalline basement, Great Valley and Sierra Nevada, California: A digital map database* (v.1.1.0). Reston, VA. https://doi.org/10.3133/ofr9596.

Wessel, P., Luis, J. F., Uieda, L., Scharroo, R., Wobbe, F., Smith, W. H. F., & Tian, D. (2019). The Generic Mapping Tools version 6. *Geochemistry, Geophysics, Geosystems, 20*(11). https://doi.org/10.1029/2019GC008515

Wilson, D. S. (1989). Deformation of the so-called Gorda plate. *Journal of Geophysical Research,* **94**. https://doi.org/10.1029/JB094iB03p03065

Wright, H. M., Vazquez, J. A., Champion, D. E., Calvert, A. T., Mangan, M. T., Stelten, M. E., Cooper, K. M., Herzig, C., & Schriener Jr., A. (2015). Episodic Holocene eruption of the Salton Buttes rhyolites, California, from paleomagnetic, U-Th, and Ar/Ar dating. *Geochemistry, Geophysics, Geosystems,* **16(4)**, 1198-1210. https://doi.org/10.1002/2015GC005714

Xiong, N., Qiu, H., & Niu, F. (2021). Data-driven velocity model evaluation using k-means clustering.Geophysical Research Letters, **48(23)**. https://doi.org/10.1029/2019JB018423.

Zandt, G., Gilbert, H., Owens, T. J., Ducea, M., Saleeby, J., & Jones, C. H. (2004). *Active foundering of a continental arc root beneath the southern Sierra Nevada in California,* https://10.1038/nature02847

Zandt, G. & Humphreys, E. (2008). Toroidal mantle flow through the western U.S. slab window. *Geology*, **36(4)**, 295-298. https://doi.org/10.1130/G24611A.1

Zhou, T., Xi, Z., Chen, M., & Li, J. (2022). Assessment of seismic tomographic models of the contiguous United States using intermediate-period 3-D wavefield simulation. *Geophysical Journal International, 228*(2). https://doi.org/10.1093/gji/ggab406

Zhu, H., Li, S., Fomel, S., Stadler, G., & Ghattas, O. (2016). A Bayesian approach to estimate uncertainty for full-waveform inversion using a priori information from depth migration. *Geophysics*, **81(5)**, R307-R323. https://doi.org/10.1190/geo2015-0641.1

Zucca, J. J., Hutchings, L. J., & Kasameyer, P. W. (1994). Seismic velocity and attenuation structure of the Geysers Geothermal Field, California. *Geothermics, 23*(2). https://doi.org/10.1016/0375-6505(94)90033-7

Appendix A. Supplemental information for "Comparing adjoint waveform tomography models of California using different starting models"

Information on the events used in both the inversion and validation datasets, including a Jupyter Notebook for downloading the relevant data, can be found on Zenodo (Doody, 2023b).

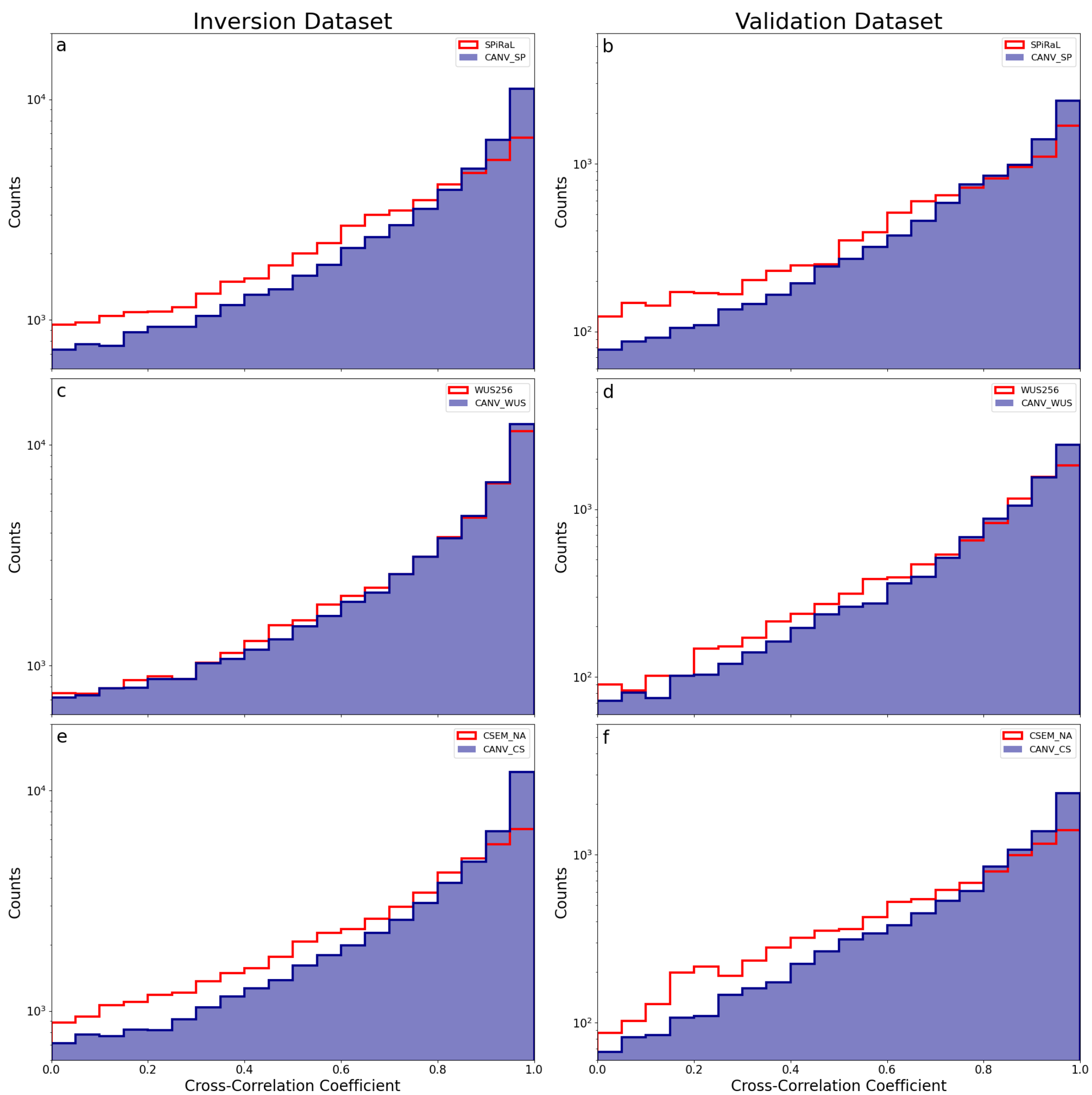

Figure A.1. Stacked comparison of envelope cross-correlation values for the starting models (red histograms) and the final models (blue histograms), respectively. Panels a, c, and f show values for the inversion dataset, while panels b, d, and f show values for the validation dataset. Cross-correlation values are binned in 0.05 intervals.

Table A.1. List of seismic networks from the Federation of Digital Seismic Networks who provided data used in this study. Digital object identifiers (DOIs) are listed if available.

Network Code	Network Name	DOI (if available)
2D	Albacore Array	N/A
4E	MARS/Testing of cabled broadband OBS using MARS test facility	https://doi.org/10.7914/SN/4E_2010
5A	Basin & Range, Pleasant Valley Faulting, Crustal-Scale Geometry of Active Continental Normal Faults.	https://doi.org/10.7914/SN/5A_2010
7D	Cascadia Initiative Community Experiment - OBS Component	https://doi.org/10.7914/SN/7D_2011
8E	Mammoth Mountain Broadband Experiment	
AZ	ANZA Regional Network	https://doi.org/10.7914/SN/AZ
BC	Red Sísmica del Noroeste de México	https://doi.org/10.7914/SN/BC
BK	Berkeley Digital Seismograph Network	https://doi.org/10.7932/BDSN
CC	Cascade Chain Volcano Monitoring	https://doi.org/10.7914/SN/CC
CI	Southern California Seismic Network	https://doi.org/10.7914/SN/CI
G	GEOSCOPE - French Global Network of Seismological Broadband Stations	https://doi.org/10.18715/GEOSCOPE.G
GM	U.S. Geological Survey Networks	https://doi.org/10.7914/SN/GM
GS	U.S. Geological Survey Networks	https://doi.org/10.7914/SN/GS
IM	International Miscellaneous Stations (IMS)	N/A
LB	Leo Brady Network	N/A
NC	USGS Northern California Network	https://doi.org/10.7914/SN/NC
NN	Nevada Seismic Network	https://doi.org/10.7914/SN/NN
NP	United States National Strong-Motion Network	https://doi.org/10.7914/SN/NP
NR	Network of Autonomously Recording Seismographs (NARS)	https://doi.org/10.7914/SN/NR
PB	Plate Boundary Observatory Borehole Seismic Network (PBO)	N/A
PG	Central Coast Seismic Network (PG&E)	N/A
PY	Piñon Flats Observatory Array	https://doi.org/10.7914/SN/PY
RE	US Bureau of Reclamation Seismic Networks	N/A
SB	UC Santa Barbara Engineering Seismology Network	https://doi.org/10.7914/SN/SB
SF	San Andreas Fault Observatory at Depth (SAFOD)	N/A
SN	Southern Great Basin Network	https://doi.org/10.7914/SN/SN
TA	USArray Transportable Array	https://doi.org/10.7914/SN/TA
TO	Tectonic Observatory	N/A
UO	Pacific Northwest Seismic Network - University of Oregon	https://doi.org/10.7914/SN/UO
US	United States National Seismic Network	https://doi.org/10.7914/SN/UU
UW	Pacific Northwest Seismic Network - University of Washington	https://doi.org/10.7914/SN/UW
XC	Collaborative Research: Understanding the causes of continental intraplate tectonomagmatism: A case study in the Pacific Northwest (HLP)	https://doi.org/10.7914/SN/XC_2006
XE	Sierra Nevada EarthScope Project (SNEP)	https://doi.org/10.7914/SN/XE_2005
XJ	Wells, Nevada Aftershock Recording	https://doi.org/10.7914/SN/XJ_2008
XN	Parkfield Passive Seismic Array	https://doi.org/10.7914/SN/XN_2000
XQ	Oregon Array for Teleseismic Study (OATS) Seismic and Geodetic Investigations of Mendocino Triple Junction Dynamics (FAME)	N/A https://doi.org/10.7914/SN/XQ_2007
Y3	Wells, Nevada Aftershock Recording (RAMP NV)	https://doi.org/10.7914/SN/Y3_2008

YB	Deep Fault Structure Beneath the Mojave from a High Density, Passive Seismic Profile	https://doi.org/10.7914/SN/YB_2018
YG	South Bay Seismic Array Seismic Imaging of New Transitional Crust in the Salton Trough Oblique Rift	N/A https://doi.org/10.7914/SN/YG_2011
YH	Seismic tomography and location calibration around the SAFOD site (PASO-TRES)	https://doi.org/10.7914/SN/YH_2004
YN	San Jacinto Fault Zone Experiment	https://doi.org/10.7914/SN/YN_2010
YS	Observational Constraints on Persistent Water Level Changes Generated by Seismic Waves (Grants Pass Well)	https://doi.org/10.7914/SN/YS_2001
YU	Northern California Delta (Delta)	https://doi.org/10.7914/SN/YU_2006
YW	Resolving structural control of episodic tremor and slip along the length of Cascadia (FACES)	https://doi.org/10.7914/SN/YW_2007
YX	Flexarrray 3D Passive Seismic Imaging of Core-Complex Extension in the Ruby Range Nevada	https://doi.org/10.7914/SN/YX_2010
Z5	Seismicity, Structure and Dynamics of the Gorda Deformation Zone (Gorda)	https://doi.org/10.7914/SN/Z5_2013
ZY	Portable Southern California Seismic Networks (Caltech)	N/A

Appendix B. Supplemental information for “Moment tensor catalogue of California and Nevada using 3D Green’s functions”

Table B.1. Event information and catalogue values for the moment tensors inverted in Chapter 2. EVID denotes the event ID used by Salvus to call events. Origin times and lat/lon coordinates for each event are listed in Columns 2-4. Columns with the prefix “G_” denote values for the GCMT. “M_” denotes MTTime solutions, and “U_” denotes ANSS solutions. Columns with the suffix “Mag” show magnitude values for the different catalogues, “Dep” shows depth, “DC” shows double couple percentage, and ‘VR’ shows variance reduction.

EVID	Origin_Time	Lat	Lon	G_Mag	G_Dep	G_DC	G_VR	M_Mag	M_Dep	M_DC	M_VR	U_Mag	U_Dep
18685	12-08-2001T23:36:16	32.18	-114.99	5.74	15	46	62.6	5.75	5	84	79.33	5.7	6.981
18896	02-22-2002T19:32:47	32.51	-115.39	5.47	15	89	60.51	5.47	15	90	74.16	5.7	7.007
21173	03-17-2004T23:53:13	36.03	-121.35	4.72	12	28	-82.94	4.82	3	68	63.59	4.51	4.271
21540	06-15-2004T22:28:52	32.45	-117.92	5.04	12	96	71.57	5.11	13	62	78.79	4.98	9.824
21904	09-18-2004T23:02:20	38.02	-118.69	5.39	12	90	76.94	5.37	3	94	89.46	5.4	3.355
21905	09-18-2004T23:43:44	38.02	-118.7	5.37	12	70	70.91	5.32	2	98	84.4	5.35	0.431
21946	09-28-2004T17:15:31	35.92	-120.54	5.97	12	82	79.65	5.92	8	98	86.46	5.97	8.136
21952	09-29-2004T17:10:08	36	-120.54	5.07	12	87	76.53	5.21	22	70	82.39	5	10.772
21954	09-29-2004T22:54:56	35.41	-118.73	5.02	12	77	72.47	5	11	98	83.6	5.03	2.788
21957	09-30-2004T18:54:32	36.02	-120.57	4.94	12	95	61.93	4.85	9	100	78.98	4.88	9.889
23091	03-18-2005T07:24:02	40.4	-124.86	4.88	21.6	98	69.51	4.86	23	95	77.49	4.85	17.08
23311	04-16-2005T19:18:22	35.03	-119.18	5.14	12	93	-1328.99	4.58	9	91	18.92	4.59	9.288
23577	06-12-2005T15:41:50	33.63	-116.59	5.21	14	97	74.97	5.2	9	61	86.85	5.2	13.051
23597	06-16-2005T20:53:29	34.09	-116.99	4.87	12	41	62.82	4.87	11	100	74.86	4.88	10.558
23978	08-31-2005T22:50:22	32.92	-115.65	4.81	12	14	-5.69	4.69	12	94	57.93	4.5	2
23984	09-02-2005T01:27:23	33.23	-115.52	5.15	12	98	61.66	5.14	4	90	83.24	4.5	4.977
25265	05-12-2006T10:37:32	38.8	-122.85	4.81	13.6	21	20.91	4.71	4	57	76.67	4.71	3.618
25320	05-24-2006T04:20:30	32.43	-115.28	5.29	12	93	41.92	5.51	3	78	84.03	5.37	6.006
26804	02-26-2007T12:20:00	40.63	-124.9	5.42	15.9	85	77.63	5.49	17	67	79.51	5.4	-0.533

EVID	Origin_Time	Lat	Lon	G_Mag	G_Dep	G_DC	G_VR	M_Mag	M_Dep	M_DC	M_VR	U_Mag	U_Dep
27415	06-25-2007T02:32:28	41.08	-124.87	5.04	22.5	65	71.05	4.98	15	85	82.46	5	2.563
28088	10-31-2007T03:04:59	37.37	-121.78	5.56	13.9	93	85.63	5.53	9	93	87	5.45	9.741
28468	01-19-2008T23:13:10	40.24	-122.69	4.94	20.5	38	-356.44	4.78	9	86	77.05	4.7	2.049
28561	02-09-2008T07:12:09	32.56	-115.37	5.14	12	34	29.34	5.21	11	99	77.14	5.1	6.001
28572	02-11-2008T18:29:35	32.46	-115.28	5.14	12	63	66.5	5.07	14	96	79.94	5.1	6.001
28576	02-12-2008T04:32:41	32.48	-115.34	5.02	12.4	43	47.78	5	18	99	79.47	4.97	6.018
28611	02-19-2008T22:41:30	32.41	-115.37	5.1	12	52	34.04	5.01	11	54	75.88	5.01	6.006
28613	02-20-2008T01:28:56	32.45	-115.33	4.84	16.6	82	-19.84	4.84	2	71	87.15	4.83	6.001
28621	2-21-2008T14:16:10	41.16	-114.85	6.02	13.5	84	43.04	5.98	9	97	83.46	5.9	7.9
28627	02-22-2008T19:31:20	32.45	-115.24	4.9	12.1	46	56.75	4.91	4	84	83.72	4.78	6.001
28956	04-26-2008T06:40:14	39.56	-119.91	5.01	15.1	69	69.3	4.91	2	100	89.17	5.1	2.8
28984	4-30-2008T03:03:08	40.83	-123.62	5.36	28	91	49.59	5.33	30	81	84.75	5.4	27.755
29436	07-29-2008T18:42:19	33.93	-117.84	5.46	20	91	77.33	5.43	13	96	85.9	5.44	15.503
29891	10-26-2008T09:27:24	40.29	-124.63	5.05	22.4	68	70.48	4.89	9	99	82.18	4.9	20.827
30078	12-06-2008T04:18:45	34.83	-116.39	5.13	12	84	79.05	5.11	2	86	88.84	5.06	6.37
30621	03-24-2009T11:55:46	33.31	-115.66	4.96	12	29	-3.46	4.78	2	92	79.86	4.77	6.003
31284	08-07-2009T10:49:39	40.34	-124.57	4.99	18.5	69	49.98	4.88	16	73	81.65	4.92	16.257
31473	09-19-2009T22:55:21	32.37	-115.31	5.17	12	76	69.15	5.17	18	87	80.28	5.08	9.987
31517	10-01-2009T10:01:28	36.37	-117.83	5.14	14.8	82	71.7	5.09	3	80	89.23	5	3.985

EVID	Origin_Time	Lat	Lon	G_Mag	G_Dep	G_DC	G_VR	M_Mag	M_Dep	M_DC	M_VR	U_Mag	U_Dep
31542	10-03-2009T01:09:23	36.41	-117.82	4.87	20.7	52	-5.97	4.71	7	97	57.72	4.74	0.7
31543	10-03-2009T01:16:06	36.39	-117.78	5.22	17.9	77	66.71	5.12	9	98	81.84	5.19	-1.77
32014	12-30-2009T18:49:01	32.46	-115.17	5.87	14.7	80	41.72	5.88	15	90	71.24	5.8	5.971
32540	04-05-2010T11:14:18	32.76	-115.79	5.11	20.9	80	36.87	5.01	19	80	74.26	4.93	13.653
32542	04-05-2010T13:33:11	32.81	-115.68	4.98	20.3	58	-11.87	4.84	14	72	71.92	4.73	0.002
32546	04-06-2010T08:12:27	31.98	-114.93	4.86	15.1	81	66.6	4.86	6	95	81.48	4.67	9.961
32552	04-08-2010T16:44:29	32.25	-115.26	5.37	12	81	55.35	5.38	18	98	76.65	5.29	9.985
32590	04-15-2010T10:20:48	32.04	-115.08	4.85	12	74	60.97	4.81	17	100	74.21	4.73	16.603
32697	05-08-2010T18:33:11	32.6	-115.76	4.97	19	71	57.88	4.84	12	96	76.52	4.8	5.955
32698	05-08-2010T18:46:28	32.59	-115.81	4.86	15	93	57	4.77	13	99	75.35	4.69	2.383
32749	05-22-2010T17:31:00	32.58	-115.83	5.06	19	60	50.39	5.01	23	60	83.29	4.9	8.073
32848	06-15-2010T04:27:01	32.66	-115.98	5.8	13.4	54	76.95	5.82	17	73	87.45	5.71	8.756
32949	07-07-2010T23:53:37	33.41	-116.51	5.54	24.1	72	74.6	5.43	12	92	83.95	5.42	12.318
33278	09-14-2010T10:52:21	32.14	-115.2	5.01	14.7	38	18.79	4.87	12	100	74.59	4.96	9.939
33302	09-20-2010T00:30:06	32.11	-115.11	4.86	14.9	73	56.81	4.8	17	92	74.9	4.75	9.939
33718	12-11-2010T12:52:30	32.31	-115.22	4.83	15.3	40	57.83	4.78	13	75	85.09	4.71	13.005
34139	02-18-2011T17:47:38	32.08	-115.06	5.15	12	84	78.17	5.16	17	94	81.16	5.1	14.9
34637	04-17-2011T00:45:40	38.47	-118.71	4.8	12.9	55	-26.76	4.72	14	71	67.37	4.6	5.1
35435	08-27-2011T07:18:24	36.51	-121.21	4.82	19	89	76.2	4.8	19	91	84.87	4.64	7.5

EVID	Origin_Time	Lat	Lon	G_Mag	G_Dep	G_DC	G_VR	M_Mag	M_Dep	M_DC	M_VR	U_Mag	U_Dep
35760	10-27-2011T06:37:13	39.65	-120.32	4.9	32.7	76	65.75	4.69	10	91	86.36	4.73	11.974
36381	02-13-2012T21:07:06	41.16	-123.79	5.62	29.3	90	68.26	5.59	28	89	83.52	5.6	27.358
37219	07-01-2012T03:25:21	32.23	-115.37	4.82	18.4	83	39.34	4.73	20	91	79.59	4.6	2.8
37221	07-01-2012T06:36:07	32.18	-115.24	4.84	12	57	7.77	4.71	19	93	82.84	4.7	9.6
37550	08-26-2012T19:31:25	32.92	-115.59	5.39	12	39	64.49	5.37	13	96	72.55	5.3	8.3
37551	08-26-2012T20:58:01	32.95	-115.56	5.49	12	63	63.69	5.49	12	94	67.53	5.4	8.3
37905	10-21-2012T06:55:13	36.27	-120.89	5.38	12	75	50.85	5.28	7	99	76.67	5.29	8.619
38697	02-13-2013T00:10:20	38.06	-118.04	5.26	16.2	93	48.64	5.14	9	100	73.34	4.94	8.635
39280	5-24-2013T03:47:12	40.23	-121.05	5.72	20	70	61.68	5.67	7	92	85.38	5.69	7.968
39304	5-29-2013T14:38:07	34.45	-120.06	4.94	17	99	-80.31	4.82	14	98	85.92	4.8	7.12
40041	10-11-2013T23:05:59	40.83	-124.91	5.2	21.7	56	-5.78	5.01	20	87	83.7	4.9	8.6
40582	01-12-2014T20:24:48	38.68	-122.98	4.8	22.8	41	-13.92	4.67	10	61	75.68	4.53	1.9
41040	03-29-2014T04:09:47	34.05	-117.89	5.13	12	39	75.48	5.14	13	99	79.77	5.1	5.09
42031	08-24-2014T10:20:49	38.31	-122.38	6.07	12	94	72.56	6.07	14	99	76.73	6.02	11.12
42551	11-05-2014T07:23:09	41.95	-119.65	4.71	16.7	89	-96.01	4.59	5	100	78.62	4.6	0.1
42618	11-13-2014T06:36:11	41.91	-119.56	4.72	18.5	83	-146.63	4.56	8	90	79.87	4.6	0
43123	01-22-2015T09:09:21	41.85	-119.58	4.84	19.3	92	-106.43	4.7	8	77	79.84	4.5	11.7
43162	01-28-2015T21:09:01	40.31	-124.31	5.76	30	97	64.44	5.76	35	93	83.58	5.72	16.881
43235	2-9-2015T01:45:06	31.62	-115.66	5.02	22.6	66	74.44	4.91	14	98	85.79	4.89	12.503

EVID	Origin_Time	Lat	Lon	G_Mag	G_Dep	G_DC	G_VR	M_Mag	M_Dep	M_DC	M_VR	U_Mag	U_Dep
43266	02-14-2015T02:29:00	37.15	-117.33	4.93	19.5	79	-464.02	4.77	8	99	79.95	4.8	17
43838	05-22-2015T18:47:45	37.36	-114.65	4.97	18.4	55	48.59	4.83	9	97	82.91	5.3	4
44518	09-14-2015T13:55:54	41.9	-119.5	4.89	21.8	53	-60.54	4.75	6	90	76.21	4.7	9.7
45403	02-16-2016T23:04:30	37.23	-118.5	4.91	28.9	85	28.29	4.75	14	98	79.58	4.77	15.06
45449	02-24-2016T00:02:27	35.55	-119.45	4.95	27.1	91	86.34	4.97	27	85	87.27	4.87	22.14
46078	06-10-2016T08:04:41	33.51	-116.48	5.27	24.7	89	65.65	5.17	11	95	83.56	5.19	12.31
46342	07-21-2016T23:09:07	40.66	-123.94	4.88	29.6	62	55.74	4.8	30	71	80.4	4.81	26.24
46441	08-10-2016T02:57:20	39.38	-122.82	5.08	17.8	94	71.45	4.99	15	95	82.61	5.09	14.45
47264	12-14-2016T16:41:10	38.82	-122.86	5.14	12	60	53.64	5.09	15	98	83.56	5.01	1.48
47370	12-28-2016T08:18:06	38.4	-118.87	5.69	20.9	50	69.15	5.64	12	100	78.35	5.6	11.3
47371	12-28-2016T08:22:15	38.41	-118.93	5.57	23.9	23	72.68	5.52	13	89	90.55	5.6	12.2
47372	12-28-2016T09:13:52	38.4	-118.91	5.72	26.2	70	75.19	5.59	11	97	82.31	5.5	8.8
49208	11-13-2017T19:31:32	36.67	-121.31	4.69	14.6	96	74.72	4.68	15	85	83.45	4.58	6.31
50040	03-22-2018T16:24:49	40.66	-124.47	4.82	26	83	-13.59	4.65	24	99	73.05	4.4	24.5
50142	04-05-2018T19:29:20	33.9	-119.72	5.36	12	95	82.97	5.35	10	100	85.78	5.3	9.8
51725	11-19-2018T20:18:45	32.21	-115.22	4.88	13.4	67	51.79	4.86	12	100	82.44	4.8	10.9
53184	6-23-2019T03:53:06	40.25	-124.29	5.65	15.1	81	38.49	5.5	9	98	82.79	5.58	9.44
53253	07-04-2019T17:33:58	35.69	-117.54	6.45	12.7	84	64.13	6.41	16	91	79.77	6.4	10.5
53257	07-05-2019T11:07:57	35.78	-117.57	5.43	15.6	99	74.49	5.36	13	100	85.73	5.37	6.95

EVID	Origin_Time	Lat	Lon	G_Mag	G_Dep	G_DC	G_VR	M_Mag	M_Dep	M_DC	M_VR	U_Mag	U_Dep
53267	07-06-2019T09:28:32	35.95	-117.65	5.01	12	88	10.31	4.86	8	99	71.7	4.89	3.95
53324	07-12-2019T13:11:41	35.65	-117.58	4.92	14.9	76	76.67	4.86	10	95	86.55	4.9	9.48
53564	08-22-2019T20:49:54	35.95	-117.64	5.06	12.6	85	54.58	4.96	12	88	81.94	4.89	4.93
53884	10-15-2019T05:33:47	37.98	-122.06	4.64	12	82	25.94	4.52	12	93	71.84	4.5	14
53889	10-15-2019T19:42:32	36.65	-121.33	4.85	12	77	47.76	4.82	15	75	76.29	4.71	10.1
54854	03-07-2020T03:52:08	31.79	-114.58	5.6	14.2	83	84.31	5.62	14	96	87.47	5.5	10
54924	03-18-2020T22:08:23	40.4	-124.47	5.3	34.1	80	66.72	5.29	37	81	78.84	5.2	28.6
54949	03-22-2020T16:27:41	40.39	-124.85	4.89	21.6	90	63.96	4.79	12	98	74.24	4.78	12.4
55032	04-04-2020T01:53:24	33.57	-116.42	5.02	24.8	65	-29.52	4.9	22	99	70.79	4.87	10.45
55072	4-11-2020T14:36:42	38.07	-118.67	5.26	14.6	77	54.43	5.18	10	86	76.7	5.24	8.45
55074	4-11-2020T16:22:55	38.11	-118.7	4.67	14.6	74	11.84	4.56	8	63	68.47	4.57	8.94
55278	05-16-2020T11:50:57	38.24	-117.67	4.71	20.5	100	-42.55	4.6	11	95	79.58	4.6	16.8
55308	05-20-2020T12:36:58	38.24	-117.72	4.91	15.5	83	75.5	4.86	14	97	83.63	5	11.7
55319	5-22-2020T00:22:05	38.23	-117.77	4.79	12	86	76.24	4.73	8	91	87.11	5.1	7.2
55413	06-04-2020T01:32:15	35.6	-117.43	5.57	15	82	80.1	5.51	8	98	88	5.51	8.44
55438	06-08-2020T03:24:10	38.26	-117.75	4.87	12	78	64.05	4.81	11	95	79.12	4.8	5.2
55558	06-24-2020T17:40:54	36.46	-117.94	5.84	17.6	65	74.29	5.8	8	93	86.01	5.8	4.7
55962	08-19-2020T17:32:14	36.45	-117.48	4.83	12	86	80.18	4.78	8	100	85.54	4.72	-0.57
56257	10-01-2020T00:31:29	33.04	-115.6	5.01	12	66	64.61	4.97	10	96	79.08	4.93	14.19

Appendix C. Supplemental information for "CANVAS: An adjoint waveform tomography model of California and Nevada"

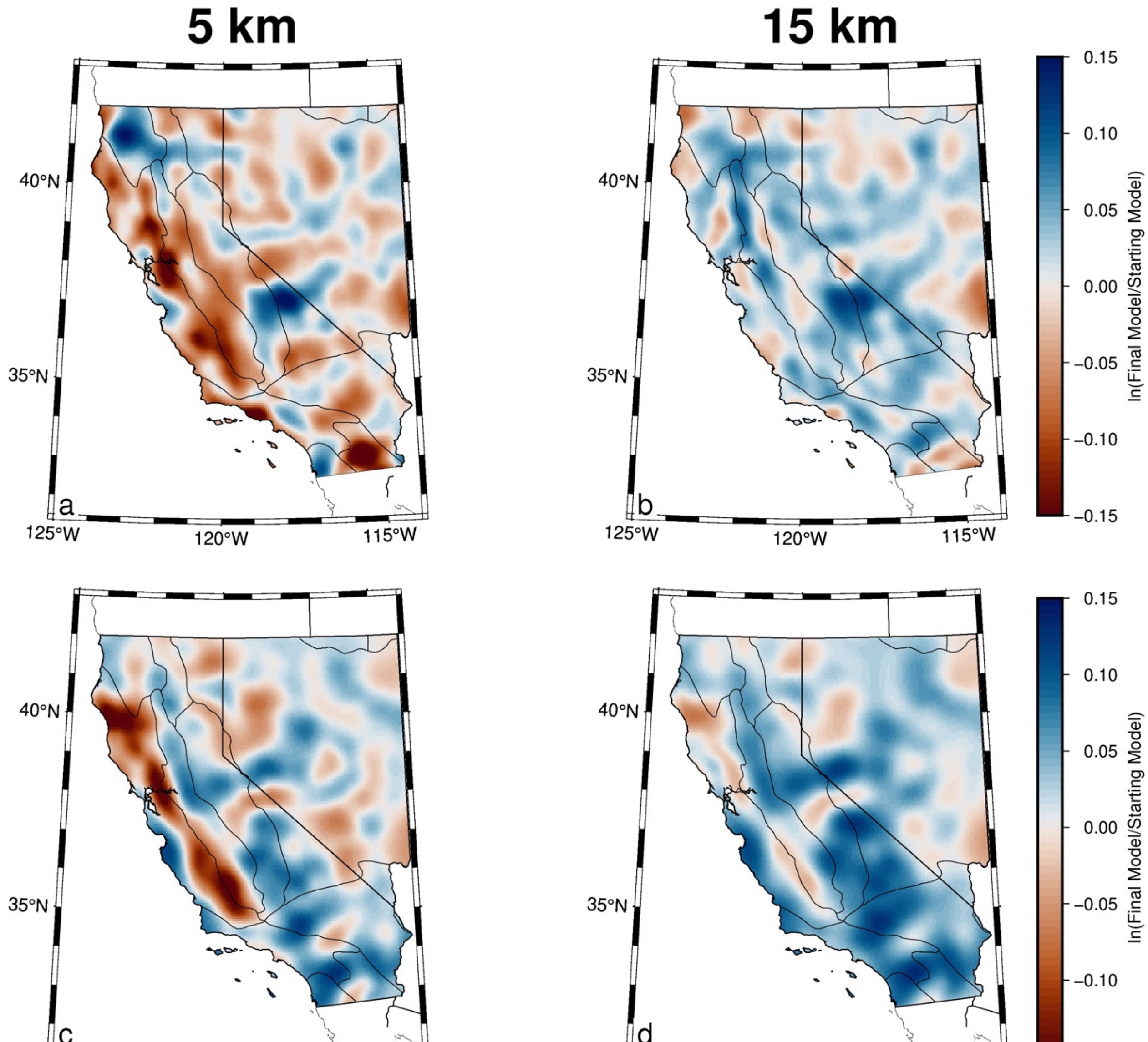

Figure C.1. *Natural log of the ratio between WUS256 and CANVAS, for Vs (a-b) and Vp(c-d) at 5km (a,c) and 15km (b,d). The values of the ratio correspond to the amplitude of changes (e.g. a value of -0.15 means that the velocity has decrease by 15% compared to WUS256). Red regions show areas where CANVAS has lower absolute velocities than WUS256; blue regions show areas where CANVAS has faster absolute velocities than WUS256.*